UNIVERSITY OF CALIFORNIA, SAN DIEGO

Inhomogeneous Phase Transition of Vanadium Oxide on Mesoscopic Scale

A dissertation submitted in partial satisfaction of the requirements for the degree

Doctor of Philosophy

in

Materials Science and Engineering

by

Siming Wang

Committee in charge:

Professor Ivan K. Schuller, Chair
Professor Daniel P. Arovas
Professor Yeshaiahu Fainman
Professor Shayan Mookherjea
Professor Oleg G. Shpyrko

2014

The Dissertation of Siming Wang is approved, and it is acceptable in quality and form for publication on microfilm and electronically:

Chair

University of California, San Diego

2014

Dedication

Dedicated to my parents

Table of Contents

Chapter II

Chapter III

Chapter IV

List of Figures

List of Tables

Acknowledgements

The completion of this dissertation would not be possible without the support from my colleagues, collaborators, families and friends in the past 6 years.

First of all, I thank my advisor Prof. Ivan K. Schuller. It is always my honor to be a member in the Schuller's lab. In the past 5 years, Prof. Schuller has taught me not only the scientific knowledge, but also the serious attitude in work. Besides the research skills, I have also developed presentation, communication, and multitasking skills. One most important thing that I learned from Prof. Schuller is his vision. He is always able to spot the fundamental problems in the current research topics and design simple, direct, quantitative experiments to address them. This skill is crucial in many professions beyond scientific research. Prof. Schuller is also very supportive when every member of the lab is moving forward to the next step of his/her career. He always does his best to help the young physicists to plan for their future. It is certainly a great experience to work with him and learn all the important things that he emphasizes everyday.

I thank Prof. Amos Sharoni and Dr. Juan Gabriel Ramirez who taught me the basic knowledge and skill in magnetron sputtering. I inherited the project to study the phase transitions of vanadium oxides initiated by them. Without their preliminary research and experiences, it would be much more difficult for me to start my graduate research. I worked with Dr. Ramirez for three years and we collaborated on a broad range of topics including phase transitions, magnetism, spintronics, spectroscopy, and numerical simulations. We had discussions on a daily basis which always inspired me in my research. Dr. Ramirez also gave a lot of helpful comments on this dissertation.

I thank Prof. Jose de la Venta and Dr. Thomas Saerbeck who gave me the knowledge in magnetism. I worked with Prof. de la Venta for nearly 4 years. We developed the procedure for vanadium oxide thin film deposition together. We collaborated to study the exchange bias and the magnetostrictive effect in magnetic materials. Dr. Saerbeck taught me a fundamental skill in physics, X-ray diffraction. He also gave a lot of helpful comments on this dissertation. I always respect his serious attitude in work.

I thank Dr. Alexandre Zimmers and his colleagues at CNRS in France. I collaborated with Dr. Zimmers and learned how to use fluorescent spectra to probe the surface temperature of materials. I thank Dr. Stefan Guenon and his colleagues at University of Tubingen in Germany. I collaborated with Dr. Guenon to study local heating at cryogenic temperatures and develop nanofabrication techniques. He also gave a lot of helpful comments on this dissertation. I truly respect his hard working attitude.

I thank Prof. Oleg G. Shpyrko, Sebastian H. Dietze and their colleagues at UCSD. I collaborated with them to perform synchrotron experiments on vanadium oxides. I thank Prof. Dimitri N. Basov, Alexander Mcleod and their colleagues at UCSD. I collaborated with them to study the scanning near-field spectroscopy of vanadium oxides. I thank Prof. Richard D. Averitt, Dr. Mengkun Liu, Elsa Abreu and their colleagues at Boston University. I collaborated with them to study the ultrafast spectroscopy of vanadium oxides.

I thank Dr. Kevin G. West for helping me develop the thin film growth and nanofabrication procedure. I thank Dr. Yaniv Rosen for his training on nanofabrication techniques and lab safety. Dr. West and Dr. Rosen both gave me a lot of supports and encouragements when I had a difficult time in my work.

I thank Ilya Valmianski and Jamie Wampler for their helpful comments on this thesis. I thank all my colleagues and collaborators, Corneliu Colesniuc, Mikhail Erekhinsky, Ali Basaran, Carlos Monton, Juan Pereiro Viterbo, Christian Urban, Shimshon Barad, Xavier Batlle, Miguel A. Garcia, Rafael Morales, Samuel Hevia, Mahmut Sami Kavrik, Javier Villegas, Michael Fitzsimons, Axel Hoffmann, Wei Zhang, David Hsieh, Hao Chu. I had a lot of discussions with them, which inspires me in my research. I thank the support from Robin K. Knox, Amie Diza, Charlotte Lauve, and other staff members from the physics department and the materials science and engineering program. I could not receive my PhD without their supports.

Last but not least, I thank my parents for their love and support in the past 6 years. Whenever there is a difficult time, they are always ready to back me up. I could not have been where I am today without them. I thank my host family Sulfren and Chris Deng, and many other friends in San Diego. It was a great experience to meet all of you.

Chapter III in part is currently being prepared for submission for publication of the material. Co-authors include J. G. Ramirez, and I. K. Schuller. The dissertation author was the primary investigator and author of this material.

Chapter IV, in part (section IV.2), has been previously published in: A. Zimmers, L. Aigouy, M. Mortier, A. Sharoni, S. Wang, K. G. West, J. G. Ramirez, and I. K. Schuller, "Role of Thermal Heating on the Voltage Induced Insulator-Metal Transition in VO_2", Phys. Rev. Lett. **110**, 056601 (2013). The dissertation author was a co-author of this paper. Chapter IV, in part (section IV.3), has been previously published in: S. Guenon, S. Scharinger, S. Wang, J. G. Ramirez, D. Koelle, R. Kleiner, and I. K. Schuller, "Electrical

breakdown in a V_2O_3 device at the insulator-to-metal transition", Europhys. Lett. **101**, 57003 (2013). The dissertation author was a co-auther of this paper. Chapter IV, in part (section IV.3), has been previously published in: S. Guenon, S. Scharinger, S. Wang, J. G. Ramirez, D. Koelle, R. Kleiner, and I. K. Schuller, "Electrical Breakdown in a V_2O_3 device at the Insulator to Metal Transition", arXiv:1210.6648 (2012). The dissertation author was a co-auther of this paper.

Chapter V, in part (section V.2), has been previously published in: J. de la Venta, S. Wang, J. G. Ramirez, and I. K. Schuller, "Control of magnetism across metal to insulator transitions", Appl. Phys. Lett. **102**, 122404 (2013). The dissertation author was a co-author of this paper. Chapter V, in part (section V.3), has been previously published in: J. de la Venta, S. Wang, T. Saerbeck, J. G. Ramirez, I. Valmianski, and I. K. Schuller, "Coercivity enhancement in V_2O_3/Ni bilayers driven by nanoscale phase coexistence", Appl. Phys. Lett. **104**, 062410 (2014). The dissertation author was a co-author of this paper. Chapter V, in part (section V.2 and V.3), has been previously published in: T. Saerbeck, J. de la Venta, S. Wang, J. G. Ramirez, M. Erekhinsky, I. Valmianski, and I. K. Schuller, "Coupling of magnetism and structural phase transitions by interfacial strain", J. Mater. Rev.. The dissertation author was a co-author of this paper.

The magnetism aspects of the work in this dissertation were supported by U.S. Department of Energy, under Grant No. DE FG03-87ER-45332, and the oxide related science by the AFOSR Grant No. FA9550-12-1-0381. I want to thank them for their generous support.

VITA

2008	Bachelor of Science, Physics, Peking University, Beijing, China
2009	Master of Science, Materials Science and Engineering, University of California, San Diego, La Jolla, California
2014	Doctor of Philosophy, Materials Science and Engineering, University of California, San Diego, La Jolla, California

Abstract of the Dissertation

Inhomogeneous Phase Transition of Vanadium Oxide on Mesoscopic Scale

by

Siming Wang

Doctor of Philosophy in Materials Science and Engineering

University of California, San Diego, 2014

Professor Ivan K. Schuller, Chair

Vanadium oxides are a prototypical family of materials that exhibit first order metal insulator transitions (MIT). In the past 15 years, the research has been focused on the role of different driving forces and the inhomogeneity in the phase transitions of vanadium oxides. Multiple stimuli, such as voltage, current and laser pulses, have been used to induce a MIT in vanadium oxides. Inhomogeneity can give rise to phase coexistence and multiple avalanches in mesoscopic scale vanadium oxides.

In this thesis, I will focus on understanding the MIT of mesoscopic vanadium oxides. I will address the phase transition mechanism through resistance – temperature (R-T) and current – voltage (I-V) characteristics. I will present the R-T characteristic of nano-sized vanadium oxide devices, which exhibits multiple avalanches over two orders of magnitude. Statistics on the avalanches indicate different MIT mechanisms for different vanadium oxides.

The I-V characteristic of micro-sized vanadium oxide devices has been previously interpreted as evidence for a voltage induced transition, a non-thermal pure electronic transition in vanadium oxides. I will present a comprehensive study of the I-V characteristic supported by various techniques, including fluorescent local temperature measurement, low temperature scanning electron microscopy and numerical simulation. The results prove that Joule heating plays a significant role in the voltage induced transition of vanadium oxides.

I will also discuss the other important aspect of the phase transition, the structural phase transition (SPT) in vanadium oxides. The SPT can be used to manipulate the magnetic properties of ferromagnetic materials, e.g. coercivity and magnetization. In a vanadium oxide/ferromagnet bilayer, the coercivity increases as the SPT occurs, due to the stress anisotropy induced by the SPT. In the special case of a V_2O_3/Ni bilayer with a smooth interface, a large coercivity enhancement appears at the middle of the V_2O_3 SPT. This effect is attributed to the phase coexistence in V_2O_3 at the nanoscale and supported by micromagnetic simulations.

Chapter I

Introduction

I.1 Electronic phenomena in transition metal oxides

For decades, transition metal oxides have been the main focus of both basic and applied research communities due to their unique electrical [1, 2], magnetic [3, 4], optical [5], thermal [6], chemical [7], and biological properties [8]. Antiferromagnets such as FeO, CoO and NiO have been studied in exchange bias systems [3]. CrO_2, a half-metal with ~100% spin polarization [4], is a good candidate material for the next generation spintronics devices [9, 10]. ZnO has been highlighted as an alternative choice to replace III-V semiconductors [5]. Resistive memory devices with NiO, CuO, TiO_2, NbO_x and $SrTiO_3$ are under development [11]. TiO_2, ZnO, WO_3 and Fe_2O_3 are important photocatalysts [7]. High temperature superconductivity in cuprates is one of the most important discovery in condensed matter physics [12]. Furthermore, several transition metal oxides exhibit a metal insulator transition (MIT), such as VO_2, V_2O_3, VO, Ti_2O_3, NbO_2, Fe_3O_4, nickelates, and manganites [1, 2, 13, 14]. Most of these oxides are strongly correlated systems, meaning that in these systems different degrees of freedom such as lattice, charge and spin, are strongly coupled. It is very challenging to unravel the physical mechanisms behind the MIT in these complex systems. The intense debates about the MITs have provided broad research opportunities for physicists and engineers.

I.2 Metal insulator transition in vanadium oxides

A first order MIT in vanadium oxides was first discovered by Morin 55 years ago [1]. As a first order phase transition [14], the MIT always occurs together with a structural phase transition (SPT). The relationship between the MIT and SPT has been long debated among theoretical and experimental physicists [15-18].

I.2.1 Vanadium dioxide (VO_2)

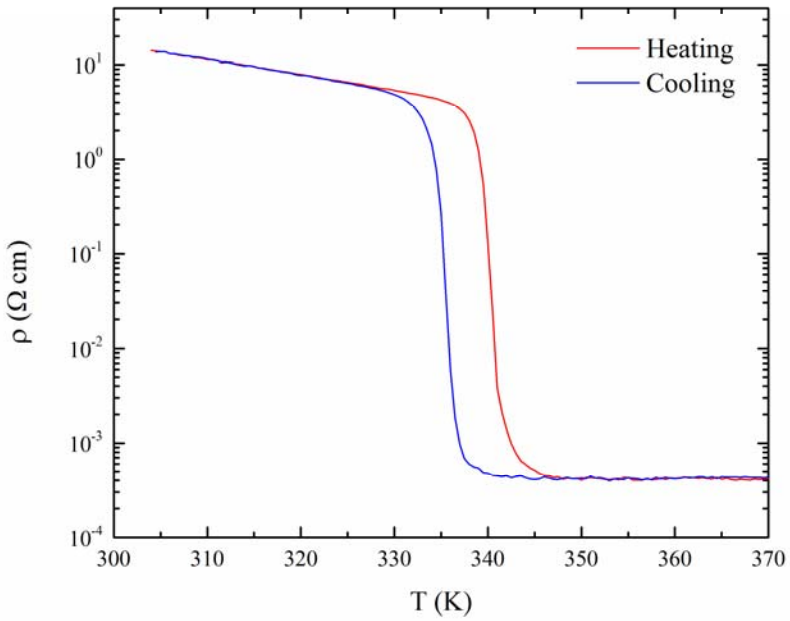

Figure 1.1. Resistivity versus temperature of a 100 nm VO_2 thin film. The red curve is the heating branch and the blue curve is the cooling branch.

The phase transition of VO_2 occurs at 340 K with a 7 – 8 K thermal hysteresis. It transitions from a low temperature, monoclinic, insulating phase to a high temperature, rutile, metallic phase. The resistivity changes by more than 4 orders of magnitude, shown in Figure 1.1. The SPT occurs simultaneously, with a lattice distortion along the c_r-axis of the rutile phase (a_m-axis of the monoclinic phase), shown in Figure 1.2. The SPT causes a crystallographic symmetry change and doubles the unit cell in the low temperature phase [19]. This can reduce the volume of the first Brillouin zone by half and open a bandgap at the Fermi surface [20]. Intensive studies have been done on VO_2 due to its application potentials. In the past 15 years, it has been shown that the MIT in VO_2 can be driven by temperature [1], voltage/current [17, 21] and femtosecond laser pulses [18].

Theories for the MIT that are based on band theory have been long established [15, 22]. Others have argued that electron-electron correlation is the driving mechanism [16, 23]. Recently, new theoretical models treating VO_2 as a hybrid of Peierls and Mott insulators have been proposed [24, 25].

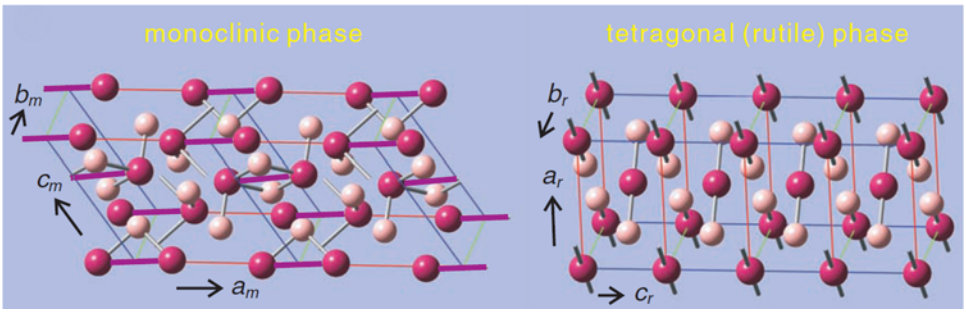

Figure 1.2. Crystal structures of VO_2 monoclinic (left) and rutile (right) phase. Vanadium atoms are depicted in red and oxygen atoms in a lighter color. From P. Baum *et al*., Science **318**, 788 (2007). Reprinted with permission from American Association for the Advancement of Science.

There are numerous experiments supporting different theoretical models for VO_2. For instance, the nanosecond voltage induced transition [17] suggests that the charge density in VO_2 can exceed the critical density [14] for Mott transition in 10 ns without causing dramatic Joule heating in VO_2. The voltage induced transition with ion liquid gating also suggests that Joule heating does not play a role because the high resistivity of the ionic liquid can avoid any current flow [26]. In-situ micrometer X-ray diffraction [27] and micro-Raman scattering [28] show that when a DC voltage induced transition occurs at room temperature, no SPT is observed on a few micrometers length scale. A recent study of VO_2 nanobeams also shows that the MIT and SPT can be decoupled when the nanobeams are suspended over a Ni, Au or Cu TEM grid [29]. A possible explanation is an interface mediated charge doping due to the metallic substrates [29]. All these experiments demonstrate that the MIT in VO_2 can be non-thermal and purely electronic, i.e. the first order phase transition that requires latent heat and an SPT can be bypassed.

On the other hand, femtosecond pump probe experiments provide evidence for a different mechanism. This type of experiments allows a temporal study of the onset of the MIT. Experiments with different pump laser intensities suggest that the laser induced MIT can be both thermal [30] and non-thermal [31], but both require latent heat and SPT. For the thermal laser induced MIT which takes place on the time scale of 100 ps, the latent heat and SPT are induced by electron-phonon thermalization [30, 32] or Joule heating [33]. For the non-thermal laser induced MIT which takes place on the time scale of 100 fs, the latent heat and SPT are induced by coherent optical phonons [31].

It is important to note that numerous experiments seem to lead to contradicting conclusions and some of these conclusions are based on inappropriate assumptions. Scanning near-field infrared microscopy has shown that the MIT of VO_2 is inhomogeneous at nanoscale, i.e. the insulating and metallic phases coexists during the phase transition [34]. Observation of multiple avalanches in VO_2 also supports that inhomogeneity is critical for the MIT [35]. To study the DC voltage and charge doping induced transitions, in-situ nanoscale temperature and structure measurements must be carried out to understand the interplay among thermal, structural and electronic effects in such an inhomogeneous system. In the nanosecond voltage induced transition, avalanche breakdown at the nanoscale must be taken into account [36]. For electrolyte gating experiments, migration of hydrogen and oxygen atoms in ionic liquid can permanently change the chemical composition of VO_2 [37, 38], which makes ionic liquid unsuitable for this type of experiments. For the laser induced transition, time dependent X-ray diffraction with femtosecond temporal resolution needs to be done to prove that the SPT occurs simultaneously with the MIT. Due to the unsolved problems in the above experiments, the mechanism of the MIT in VO_2 remains an open question. Recent photoemission spectroscopy suggests that both Peierls-like and Mott-like transitions occur in VO_2 [39].

I.2.2 Vanadium sesquioxide (V_2O_3)

V_2O_3 has been studied much less than VO_2. The phase transition of V_2O_3 occurs at 150 – 165 K with a 7 – 8 K thermal hysteresis. It transitions from a low temperature monoclinic insulating phase to a high temperature rhombohedral metallic phase. The

resistivity changes by more than 5 orders of magnitude, shown in Figure 1.3. A difference between VO_2 and V_2O_3 is that the SPT of V_2O_3 does not cause a doubling of the unit cell in the insulating phase [40]. However, an antiferromagnetic phase formed simultaneously at low temperature with the MIT causes the volume of the unit cell doubling in the insulating phase [41], shown in Figure 1.4. V_2O_3 has been categorized as a Mott insulator by theoreticians [14]. Based on this theoretical argument, it is possible to observe a purely electronic transition and the decoupling of the MIT and SPT. Previous research on V_2O_3 includes doping and high pressure experiments on single crystals [42]. Voltage induced transition experiments and femtosecond pump probe experiments have not been systematically performed on V_2O_3 until very recently [43, 44]. Many experiments that have been done on VO_2 can be repeated on V_2O_3. One can expect V_2O_3 to share some similar physical properties with VO_2, because the MIT in VO_2 and V_2O_3 are both first order phase transitions. On the other hand, the electronic properties of V_2O_3 could be different from VO_2, because of the magnetic phase transition which only occurs in V_2O_3. These similarities and differences will deepen our knowledge about MITs in transition metal oxides.

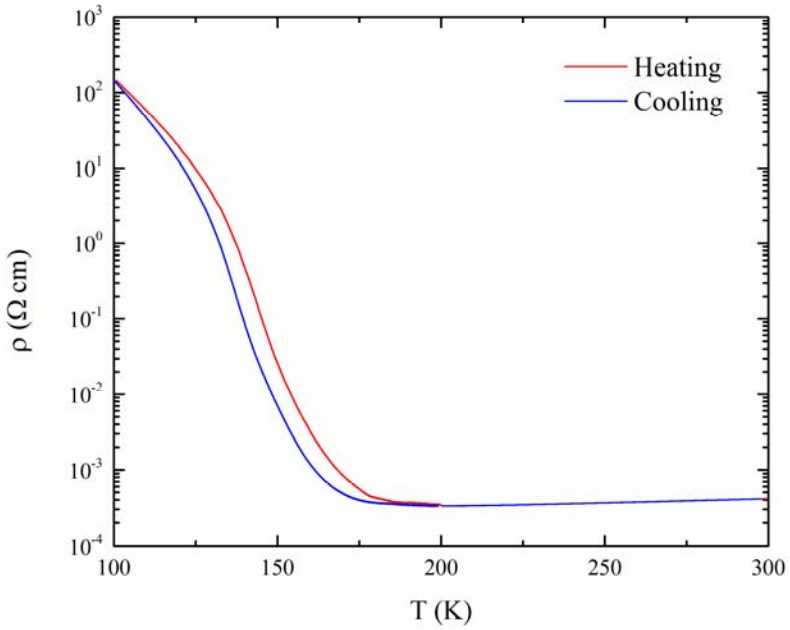

Figure 1.3. Resistivity versus temperature of a 100 nm V_2O_3 thin film. The red curve is the heating branch and the blue curve is the cooling branch.

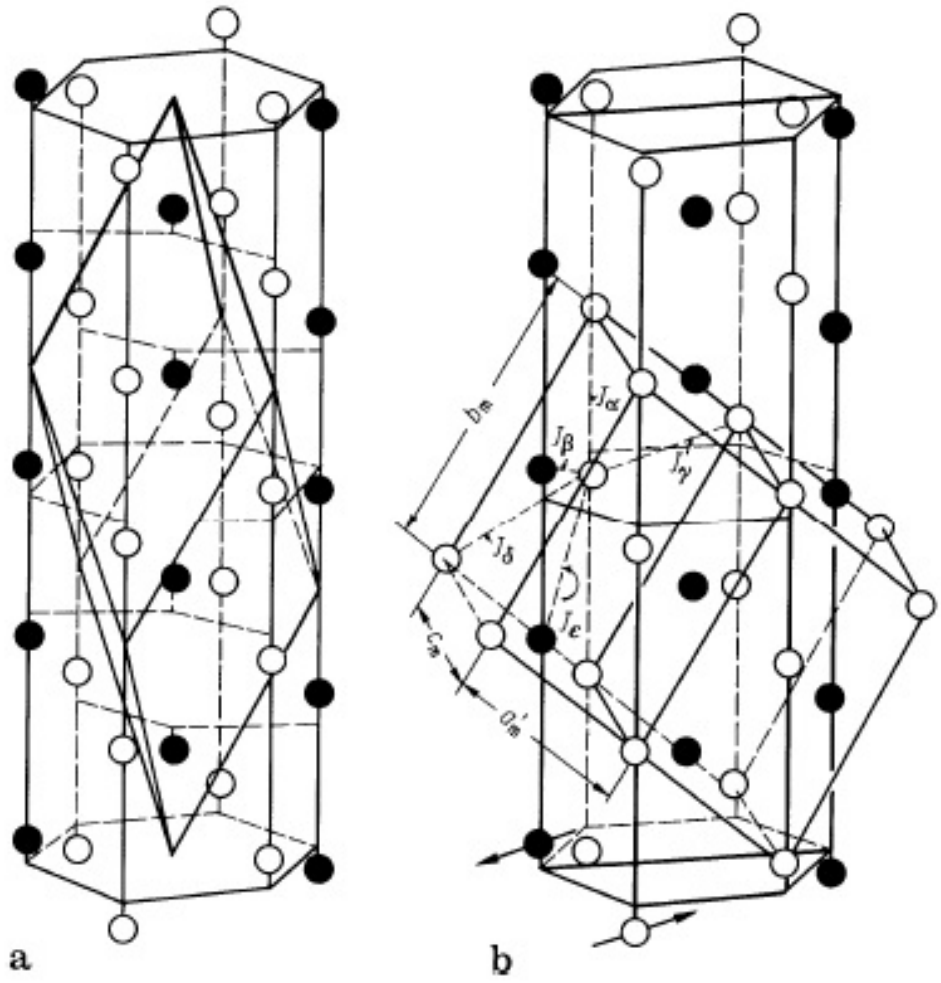

Figure 1.4. Crystallographic symmetries of V_2O_3 corundum (a) and monoclinic (b) phase. The primitive rhombohedral axes are shown as bold lines in (a); the primitive monoclinic axes are shown as bold lines in (b). The spins on the filled circles are opposite to those on the open circles. Reprinted with permission from R. E. Word *et al*., Phys. Rev. B **23**, 3533 (1981). Copyright (1981) by the American Physical Society.

In this thesis, I will focus on comparing the phase transition of VO_2 and V_2O_3 at the mesoscopic scale including the temperature induced MIT, the voltage induced MIT and the proximity effect with other materials. VO_2 and V_2O_3 thin films are deposited with RF magnetron sputtering and characterized with X-ray diffraction and scanning electron microscopy; microdevices and nanodevices are fabrication with various lithographic

techniques. Avalanches are observed in both VO_2 and V_2O_3 nanodevices when the MIT is induced by temperature, but statistics show that the MIT in VO_2 and V_2O_3 may occur through different mechanisms. The voltage induced MIT are in both VO_2 and V_2O_3 microdevices, and Joule heating is found to play a predominant role. The SPT of VO_2 and V_2O_3 can be used to modify the magnetic properties of ferromagnetic materials. The detailed studies of VO_2 and V_2O_3 will be presented in the following four chapters of this thesis.

I.3 References

[1] F. J. Morin, Phys. Rev. Lett. **3**, 34 (1959).

[2] F. Walz, J. Phys.: Condens. Matter **14**, R285 (2002).

[3] J. Nogues and I. K. Schuller, J. Magn. Magn. Mater. **192**, 203 (1999).

[4] K. Schwarz, J. Phys. F: Met. Phys. **16**, L211 (1986).

[5] U. Özgür, Y. I. Alivov, C. Liu, A. Teke, M. A. Reshchikov, S. Dogan, V. Avrutin, S.-J. Cho, and H. Morkoc, J. Appl. Phys. **98**, 041301 (2005).

[6] S. Walia, S. Balendhran, H. Nili, S. Zhuiykov, G. Rosengarten, Q. H. Wang, M. Bhaskaran, S. Sriram, M. S. Strano, and K. Kalantar-zadeh, Prog. Mater. Sci. **58**, 1443 (2013).

[7] H. Zhang, G. Chen, and D.W. Bahnemann, J. Mater. Chem. **19**, 5089 (2009).

[8] Q. A. Pankhurst, J. Connolly, S. K. Jones, and J. Dobson, J. Phys. D: Appl. Phys. **36**, R167 (2003).

[9] J. Lu, K. G. West, and S. A. Wolf, Chapter 3 in *Thin Film Metal-Oxides*, edited by S. Ramanathan, (Springer, New York, 2010).

[10] *Nanoscale Magnetic Materials and Applications*, edited by J. P. Liu, E. Fullerton, O. Gutfleisch, and D. J. Sellmyer, (Springer, Berlin, 2009).

[11] R. Waser, R. Dittmann, G. Staikov, and K. Szot, Adv. Mater. **21**, 2632 (2009).

[12] J. G. Bednorz and K. A. Mulller, Z. Phys. B Con. Mat. **64**, 189 (1986).

[13] M. Imada, A. Fujimori, and Y. Tokura, Rev. Mod. Phys. **70**, 1039 (1998).

[14] N. F. Mott, *Metal-Insulator Transitions*, second edition (Tayler & Francis, London, 1990).

[15] R. M. Wentcovitch, W. W. Schultz, and P. B. Allen, Phys. Rev. Lett. **72**, 3389 (1994).

[16] T. M. Rice, H. Launois, and J. P. Pouget, Phys. Rev. Lett. **73**, 3042 (1994).

[17] G. Stefanovich, A. Pergament, and D. Stefanovich, J. Phys.: Condens. Matter **12**, 8837 (2000).

[18] A. Cavalleri, Cs. Toth, C. W. Siders, J. A. Squier, F. Raksi, P. Forget, and J. C. Kieffer, Phys. Rev. Lett. **87**, 237401 (2001).

[19] G. Andersson, Acta Chem. Scand. **8**, 1599 (1954).

[20] C. Kittel, *Introduction To Solid State Physics*, 8th edition (John Wiley & Sons, Philadelphia, 2004).

[21] H.-T. Kim, B.-G. Chae, D.-H. Youn, S.-L. Maeng, G. Kim, K.-Y. Kang, and Y.-S. Lim, New J. Phys. **6**, 52 (2004).

[22] J. B. Goodenough, Phys. Rev. **117**, 1442 (1960).

[23] A. Zylbersztejn and N. F. Mott, Phys. Rev. B **11**, 4383 (1975).

[24] S. Biermann, A. Poteryaev, A. I. Lichtenstein, and A. Georges, Phys. Rev. Lett. **94**, 026404 (2005).

[25] C. Weber, D. D. O'Regan, N. D. M. Hine, M. C. Payne, G. Kotliar, and P. B. Littlewood, Phys. Rev. Lett. **108**, 256402 (2012).

[26] M. Nakano, K. Shibuya, D. Okuyama, T. Hatano, S. Ono, M. Kawasaki, Y. Iwasa, and Y. Tokura, Nature **487**, 459 (2012).

[27] B.-J. Kim, Y. W. Lee, S. Choi, J.-W. Lim, S. J. Yun, H.-T. Kim, T.-J. Shin, and H.-S. Yun, Phys. Rev. B **77**, 235401 (2008).

[28] H.-T. Kim, B.-G. Chae, D.-H. Youn, G. Kim, K.-Y. Kang, S.-J. Lee, K. Kim, and Y.-S. Lim, Appl. Phys. Lett. **86**, 242101 (2005).

[29] Z. Tao, T.-R. T. Han, S. D. Mahanti, P. M. Duxbury, F. Yuan, C.-Y. Ruan, K. Wang, and J. Wu, Phys. Rev. Lett. **109**, 166406 (2012).

[30] D. J. Hilton, R. P. Prasankumar, S. Fourmaux, A. Cavalleri, D. Brassard, M. A. El KhaKani, J. C. Kieffer, A. J. Taylor, and R. D. Averitt, Phys. Rev. Lett. **99**, 226401 (2007).

[31] A. Cavalleri, Th. Dekorsy, H. H. W. Chong, J. C. Kieffer, and R. W. Schoenlein, Phys. Rev. B **70** 161102 (2004).

[32] R. D. Averitt and A. J. Taylor, J. Phys.: Condens. Matter **14**, R1357 (2002).

[33] M. Liu, H. Y. Hwang, H. Tao, A. C. Strikwerda, K. Fan, G. R. Keiser, A. J. Sternbach, K. G. West, S. Kittiwatanakul, J. Lu, S. A. Wolf, F. G. Omenetto, X. Zhang, K. A. Nelson, R. D. Averitt, Nature **487**, 345 (2012).

[34] M. M. Qazilbash, M. Brehm, B.-G. Chae, P.-C. Ho, G. O. Andreev, B.-J. Kim, S. J. Yun, A. V. Balatsky, M. B. Maple, F. Keilmann, H.-T. Kim, and D. N. Basov, Science **318**, 1750 (2007).

[35] A. Sharoni, J. G. Ramírez, and I. K. Schuller, Phys. Rev. Lett. **101**, 026404 (2008).

[36] X. Zhong, X. Zhang, A. Gupta, and P. LeClair, J. Appl. Phys. **110**, 084516 (2011).

[37] H. Ji, J. Wei, and D. Natelson, Nano Lett. **12**, 2988 (2012).

[38] J. Jeong, N. Aetukuri, T. Graf, T. D. Schladt, M. G. Samant, and S. S. P. Parkin, Science **339**, 1402 (2013).

[39] J. Laverock, A. R. H. Preston, D. Newby, Jr., K. E. Smith, S. Sallis, L. F. J. Piper, S. Kittiwatanakul, J. W. Lu, S. A. Wolf, M. Leandersson, and T. Balasubramanian, Phys. Rev. B **86**, 195124 (2012).

[40] P. D. Dernier and M. Marezio, Phys. Rev. B **2**, 3771 (1970).

[41] S. Di Matteo, N. B. Perkins, and C. R. Natoli, Phys. Rev. B **65** 054413 (2002).

[42] D. B. McWhan, J. P. Remeika, T. M. Rice, W. F. Brinkman, J. P. Maita, and A. Menth, Phys. Rev. Lett. **27**, 941 (1971).

[43] S. Guénon, S. Scharinger, S. Wang, J. G. Ramirez, D. Koelle, R. Kleiner, and I. K. Schuller, EPL **101**, 57003 (2013).

[44] M. K. Liu, B. Pardo, J. Zhang, M. M. Qazilbash, S. J. Yin, Z. Fei, J.-H. Shin, H.-T. Kim, D. N. Basov, R. D. Averitt, Phys. Rev. Lett. **107**, 066403 (2011).

Chapter II

Thin film deposition, characterization and device fabrication

II.1 Introduction

Due to the potential technological applications [1] of vanadium oxide thin films and nanostructures, its synthesis has been a major focus for solid state physicists and materials scientists [2]. As a transition metal, vanadium exhibits multiple valence states in oxide and other compounds. This gives rise to a rich variety of oxides with various stoichiometries [3] and polymorphic phases [4]. It is challenging to synthesize single phase VO_2 or V_2O_3, due to the existence of stable phases in between V^{3+} an V^{4+}, also known as Magneli phases (V_nO_{2n-1}) [3]. The growth of vanadium oxide thin films has been successfully performed with various techniques, including chemical vapor deposition [5], the sol-gel method [6], sputtering [7], pulsed laser deposition [8], ion beam deposition [9], e-beam evaporation [10] and thermal evaporation [11]. During the reactive synthesis of vanadium oxides, many parameters, including target material [12], gas pressure [3], substrate orientation [13], deposition temperature [3], power input [14], annealing temperature and time [15] need to be precisely controlled to achieve the correct stoichiometry. A change in the deposition condition can cause changes in the properties of the metal insulator transition (MIT), including the transition temperature [3], the magnitude of the MIT [3], the width of the thermal hysteresis [16] and the slope of the resistance versus temperature (R-T) characteristic $\frac{dR}{dT}$ [16]. Nanostructures of vanadium oxides such as nanoparticles [17] and nanobeams [18] have been synthesized and investigated. Micro-

and nano-sized devices in both vertical and planar geometries have been fabricated on vanadium oxide thin films [19, 20].

In this chapter, I will present a study of vanadium oxide thin film growth and device fabrication. I successfully prepared single phase textured VO_2 and V_2O_3 films with reactive RF magnetron sputtering by controlling the oxygen flow, substrate temperature, RF power and substrate orientation. R-T characteristics of the films were measured to determine the optimal deposition conditions. Structural characterization techniques including X-ray diffraction (XRD) and scanning electron microscopy (SEM) were employed to study the crystal orientation and the surface morphology of the films. I also successfully fabricated micro- and nano-sized devices in planar geometry with vanadium oxide films. The lithographic techniques include electron beam lithography, photolithography, reactive ion etching (RIE) and sputtering coating. The fabrication procedures for each technique will be described in detail.

II.2 Reactive sputtering growth of vanadium oxides

II.2.1 VO_2 growth with various oxygen partial pressures and substrate temperatures

In this section, I will present the reactive sputtering growth conditions for VO_2 thin films. Sputtering growth is performed in a high vacuum chamber with a base pressure of 2 $\times 10^{7}$ Torr. The target material is V_2O_3 (1.5" diameter × 0.125" thick, 99.7 – 99.9 % ACI Alloys Inc.). For all of the depositions, the RF power is kept at 100 W and the substrate is

r-plane sapphire. The oxygen flow and substrate temperature is controlled to optimize the growth condition.

It is important to clean the sapphire substrates before vanadium oxide thin films are deposited. The sapphire substrates are cleaned using the following produce:

(1) 15 min ultrasonication bath in DI water, which removes inorganic contaminates.

(2) 15 min ultrasonication bath in acetone, which removes organic contaminates.

(3) 15 min ultrasonication bath in methanol, which removes the acetone from the previous step.

(4) The substrate is dried with high purity nitrogen.

The sputtering procedure is described as follows:

(1) The substrate temperature is increased to the deposition temperature at a rate of 13 °C/min.

(2) A 10 min presputtering is performed with pure argon gas to clean the surface of the target material.

(3) A 30 min presputtering is performed with an argon/oxygen mixture to establish a stable plasma for the deposition. The percentage of oxygen is optimized for the correct stoichiometry.

(4) A 140 min sputtering is performed with the same argon/oxygen mixture as the previous step to deposit VO_2 thin films with ~ 100 nm thickness. The VO_2 film thickness is measured with a Dektak 150 surface profiler after removed from the vacuum chamber.

(5) The substrate temperature is decreased to room temperature at a rate of 13 °C/min.

It is important to note that in order to obtain high quality VO_2 films, it is very important to control the partial pressure of oxygen in the chamber. The oxygen in the chamber can modify the stoichiometry of the target material and cause a change in the sputtering rate and the oxidation rate of the films. This delicate balance is a difficulty in the growth of VO_2 thin films.

We control the gas flow rate and pumping speed simultaneously. We use MKS RS-485 mass flow controllers (10 sccm full scale and 1% precession) to inject ultrahigh purity (99.999%) argon and an 80% argon/20% oxygen mixture into the vacuum chamber. We installed a pneumatic valve with an adjustable intermediate position between the vacuum chamber and the main turbo pump. We adjust the intermediate position of the valve to obtain a 1:1 ratio between the gas flow (sccm) and the pressure (mTorr) in the chamber as shown in Figure 2.1. The total gas pressure is kept at 4 mTorr during the sputtering process. Using this process, the oxygen percentage is controlled with 0.5% accuracy.

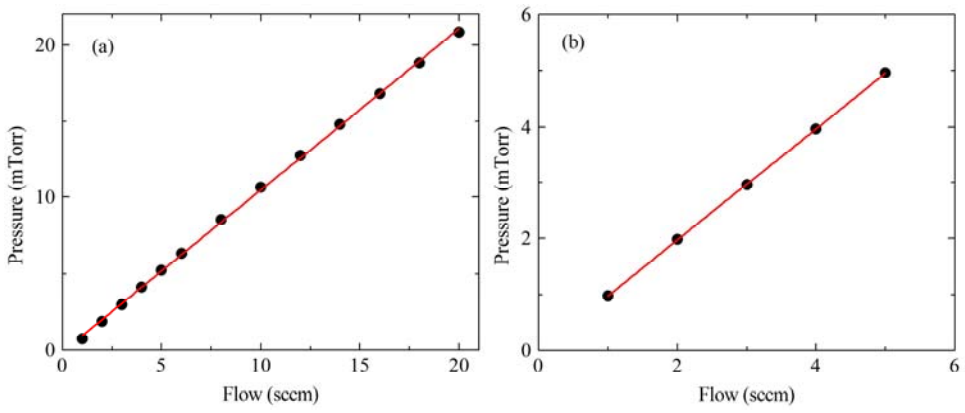

Figure 2.1. (Black circles) 1:1 ratio between the gas flow (sccm) and pressure (mTorr) in the chamber. (a) Argon and (b) argon/oxygen mixture. The red lines are linear fits of the data.

Figure 2.2 shows the effect of the oxygen concentration on the MIT of VO_2 thin films. The substrate temperature is fixed at 600 °C for all the depositions. From 5% oxygen, the magnitude of the MIT, indicated by the R-T characteristics, increases with oxygen percentage. At 7.5 – 8.5% oxygen, a MIT of more than 4 orders of magnitude is observed. Up to 10% oxygen, the 4 orders of magnitude MIT remains. However, the film becomes visibly inhomogeneous as the oxygen percentage reaches 10%. The resistance of the insulating phase increases with the increasing oxygen percentage monotonically while the resistance of the metallic phase reaches a minimum at 6.5 – 8.5% oxygen. For 6.5% and 7.5% oxygen, the heat and cooling branches of the R-T curves remain different until 350 – 360 K. This indicates an inhomogeneous stoichiometry in the film, causing a width distribution of the transition temperature. For these reasons, we choose 8.5% oxygen percentage as the optimal condition for VO_2 film deposition.

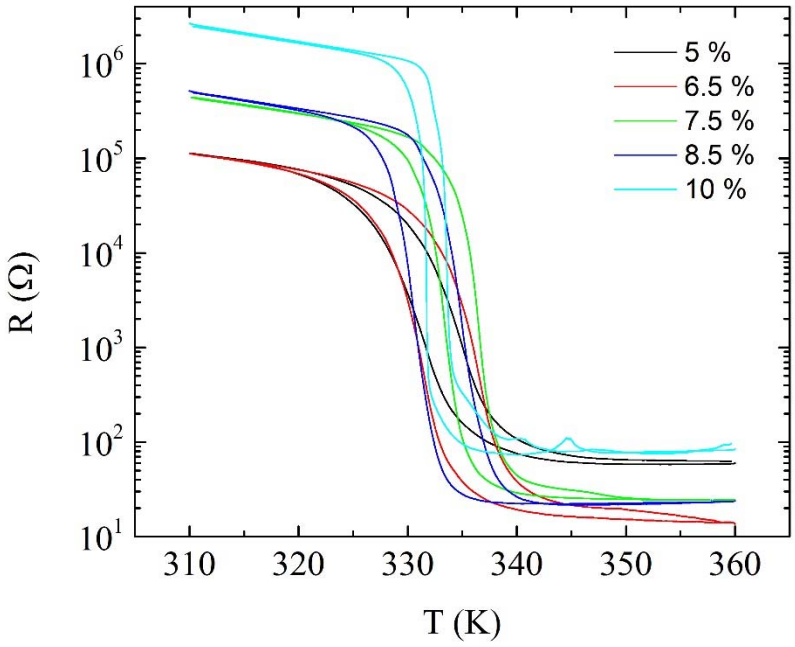

Figure 2.2. R-T characteristics of VO_2 thin films deposited with different oxygen percentages: 5% (black curve), 6.5% (red curve), 7.5% (green curve), 8.5% (blue curve) and 10% (cyan curve). The resistance of the VO_2 film is measured in a 2-probe configuration. The resistance of the cables is 2 – 3 Ω.

The VO_2 growth is sensitive to the substrate temperature as well. We place the sapphire substrates on an inconel (austenitic nickel-chromium-based high-performance alloy) sample holder with two clamps. The back side of the sample holder is heated by infrared radiation from two halogen lamps. A K-type thermocouple is placed between the two halogen lamps and close to the back side of the sample holder. The power output of the halogen lamps is controlled by a heater controller with a proportional-integral-derivative (PID) feedback circuit to stabilize the temperature readout from the thermocouple. Note that the temperature readout from the thermocouple is different than

the temperature of the sapphire substrate mounted on the front side of the sample holder, because a temperature gradient exists between the two sides of the sample holder. To control the substrate temperature accurately, we performed a temperature calibration by placing a K-type thermocouple on the surface of the sample holder. As shown in Figure 2.3, we recorded the temperature readout from the heater controller and the substrate temperature simultaneously. According to the calibration curve, a 50 °C temperature increase in the heater controller gives rise to a ~ 40 °C temperature increase in the substrate.

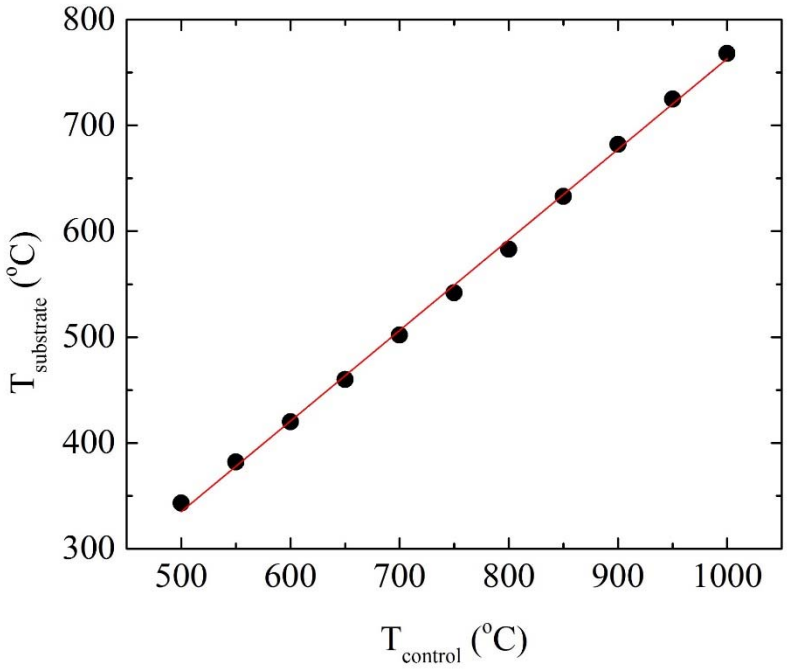

Figure 2.3. Black circles: temperature calibration, showing substrate temperature $T_{substrate}$ vs. heater controller temperature readout $T_{control}$. Red line: linear fit of the data.

Figure 2.4 shows the MIT of VO_2 films deposited at various substrate temperatures. From a substrate temperature of 500 °C, the magnitude of the MIT increases with increasing substrate temperatures. For a substrate temperature of 600 °C, the magnitude of the MIT reaches a maximum. For a substrate temperature of 650 °C, the magnitude of the MIT starts to decrease and the films become visibly inhomogeneous. The resistance of the insulating phase increases monotonically with increasing substrate temperature. The resistance of the metallic phase shows a minimum for the substrate temperature of 600 °C. We choose a substrate temperature of 600 °C as the optimal condition for the VO_2 film deposition.

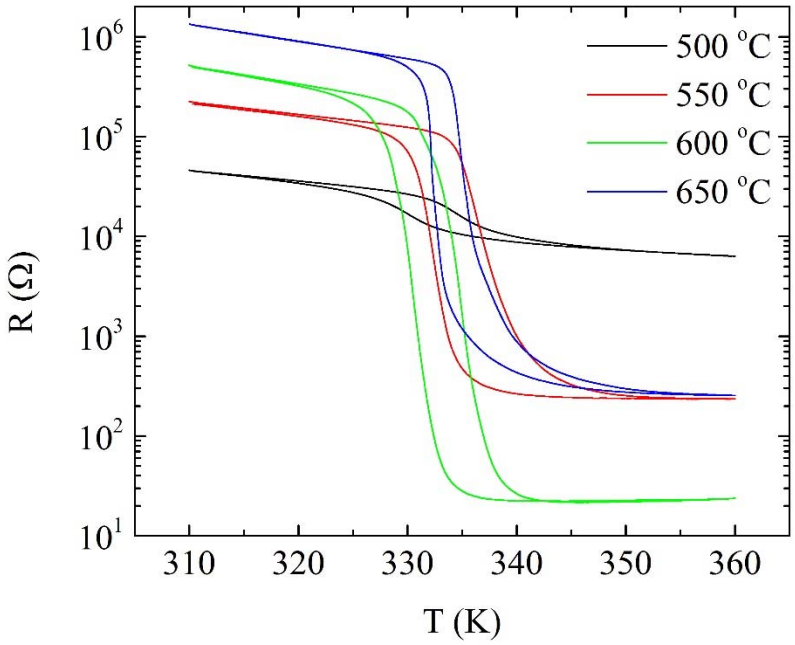

Figure 2.4. R-T characteristics of VO_2 thin films deposited at different substrate temperatures: 500 °C (black curve), 550 °C (red curve), 600 °C (green curve) and 650 °C (blue curve).

II.2.2 V_2O_3 growth with various oxygen partial pressures, substrate temperatures and orientations

In this section, I will present the reactive sputtering growth conditions for V_2O_3 thin films. The sputtering growth is performed in the same high vacuum chamber used for VO_2 growth, with a base pressure of 2×10^{7} Torr. The target material is V_2O_3 (1.5" diameter × 0.125" thick, 99.7 – 99.9% ACI Alloys Inc.). For all of the depositions, the RF power is kept at 100 W and the gas pressure is kept at 4 mTorr. The oxygen flow, substrate temperature and orientation are controlled to optimize the growth conditions.

The sputtering procedure is described as follows:

(1) The substrate temperature is increased to the deposition temperature at a rate of 13 °C/min.

(2) A 10 min presputtering is performed with pure argon gas to clean the surface of the target material.

(3) A 25 min sputtering is performed to deposit V_2O_3 thin films with ~ 100 nm thickness. The V_2O_3 film thickness is measured by low angle X-ray reflectivity after removed from the vacuum chamber, which will be discussed in the next section.

(4) The substrate temperature is decreased to room temperature at a rate of 13 °C/min.

The V_2O_3 growth is more sensitive to oxygen than VO_2. Figure 2.5 shows the effect of the oxygen percentage on the MIT of V_2O_3 thin films. The substrate temperature is fixed at 750 °C for both depositions. For 0% oxygen, the MIT is approximately 5 orders of magnitude. However, even 0.5% oxygen can suppress the MIT to less than one order of

magnitude. This indicates that the MIT of V_2O_3 is more sensitive to oxygen stoichiometry than VO_2. All the V_2O_3 films used in the rest of this thesis are deposited in pure argon gas without any oxygen flow.

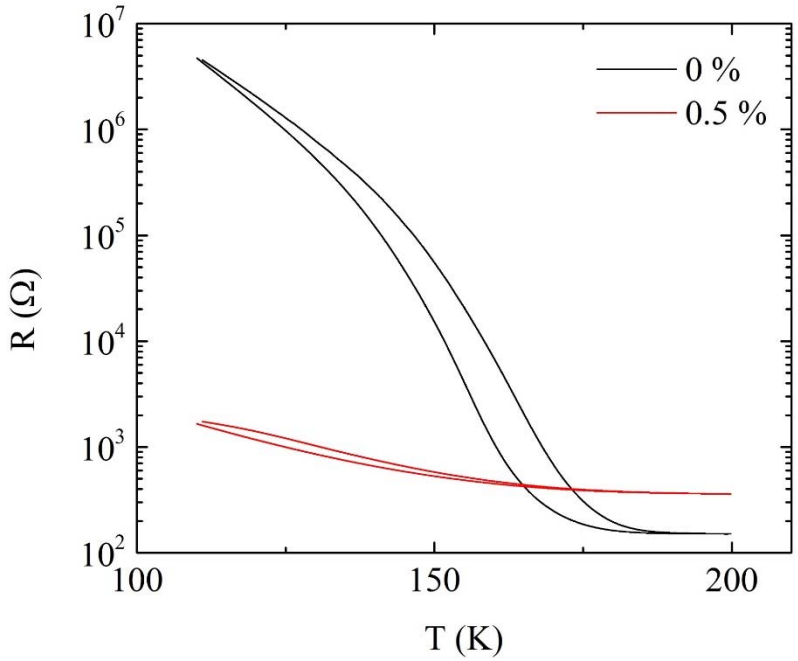

Figure 2.5. R-T characteristics of V_2O_3 thin films deposited with different oxygen percentages: 0% (black curve) and 0.5% (red curve).

The V_2O_3 growth is also sensitive to the substrate temperature. Figure 2.6 shows the effect of the substrate temperature on the MIT of V_2O_3 thin films. For a substrate temperature of 650 °C, the magnitude of the MIT increases with the increasing substrate temperature. At a substrate temperature of 750 °C, a MIT of ~ 5 orders of magnitude is observed. This temperature is the highest possible in our sputtering system. The resistance

of the insulating phase of V_2O_3 increases monotonically with increasing substrate temperature while the resistance of the metallic phase is not sensitive to the substrate temperature. We choose a substrate temperature of 750 °C as the optimal condition for the V_2O_3 thin film deposition.

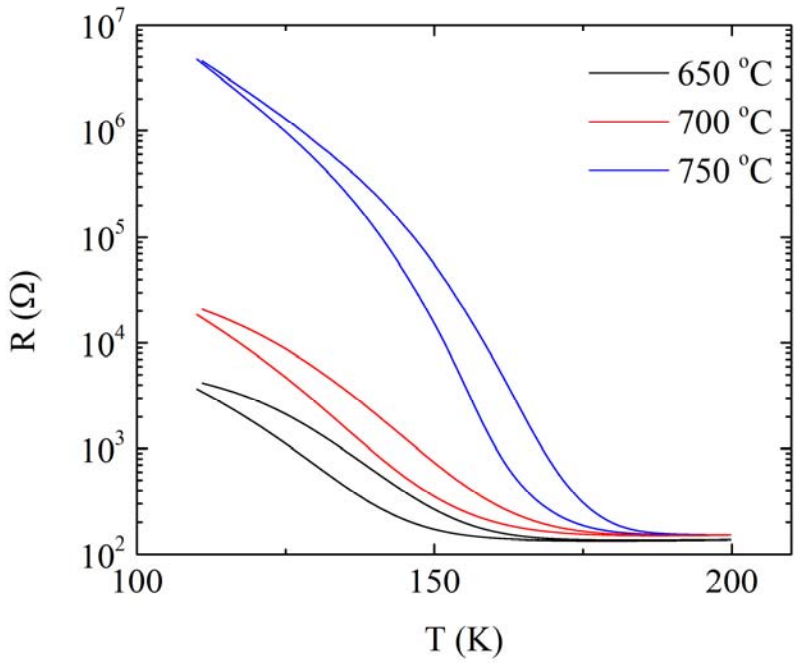

Figure 2.6. R-T characteristics of V_2O_3 thin films deposited at different substrate temperatures: 650 °C (black curve), 700 °C (red curve) and 750 °C (blue curve).

We deposited V_2O_3 films on sapphire substrates of different crystal orientations including r-, a-, m- and c-plane substrates. V_2O_3 has the same crystal symmetry as sapphire. The V_2O_3 films always grow in the same crystal orientation as the sapphire substrate they are grown on. We observed MITs in all the V_2O_3 films, regardless of orientation. However,

the R-T characteristics of the V_2O_3 films deposited on different sapphire substrates are different. For the V_2O_3 film deposited on r-plane sapphire, the MIT temperature is the same as that of the bulk, 150 – 165 K. The MIT is about 5 orders of magnitude and the thermal hysteresis is 10 K. For the V_2O_3 film deposited on m-plane sapphire, the MIT temperature is higher than that of the bulk, 170 K. The MIT is about 4 orders of magnitude and the thermal hysteresis – 5K – is smaller than that of the film deposited on r-plane sapphire. For the V_2O_3 film deposited on a-plane sapphire, the MIT temperature is lower than that of the bulk, 120 K. The MIT is about 6 orders of magnitude and the thermal hysteresis – 15K – is larger than that of the film deposited on r-plane sapphire. Note that the R-T characteristic for the V_2O_3 deposited on a-plane sapphire saturates below 100 K at 120 MΩ, because with 100 nA applied current the voltage on the film is about 12 V, which is the compliance voltage of the current source. For the V_2O_3 film deposited on c-plane sapphire, the MIT temperature is lower than that of the bulk, 120 K. The MIT is only one order of magnitude and the thermal hysteresis is 10 K. It has been reported previously that V_2O_3 films grown on c-plane sapphire by reactive DC magnetron sputtering [21] and oxygen plasma-assisted thermal evaporation [22, 23] exhibit 5 – 6 orders of magnitude MIT. The origin of the difference in the MIT temperatures of the V_2O_3 films grown on different sapphire substrates remains an open question. A possible explanation could be that different sapphire substrates induce different types of stress in the V_2O_3 films. A tensile stress can decrease the MIT temperature of V_2O_3 [24] while a compressive stress can do the opposite. The V_2O_3 films on a- and c-plane sapphire might be under tensile stress while the V_2O_3 films on m-plane might be under compressive stress. The stress in the V_2O_3 films could be

investigated by in-situ wafer curvature measurements [25], but that is beyond the scope of this thesis.

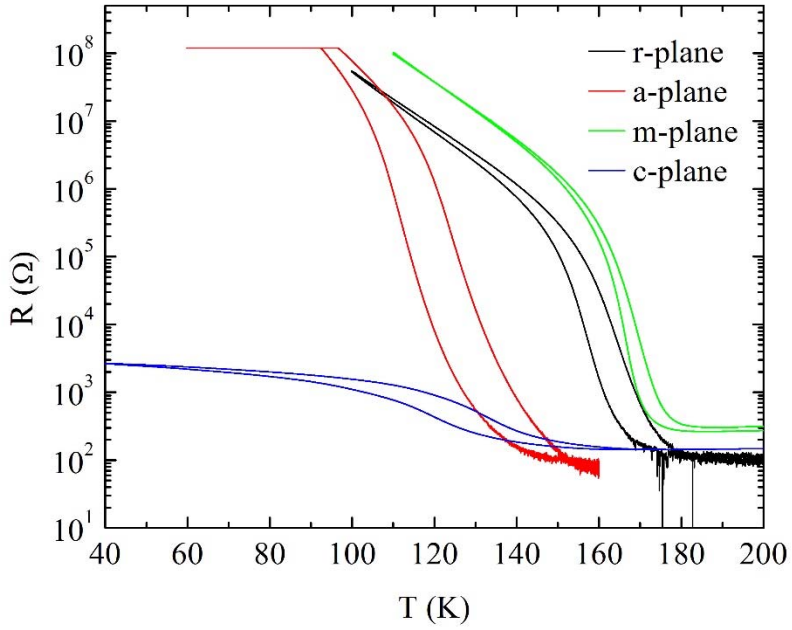

Figure 2.7. R-T characteristics of V_2O_3 thin films deposited on sapphire substrates of different orientations: r-plane (black curve), a-plane (red curve), m-plane (green) and c-plane (blue curve).

II.3 Structural Characterization

II.3.1 X-ray diffraction

I performed low angle ($2\theta < 5°$) X-ray reflectivity (XRR) and high angle ($2\theta > 10°$) X-ray diffraction (XRD) to characterize the film thickness, surface roughness and crystal orientation of vanadium oxides at room temperature. 2θ is the angle between the incident

and diffracted X-ray beam. All the measurements are performed on a Bruker D8 Discovery rotating anode diffractometer using CuKα radiation. The X-ray wavelength is 1.54 Å. The measurements are performed using the following procedure:

(1) Detector scan at ω = 0. Scan 2θ from -0.2 to 0.2° to maximize the intensity in the detector.

(2) z scan. Block half of the X-ray beam with the substrate.

(3) ω scan (rocking curve) at 2θ = 0. Locate the ω with the maximum intensity and align the diffractometer to the surface of the substrate.

(4) Repeat z scan.

If low angle XRR is performed,

(5) ω scan at 2θ = 1. Locate the ω with the maximum intensity and align the diffractometer to the surface of the substrate.

(6) 2θ/ω scan from 0 – 5°.

If high angle XRD is performed,

(5) ω scan at the out-of-plane 2θ of the sample. Locate the ω with the maximum intensity and align the diffractometer to the out-of-plane 2θ of the sample.

(6) 2θ/ω scan around the out-of-plane 2θ of the sample (± 2°). Locate the 2θ with the maximum intensity.

(7) Repeat ω scan at the out-of-plane 2θ of the sample.

(8) Chi (χ) scan at the out-of-plane 2θ of the sample. Locate the Chi with the maximum intensity.

(9) Repeat ω scan at the out-of-plane 2θ of the sample.

(10) 2θ/ω scan from 0 – 90°.

Figure 2.8(a) shows the low angle XRR of a 100 nm VO_2 film. The x-axis is the scattering vector Q_Z calculated from the 2θ = 0 – 5° with Equation (2.1):

$$Q_Z = \frac{4\pi}{\lambda} sin\theta \tag{2.1}$$

where λ is the wavelength of the X-ray. As Q_Z increases, no oscillations in the intensity is observed, indicating a high surface roughness.

Figure 2.8(b) shows the high angle XRD with the diffractometer aligned to the sapphire (012), substrate surface and VO_2 in the monoclinic phase (200). Note that except for the highlighted peaks at 37.1° (black square) and 79° (red circle) from the VO_2 monoclinic (200) and (400) respectively, all the other peaks come from the sapphire substrate. The intensities of the sapphire peaks are different by as much as 4 orders of magnitude with the diffractometer aligned to the sapphire (012) and substrate surface, meaning that there is a miscut between the sapphire (012) and substrate surface. In addition, the intensity of the VO_2 monoclinic (200) peak at 37.1° varies by less than a factor of two, indicating that the VO_2 film is not a single crystal. The VO_2 monoclinic (200) plane can orient differently among the grains and a twinning (-211) exists, which also broadens the diffraction peak. A diffraction peak at 11.7° (blue triangle) with an intensity above the noise level is also observed. This peak does not belong to any VO_2 phases but comes from

the V_5O_9 triclinic (001) plane. V_5O_9 is one of the non-stoichiometric Magneli phase formed between V_2O_3 and VO_2 [3], indicating that a small fraction of VO_2 film has oxygen vacancies. V_5O_9 exhibits an MIT at 129 – 135 K [26].

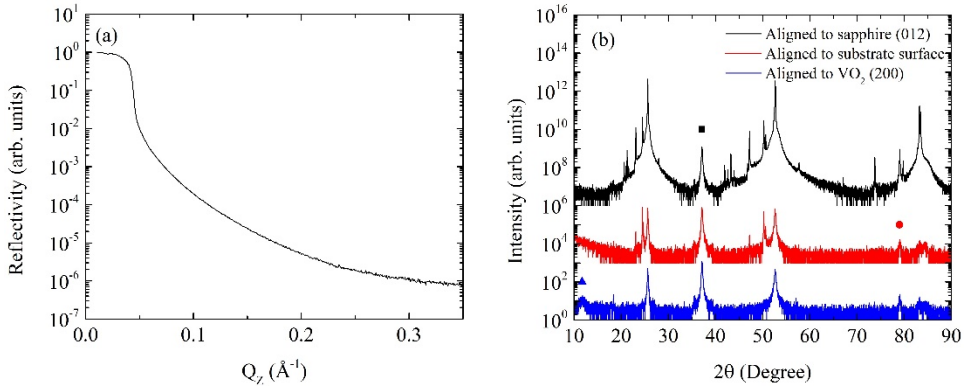

Figure 2.8. (a) Low angle XRR of a 100 nm VO_2 film. (b) High angle XRD of the same VO_2 film with the X-ray diffractometer aligned to the sapphire (012) (black curve), substrate surface (red curve) and VO_2 monoclinic (200) (blue curve). VO_2 monoclinic (200) (black square), (400) (red circle) and V_5O_9 triclinic (001) (blue triangle) are indicated. All the other peaks are from the sapphire substrate. The curves are shifted along the y-axis for visual clarity.

As discussed in the previous section, the VO_2 film deposited at 500 K shows a two orders of magnitude higher resistance than one deposited at 600 K in the metallic phase, shown in Figure 2.4. This is caused by the VO_2(B) phase, which is formed at a substrate temperature of 500 K. Figure 2.9 shows the high angle XRD of VO_2 films deposited at 500 K and 600 K with the diffractometer aligned to the sapphire (012). For the VO_2 film deposited at 600 K, the VO_2 monoclinic (200) peak at 37.1° is observed (black square). For the VO_2 film deposited at 500 K, no VO_2 monoclinic (200) peak at 37.1° is observed above the noise level. This indicates that the VO_2 monoclinic phase grows in different crystal

orientations. Diffraction peaks from the (001) planes of the VO_2(B) phase are observed at 14.45°, 29.11° and 44.36° (red circles). VO_2(B) phase is a polymorphic VO_2 phase with a base-centered monoclinic crystal structure and does not exhibit a MIT [4]. To study the physical properties of the VO_2(B) phase, single phase VO_2(B) films can be deposited, but that is beyond the scope of this thesis.

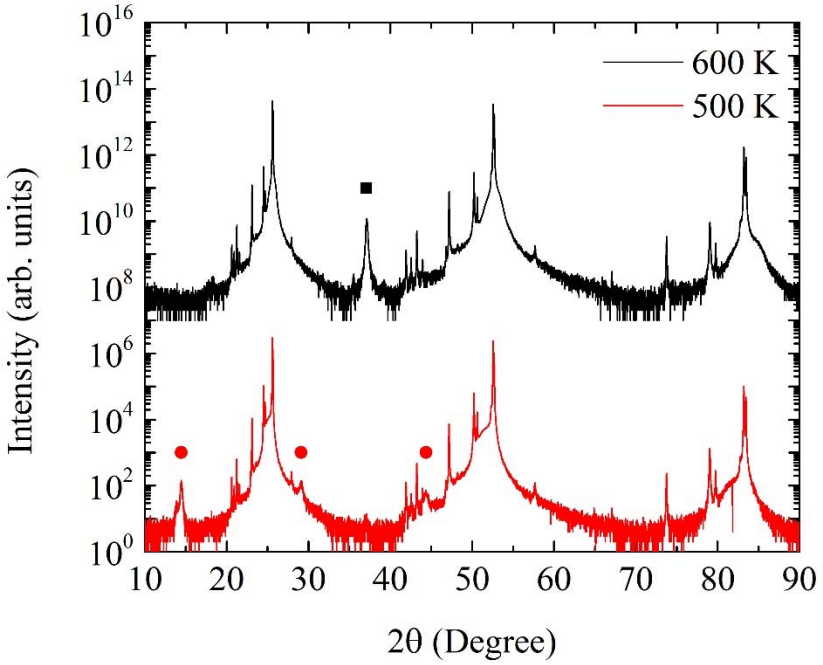

Figure 2.9. High angle XRD of VO_2 films deposited at 600 K (black curve) and 500 K (red curve). The VO_2 monoclinic (200) (black square) and VO_2(B) (001), (002) and (003) (red circles) are indicated. All the other peaks are from the sapphire substrate. The curves are shifted along the y-axis for visual clarity.

Figure 2.10(a) shows the low angle XRR of a V_2O_3 film. Oscillations in the intensity are observed for $Q_Z > 0.05$ Å^{-1}. The experimental data is fitted with a reflectivity

analysis package (MOTOFIT) for the co-refinement of multiple-contrast neutron and X-ray reflectometry data [27]. The fitting cannot be optimized with one V_2O_3 layer between the air and the sapphire substrate. If a 4 nm layer with a density lower than V_2O_3 is added between the air and V_2O_3, the fitting can be optimized with the film thickness and surface roughness of V_2O_3 as 99.4 nm and 1.4 nm, respectively. This implies that the surface layer of the V_2O_3 film has a different oxygen stoichiometry.

Figure 2.10(b) shows the high angle XRD with the diffractometer aligned to the sapphire (012) and the V_2O_3 (012). When the diffractometer is aligned to the sapphire (012), no V_2O_3 diffraction peak is observed. All the diffraction peaks in this case come from the sapphire substrate. When the diffractometer is aligned to the V_2O_3 (012), diffraction peaks from V_2O_3 (012), (024) and (036) are observed at 24.32°, 49.78° and 78.36° respectively (highlighted by the red squares). The diffraction peaks on the left hand side of the highlighted peaks come from a tungsten impurity wavelength (WLα, 1.476 Å) in the X-ray. The diffraction peaks on the right hand side of the highlighted peaks come from the sapphire (012), (024) and (036). Note that the intensity of the sapphire (012) peaks close to noise level, meaning that the V_2O_3 (012) planes are not aligned to the sapphire (012) planes.

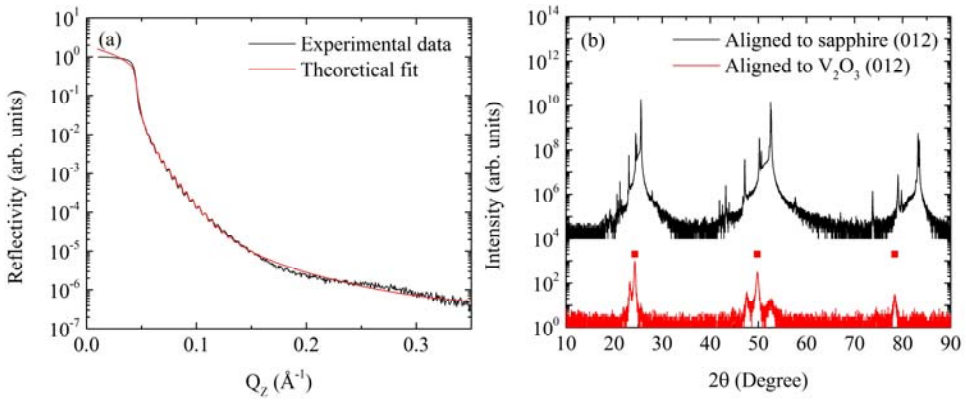

Figure 2.10. Low angle XRR of a 100 nm V_2O_3 film, experimental data (black curve) and theoretical fit (red curve). (b) High angle XRD of the same V_2O_3 film with the X-ray diffractometer aligned to the sapphire (012) (black curve) and V_2O_3 rhombohedral (012) (red curve). V_2O_3 rhombohedral (012), (024) and (036) peaks (red squares) are indicated. The curves are shifted along the y-axis for visual clarity.

II.3.2 SEM

Scanning electron microscopy (SEM) is performed in a FEI XL30-SFEG SEM to characterize the surface morphology of the vanadium oxide films. Figure 2.11 shows the SEM images of VO_2 and V_2O_3 films. The VO_2 film is constituted by grains of different sizes and irregular shapes, shown in Figure 2.11(a). The V_2O_3 film shows a different surface morphology. The grains of the V_2O_3 film elongate along a preferred direction, shown by the red dashed line in Figure 2.11(b). The V_2O_3 film also exhibits fewer grain boundaries than the VO_2 film.

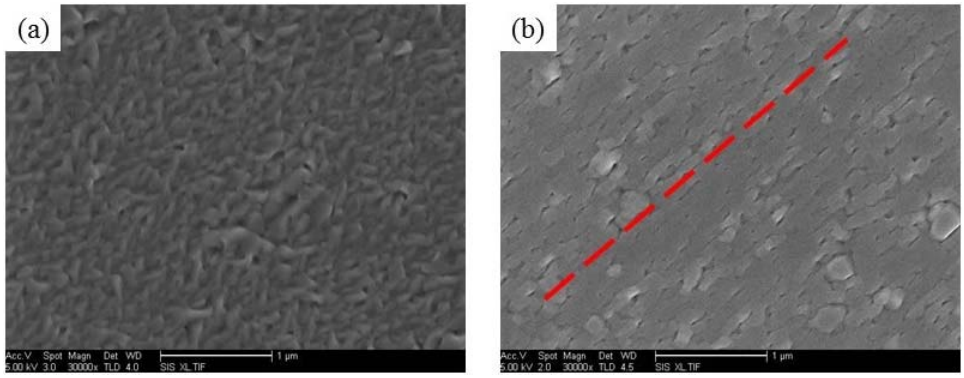

Figure 2.11. SEM images of VO_2 (a) and V_2O_3 (b). The scale bar is 1 μm. The red dashed line in (b) indicates the orientation of the V_2O_3 grains.

II.4 Fabrication of micro- and nano-sized devices

I fabricated micro- and nano-sized devices using vanadium oxide films with various lithographic techniques, including electron beam lithography, reactive ion etching (RIE) and photolithography.

II.4.1 E-beam lithography

The e-beam lithography is performed according to the following procedure, illustrated in Figure 2.12:

(1) PMMA C4 resist is spun on the vanadium oxides film for 10 s at 300 rpm and 1 min at 3000 rpm. This yields a PMMA film thickness about 400 – 450 nm, measured on a Filmetrics F20 thin film system.

(2) PMMA resist is baked at 115 °C in a vacuum tube furnace for 2 hr. The base pressure must be below 2×10^{-6} mBar to avoid surface oxidation of the vanadium oxide films. The schematic of the sample preparation is shown in Figure 2.12(a).

(3) E-beam writing is performed in a Jeol JSM-6400 Scanning Electron Microscope with a 36 KV accelerating voltage. The dose is from 450 – 600 $\mu C/cm^2$. The schematic of the sample preparation is shown in Figure 2.12(b).

(4) PMMA resist is developed in a mixture of 25 % MIBK and 75 % isopropanol for 40 s. The sample is rinsed in isopropanol for 30 s to wash away the MIBK and dried with high purity nitrogen. The schematic of the sample preparation is shown in Figure 2.12(c).

(5) A 5 min in-situ Ar sputter etching is performed with 50 W RF power and 20 mTorr Ar pressure. The purpose is to remove the surface oxidation layer and improve the contact resistance before the metal layers are deposited.

(6) 10 nm titanium and 50 nm gold layers are deposited with RF magnetron sputtering. 100 W RF power and 4 mTorr Ar pressure is applied for the titanium deposition, yielding a deposition rate of 0.91 Å/s. 50 W RF power and 4 mTorr Ar pressure is applied for the gold deposition, yielding a deposition rate of 5.25 Å/s. The schematic of the sample preparation is shown in Figure 2.12(d).

(7) The sample is rinsed in acetone for 2 hrs to soften the PMMA resist. A 10 s ultrasonication bath in acetone is performed to remove the PMMA resist and the metal layers on top. A second 10 s ultrasonication bath in acetone is performed to remove the residual PMMA resist and metals. A 10 s ultrasonication bath in isopropanol is performed

to remove the acetone. The substrate is dried with high purity nitrogen. The schematic of the final sample is shown in Figure 2.12(e).

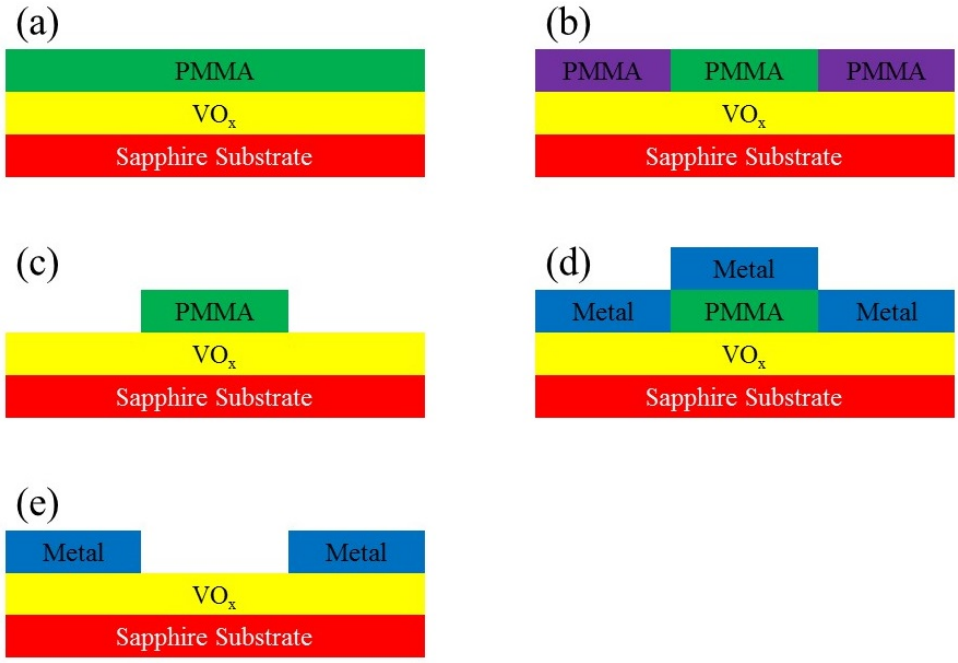

Figure 2.12. (a) PMMA (green) on VO_x film (yellow) after baking. (b) PMMA exposed by e-beam (purple) on VO_x film (yellow). (c) PMMA (green) on VO_x film (yellow) after development. (d) Metal (blue) deposited on PMMA (green) and VO_x film (yellow). (e) Metal (blue) on VO_x film (yellow) after lift-off.

II.4.2 Reactive ion etching

The reactive ion etching (RIE) is performed according to the following procedure, illustrated in Figure 2.13:

(1) S1818 resist is spun on the vanadium oxides film for 2 s at 300 rpm and 1 min at 5000 rpm. This yields a PMMA film thickness of about 2 μm, measured on a Filmetrics F20 thin film system.

(2) S1818 resist is baked at 115 °C on a hot plate for 1 min. The schematic of the sample preparation is shown in Figure 2.13(a).

(3) UV exposure is performed on a SUSS MJB 3 mask aligner. The exposure time is 3.5 min. The schematic of the sample preparation is shown in Figure 2.13(b).

(4) S1818 resist is developed in a mixture of 50 % AZ developer and 50 % DI water for 40 s. The sample is rinsed in DI water for 30 s to wash away the AZ developer and dried with high purity nitrogen. The schematic of the sample preparation is shown in Figure 2.13(c).

(5) RIE is performed in an Oxford Plasmalab 80 RIE system. The Ar flow is 10 sccm and Cl_2 flow 50 sccm. The total pressure is 50 mTorr and the RF power is 200 W, yielding an etching rate of 40 – 50 nm/min. The etching time for a 100 nm vanadium oxide film is 2.5 min. The schematic of the sample preparation is shown in Figure 2.13(d).

(6) The sample is rinsed in acetone and a 10 s ultrasonication bath is performed to remove the S1818 resist. The substrate is dried with high purity nitrogen. The schematic of the final sample is shown in Figure 2.13(e).

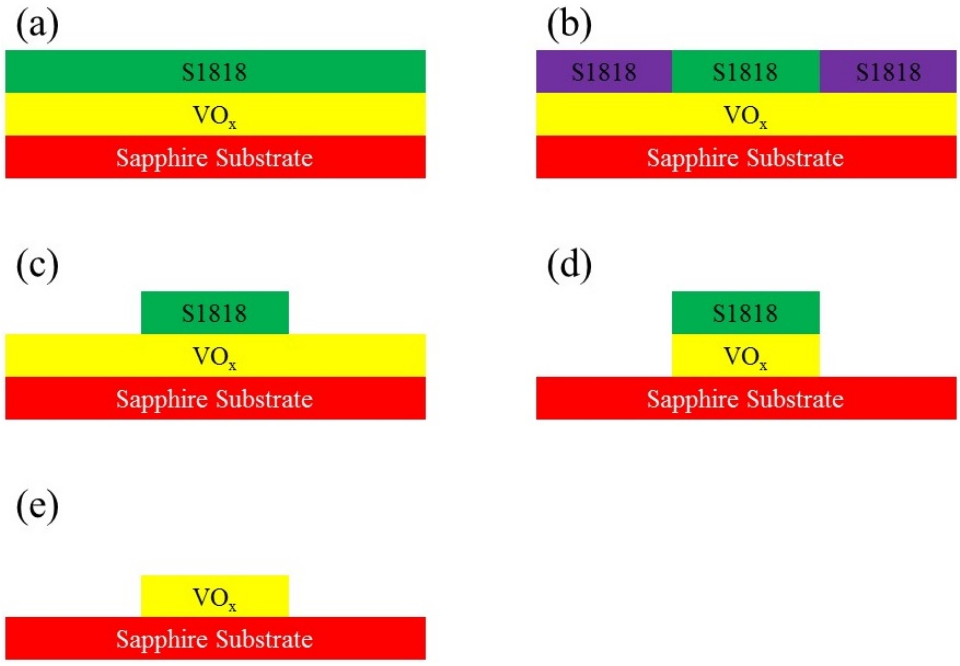

Figure 2.13. (a) S1818 (green) on VO_x film (yellow) after baking. (b) S1818 exposed by UV light (purple) on VO_x film (yellow). (c) S1818 (green) on VO_x film (yellow) after development. (d) Sample after RIE. (e) Sample after S1818 is removed.

II.4.3 Photolithography

The photolithography is performed according to the following procedure, illustrated in Figure 2.14:

(1) S1818 resist is spun on the vanadium oxides film for 2 s at 300 rpm and 1 min at 5000 rpm. This yields a PMMA film thickness about 2 μm, measured on a Filmetrics F20 thin film system.

(2) S1818 resist is baked at 115 °C on a hot plate for 1 min. The schematic of the sample preparation is shown in Figure 2.14(a).

(3) UV exposure is performed on a SUSS MJB 3 mask aligner. The exposure time is 3.5 min. The schematic of the sample preparation is shown in Figure 2.14(b).

(4) S1818 resist is developed in a mixture of 50 % AZ developer and 50 % DI water for 40 s. The sample is rinsed in DI water for 30 s to wash away the AZ developer and dried with high purity nitrogen. The schematic of the sample preparation is shown in Figure 2.14(c).

(5) A 2 min oxygen plasma etching is performed with 200 W RF power and 200 mTorr O_2 pressure. The purpose is to remove the residual S1818 resist and improve the contact resistance before the metal layers are deposited.

(6) 10 nm titanium and 100 nm gold layer are deposited with RF magnetron sputtering. 100 W RF power and 4 mTorr Ar pressure is applied for the titanium deposition, yielding a deposition rate of 0.91 Å/s. 50 W RF power and 4 mTorr Ar pressure is applied for the gold deposition, yielding a deposition rate of 5.25 Å/s. The schematic of the sample preparation is shown in Figure 2.14(d).

(7) The sample is rinsed in acetone for 1.5 hrs to soften the S1818 resist. A 10 s ultrasonication bath in acetone is performed to remove the S1818 resist and the metal layers on top. A second 10 s ultrasonication bath in acetone is performed to remove the residual S1818 resist and metals. A 10 s ultrasonication bath in isopropanol is performed to remove the acetone. The substrate is dried with high purity nitrogen. The schematic of the final sample is shown in Figure 2.14(e).

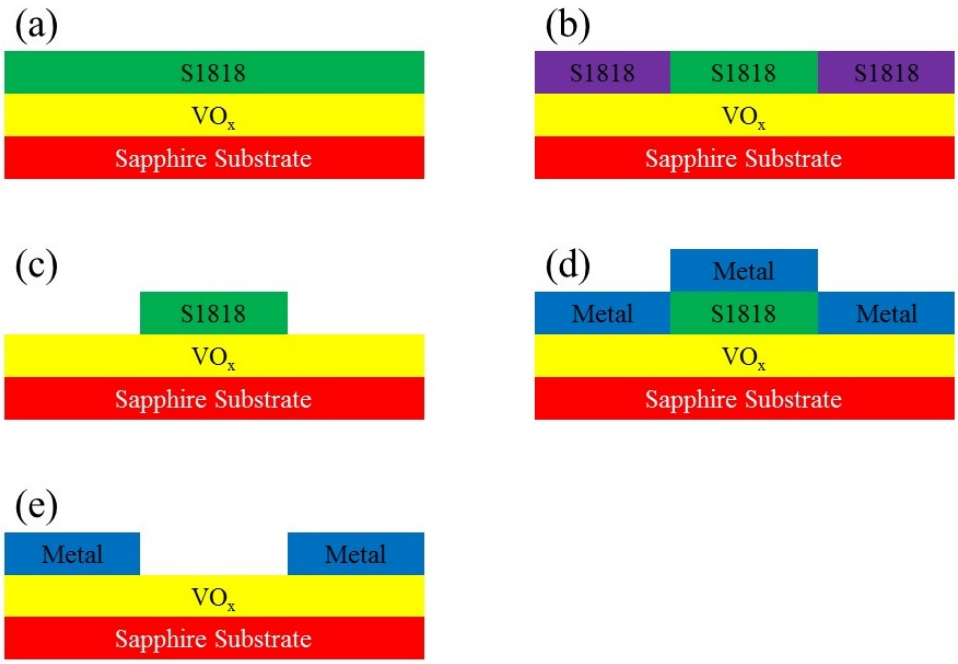

Figure 2.14. (a) S1818 (green) on VO_x film (yellow) after baking. (b) S1818 exposed by e-beam (purple) on VO_x film (yellow). (c) S1818 (green) on VO_x film (yellow) after development. (d) Metal (blue) deposited on S1818 (green) and VO_x film (yellow). (e) Metal (blue) on VO_x film (yellow) after lift-off.

Figure 2.15 shows an example of vanadium oxide nanodevices fabricated with e-beam lithography, RIE and photolithography. The bar (50 μm) is the VO_2 or V_2O_3 etched by RIE (labeled as VO_x). The e-beam patterns define the nanodevices. There are 5 e-beam patterns (nanodevices) from left to right in Figure 2.15. The gap in the middle of an e-beam pattern gives the device length and the width of the e-beam pattern gives the device width. The length is the same (500 nm) for all the devices in Figure 2.15 while the width varies from 1 – 5 μm from left to right. The photolithography patterns are electrically connected with the e-beam patterns and used to connect with cables in the electrical transport measurements.

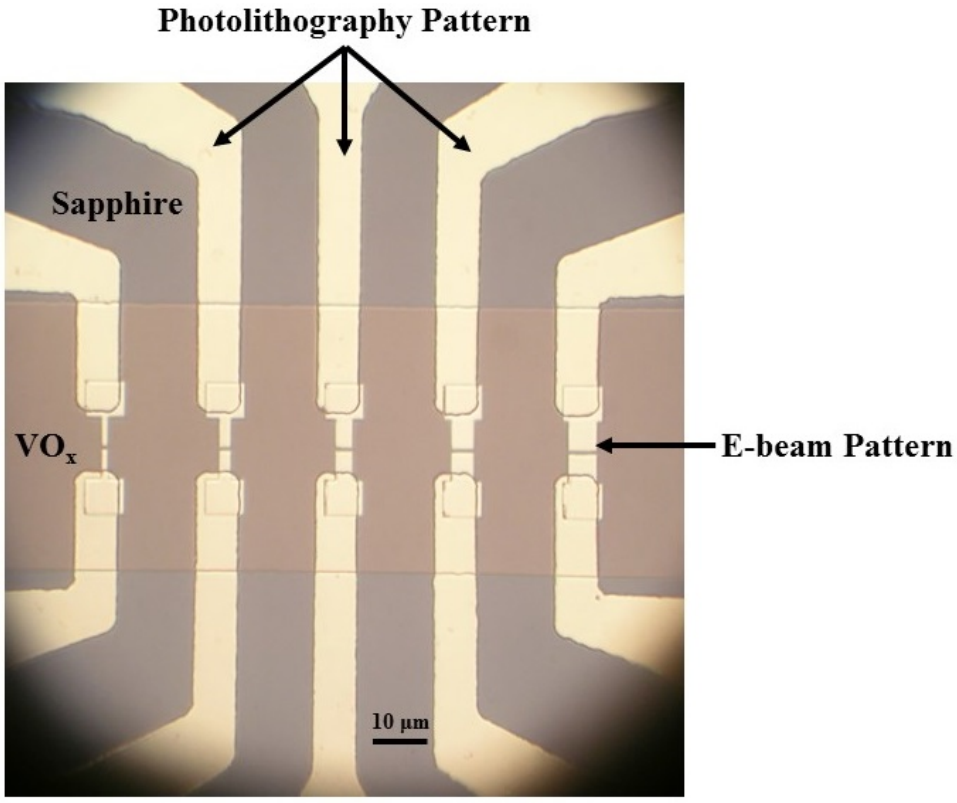

Figure 2.15. Photo image of vanadium oxide nanodevices fabricated with e-beam lithography, RIE and photolithography.

II.5 Conclusions

In this chapter, I presented the growth of vanadium oxide thin films with reactive RF magnetron sputtering and the fabrication of vanadium oxide nanodevices with various lithographic techniques. With precise controls of the gas flow and substrate temperature, I was able to grow single phase VO_2 and V_2O_3 thin films on different sapphire substrates. The crystal structure and surface morphology of the vanadium oxide thin films are characterized by XRD and SEM. Micro- and nano-sized vanadium oxide devices are

fabricated with lithographic techniques including e-beam lithography, RIE and photolithography. The recipe for each lithographic step was described in detail. With the capabilities of thin film growth and device fabrication, I was able to study the physical properties of vanadium oxides on different length scales, which will be presented in the following chapters.

II.6 References

[1] Z. Yang, C. Ko, and S. Ramanathan, Annu. Rev. Mater. Res. **41**, 337 (2011).

[2] J. Nag and R. F. Haglund Jr., J. Phys.: Condens. Matter **20**, 264016 (2008).

[3] C. H. Griffiths and H. K. Eastwood, J. Appl. Phys. **45**, 2201 (1974).

[4] C. Cesari, C. Leroux, and G. E. Nihoul, Key Eng. Mater. **155-156**, 227 (1998).

[5] S. Koide and H. Takei, J. Phys. Soc. Jpn. **22**, 946 (1967).

[6] C. B. Greenberg, Thin Solid Film **110**, 73 (1983).

[7] E. N. Fuls, D. H. Hensler, and A. R. Ross, Appl. Phys. Lett. **10**, 199 (1967).

[8] M. Borek, F. Qian, V. Nagabushnam, and R. K. Singh, Appl. Phys. Lett. **63**, 3288 (1993).

[9] K. G. West, J. Lu, J. Yu, D. Kirkwood, W. Chen, Y. Pei, J. Claassen, and S. A. Wolf, J. Vac. Sci. Technol. A **26**, 133 (2008).

[10] F. C. Case, J. Vac. Sci. Technol. A **8**, 1395 (1990).

[11] Q. Guo, D. Y. Kim, S. C. Street, and D. W. Goodman, J. Vac. Sci. Technol. A **17**, 1887 (1999).

[12] Y. Shigesato, M. Enomoto, and H. Odaka, Jpn. J. Appl. Phys. **39**, 6016 (2000).

[13] J. Lu, K. G. West, and S. A. Wolf, Appl. Phys. Lett. **93**, 262107 (2008).

[14] K. Okimura and N. Kubo, Jpn. J. Appl. Phys. **44**, L1150 (2005).

[15] G. Fu, A. Polity, N. Volbers, and B. K. Meyer, Thin Solid Films **515**, 2519 (2006).

[16] P. Jin, K. Yoshimura, and S. Tanemura, J. Vac. Sci. Technol. A **15**, 1113 (1997).

[17] J. Y. Suh, R. Lopez, L. C. Feldman, and R. F. Haglund Jr., J. Appl. Phys. **96**, 1209 (2004).

[18] B. S. Guiton, Q. Gu, A. L. Prieto, M. S. Gudiksen, and H. Park, J. Am. Chem. Soc. **127**, 498 (2005).

[19] G. Stefanovich, A. Pergament, and D. Stefanovich, J. Phys.: Condens. Matter **12**, 8837 (2000).

[20] H.-T. Kim, B.-G. Chae, D.-H. Youn, S.-L. Maeng, G. Kim, K.-Y. Kang, and Y.-S. Lim, New J. Phys. **6**, 52 (2004).

[21] B. Sass, C. Tusche, W. Felsch, N. Quaas, A. Weismann, and M. Wenderoth, J. Phys.: Condens. Matter **16**, 77 (2004).

[22] J. Brockman, N. P. Aetukuri, T. Topuria, M. G. Samant, K. P. Roche, and S. S. P. Parkin, Appl. Phys. Lett. **98**, 152105 (2011).

[23] J. Brockman, M. G. Samant, K. P. Roche, and S. S. P. Parkin, Appl. Phys. Lett. **101**, 051606 (2012).

[24] D. B. McWhan, J. P. Remeika, T. M. Rice, W. F. Brinkman, J. P. Maita, and A. Menth, Phys. Rev. Lett. **27**, 941 (1971).

[25] B. Viswanath, C. Ko, and S. Ramanathan, Scripta Mater. **64**, 490 (2011).

[26] S. Kachi, K. Kosuge, and H. Okinaka, J. Solid State Chem. **6**, 258 (1973).

[27] A. Nelson, J. Appl. Cryst. **39**, 273 (2006).

Chapter III

Avalanches in nanoscale vanadium oxides

III.1 Introduction

Real systems can be inhomogeneous for a variety of reasons [1]. Intrinsic inhomogeneities due to the latent heat in a first order phase transition can cause a coexistence of two distinct phases [2]. Extrinsic inhomogeneities, such as lattice distortions, doping, and strain, can dramatically modify the properties of materials as well [1]. Inhomogeneities can give rise to a broad range of novel phenomena in transition metal oxides in which charge, lattice and spin are strongly coupled [1]. It has been argued that inhomogeneities are related to the high temperature superconductivity in cuprates [3], the colossal magnetoresistance in manganites [4] and the multiple avalanches in vanadium dioxide (VO_2) [5]. These transition metal oxides exhibit nanoscale phase separation [3, 4] or phase coexistence [6] when the phase transitions take place.

The properties of an inhomogeneous system (crystal structure, resistance, magnetization, strain, etc.) can vary discontinuously [7] due to changes in temperature [5, 8, 9], magnetic field [10, 11], and stress [12]. The size of these changes (which we will call "events" [7]) can range over many orders of magnitude in size. The distribution of the event size follows a power law:

$$p(A) \propto A^{-\alpha}, A_{min} \leq A \leq A_{max}, \alpha > 1 \qquad (3.1)$$

where A is the event size, A_{min} and A_{max} are the minimum and maximum event size, $p(A)$ is the probability of event A and α is the power law exponent [7]. The existence of a power

law distribution indicates that the events are self-similar, i.e. there is no characteristic length (or size) of the system [13]. This phenomenon is called crackling noise or avalanches [13]. Avalanches can be observed in many natural and societal phenomena [7] such as in earthquakes, forest fires, landslides, species extinctions, epidemics, wars, stock-market crashes. Avalanches also exist in a variety of solid state systems, including Barkhausen noise in ferromagnets [10], Martensitic transformations [8], vortex motion in type-II superconductors [14], and helium condensation in porous materials [9]. Recently, multiple avalanches were observed in the resistance versus temperature (R-T) characteristics of VO_2 nanodevices [5]. The sizes of the temperature driven resistance jumps range over 2 – 3 orders of magnitude and the distribution of the sizes follows a power law. The power law exponent was found to be independent of device geometry or temperature sweep rate, indicating that the exponent is related to the intrinsic properties of VO_2 and the inhomogeneities in VO_2 or in the driving force. A theoretical model has been proposed to explain the avalanches in VO_2 with a voltage induced breakdown [15]. Avalanches in VO_2 occur through random percolation with low applied voltages and through filament formation with high applied voltages.

Avalanches can be expected in V_2O_3 for the following reasons: i) it has a first order metal insulator transition (MIT) with a similar phenomenology as the MIT that occurs in VO_2 [16]; ii) phase coexistence has been observed in V_2O_3 with low temperature scanning electron microscopy [17]. In this chapter, I will present evidence of avalanches in the R-T characteristics of V_2O_3 nanodevices. I measured the R-T characteristics of V_2O_3 nanodevices with device lengths from 500 nm to 2 μm and device widths from 1 μm to 5 μm. Resistance jumps over 3 – 4 orders of magnitude are observed in all of the devices.

The largest jumps depend on the device dimensions. The resistance jumps follow a power law distribution with a power law exponent independent of the device geometry. Furthermore, avalanches of V_2O_3 and VO_2 are compared with a numerical model based on 2D random percolation. The differences in the power law exponents suggest that the MITs in V_2O_3 and VO_2 may occur through different mechanisms.

III.2 Avalanches in V_2O_3 nanodevices

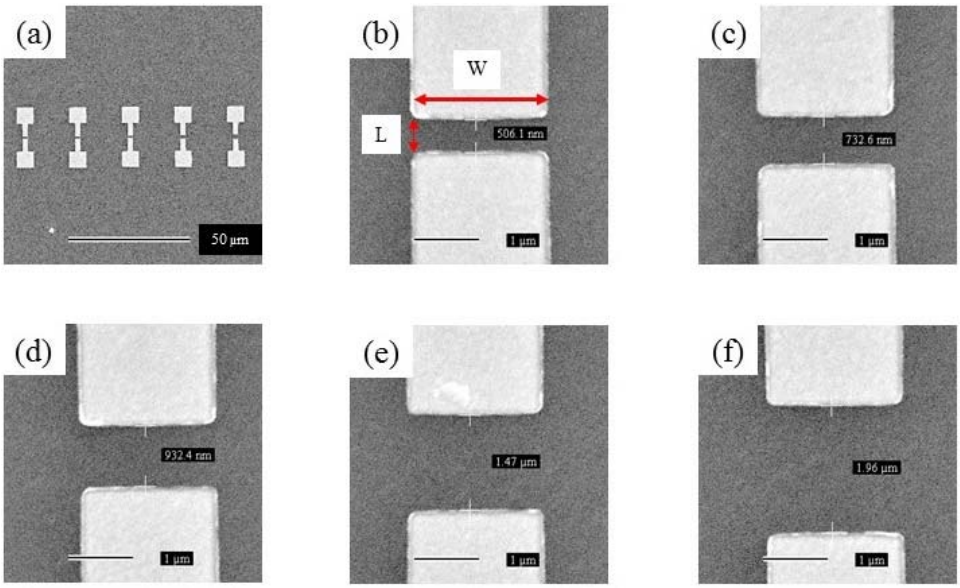

Figure 3.1. (a) SEM images of 5 V_2O_3 nanodevices with different lengths fabricated by e-beam lithography. The scale bar is 50 µm. The dark color in the images comes from the V_2O_3 and the light color comes from the gold. (b-f) Zoomed SEM images of the devices in (a) from left to right. The scale bar is 1 µm. The device length (L) is also labeled in the images: (b) 506 nm, (c) 733 nm, (d) 932 nm, (e) 1.47 µm and (f) 1.96 µm. The device width (W) is 2 µm for all the devices.

V_2O_3 nanodevices of different sizes are fabricated with the lithographic techniques described in Chapter II. Figure 3.1 shows the SEM images of a set of devices with increasing lengths but identical widths, fabricated on the same V_2O_3 thin film.

R-T characteristics of V_2O_3 nanodevices are measured in a cryostat cooled by a helium close cycle refrigerator (CCR). The base pressure of the cryostat is 1×10^{-6} Torr. The substrate is mounted on a copper cold finger with Ted Pella 3M 1182 double-sided copper tape. The adhesive on the copper tape is an electrically conductive and pressure sensitive acrylic adhesive. The temperature is measured with a calibrated cernox temperature sensor and controlled with a Lakeshore 325 temperature controller. The temperature sweep rate is kept constant during the measurements. The resistance of the devices is measured in a 2-probe configuration with a Keithley 6220 precision current source and a Keithley 2182A nanovoltmeter. The DC current used in all measurements is 100 nA. This current is within the linear region of the current-voltage (I-V) characteristics of the V_2O_3 nanodevices, so the Joule heating induced by the current is low and does not increase the local temperature of the nanodevices.

Figure 3.2 shows the heating branches (indicated by the red arrow in the inset of Figure 3.2) of 5 consecutive R-T measurements of a 1×2 μm^2 V_2O_3 device. The temperature sweep rate during the measurements is 1 K/min. The device exhibits a 5 orders of magnitude MIT over 20 K with a 5 K thermal hysteresis centered at 150 K as shown in the inset of Figure 3.2. The properties of this MIT are similar to those of the MIT in a V_2O_3 thin film. Resistance jumps of various sizes are observed from the onset of the MIT, as shown in Figure 3.2. The jumps are found between two adjacent data points with a

temperature difference of 2.5 mK. There are a few large jumps of up to 2×10^4 Ω, which account for more than 50 % of the resistance change. The rest of the jumps are smaller, ranging from a few kiloohms to a few ohms, limited by the system resolution. This indicates that the MIT in V_2O_3 is inhomogeneous at the nanoscale, due to the coexistence of the insulating and metallic phases. The MIT occurs through a series of discontinuous events over a broad range of magnitudes. To further understand the properties of the MIT in V_2O_3, statistics of the distribution of the resistance jump sizes must be studied.

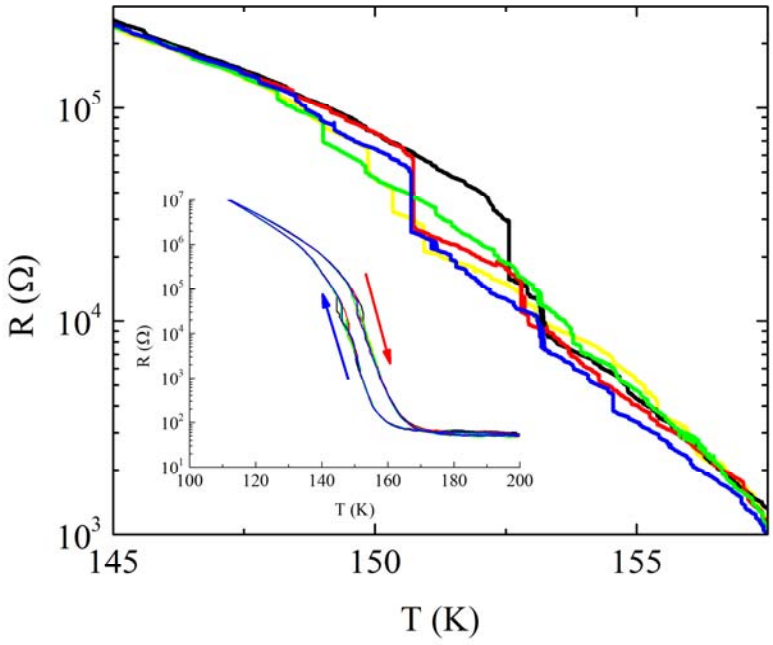

Figure 3.2. The heating branches of 5 consecutive R-T measurements of a 1×2 μm^2 V_2O_3 device. The 5 R-T measurements are shown by 5 different colors. The main figure shows between 145 and 157.5 K, a range that contains the largest jumps. The full hysteresis loop is shown in the inset. The red arrow indicates the heating branches and the blue arrow indicates the cooling branches.

Figure 3.3 shows the temperature distribution of the resistance jump sizes $\frac{\Delta R}{R}$ for the 1×2 μm^2 V_2O_3 device from 10 consecutive R-T measurements. The jump size $\frac{\Delta R}{R}$ is calculated with two consecutive data points (T_1,R_1) and (T_2,R_2) from the R-T characteristics. For the heating branches ($T_1 < T_2$) of the R-T measurements,

$$\frac{\Delta R}{R} = \frac{R_1 - R_2}{R_1}; \tag{3.2a}$$

for the cooling branches ($T_1 > T_2$) of the R-T characteristics,

$$\frac{\Delta R}{R} = \frac{R_2 - R_1}{R_2}. \tag{3.2b}$$

Resistance jumps ranging over two orders of magnitude exist from 120 – 175 K. In Figure 3.3, most of the jumps take place between 140K and 160 K. The largest jumps are located around 150 K (red circles) and 145 K (blue circles), which are the centers of the heating and cooling branches, respectively. In the next section, these resistance jumps will be analyzed with the maximum likelihood method, to show a power law distribution.

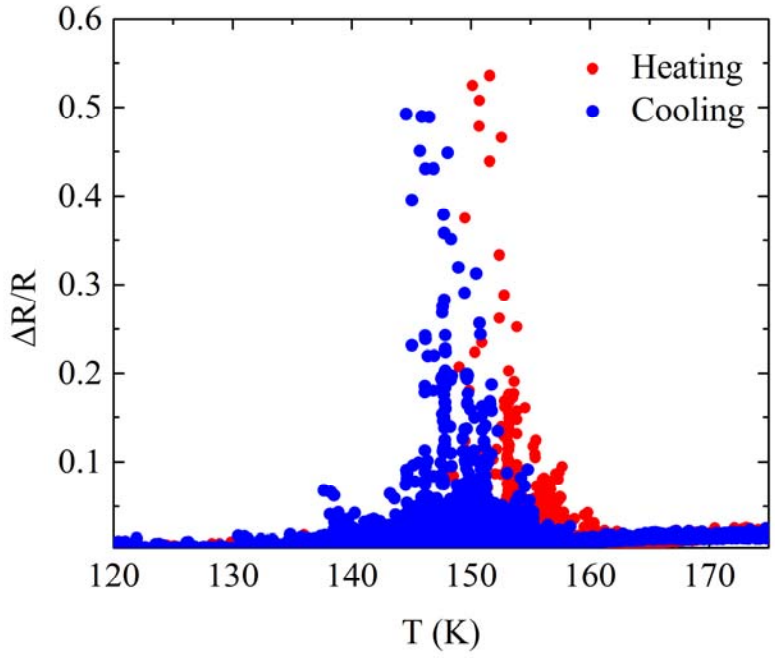

Figure 3.3. Temperature distribution of resistance jumps of the 1 × 2 μm^2 V_2O_3 device from 10 consecutive R-T measurements. Red circles are jumps from the heating branches of the R-T characteristics and blue circles are from the cooling branches.

III.2.1 Power law distribution and maximum likelihood method

In this section, I will describe the maximum likelihood method (MLM) from Ref. 18, which will be used to fit the power law distribution. For a data set following a power law distribution, a probability density function can be defined by Equation (3.3):

$$p\left(x = \frac{\Delta R}{R}\right) = C\left(\frac{\Delta R}{R}\right)^{-\alpha}, \tag{3.3}$$

where $x = \frac{\Delta R}{R}$ are the resistance jumps in Figure 3.3, $p\left(x = \frac{\Delta R}{R}\right)$ is the probability density, α is the power law exponent and C is the normalization constant. The probability for a jump of $x = \frac{\Delta R}{R}$ is

$$P\left(x \le \frac{\Delta R}{R} < x + dx\right) = C\left(\frac{\Delta R}{R}\right)^{-\alpha} dx. \tag{3.4}$$

Considering that

$$\int_{x_{min}}^{x_{max}} C(x)^{-\alpha}\, dx \approx \int_{x_{min}}^{+\infty} C(x)^{-\alpha}\, dx = 1, \tag{3.5}$$

where x_{min} and x_{max} are the minimum jump size, and $x_{max} >> x_{min}$, we have

$$p(x) = \frac{\alpha-1}{x_{min}}\left(\frac{x}{x_{min}}\right)^{-\alpha}, \alpha > 1. \tag{3.6}$$

We estimate the power law exponent α with the maximum likelihood method [18]. For a data set $\left\{x_i = \frac{\Delta R}{R}\right\}$, the probability for this data set is proportional to

$$\prod_{i=1}^{n} p(x_i) = \prod_{i=1}^{n} \frac{\alpha-1}{x_{min}}\left(\frac{x_i}{x_{min}}\right)^{-\alpha}, \tag{3.7}$$

where n is the total number of the data points. We define the likelihood of the data as

$$L = \ln \prod_{i=1}^{n} p(x_i) = \ln \prod_{i=1}^{n} \frac{\alpha-1}{x_{min}}\left(\frac{x_i}{x_{min}}\right)^{-\alpha} = n\ln(\alpha-1) - n\ln x_{min} - \alpha \sum_{i=1}^{n} \ln \frac{x_i}{x_{min}}. \tag{3.8}$$

The power law exponent α, which gives the maximum likelihood, is determined by

$$\frac{\partial L}{\partial \alpha} = \frac{n}{\alpha-1} - \sum_{i=1}^{n} \ln \frac{x_i}{x_{min}} = 0. \tag{3.9}$$

The estimated power law exponent α is

$$\alpha = 1 + n\left[\sum_{i=1}^{n} \ln\frac{x_i}{x_{min}}\right]^{-1}. \quad (3.10)$$

The standard deviation of α is given by [18]

$$\sigma = \frac{\alpha}{\sqrt{n}}. \quad (3.11)$$

With the probability density function (Equation 3.6), the cumulative distribution function can be defined as

$$P_{MLM}(x \geq x_i) = \int_{x_i}^{\infty} p(x)dx = \left(\frac{x_i}{x_{min}}\right)^{-\alpha+1}. \quad (3.12)$$

The cumulative distribution function $P_{MLE}(x \geq x_i)$ gives the probability for the data points greater than x_i. Experimentally, the cumulative distribution function can be estimated by sorting the data set from low to high,

$$P_{Exp}(x \geq x_i) = 1 - \frac{r_i - 1}{n}, \quad (3.13)$$

where r_i is the ranking of data point x_i after sorting by size. The power law exponent estimated by Equation (3.10) depends on the minimum jump size x_{min}. The best estimation of the power law exponent is made when the x_{min} that minimizes

$$D = \max_{x_i \geq x_{min}} \left|P_{MLM}(x \geq x_i) - P_{Exp}(x \geq x_i)\right|, \quad (3.14)$$

where D is the maximum difference between $P_{MLM}(x \geq x_i)$ and $P_{MLM}(x \geq x_i)$.

Figure 3.4 shows the cumulative distribution function (Equation 3.13) calculated from the heating branches of the 1 × 2 μm^2 V_2O_3 device (red circles in Figure 3.3) and the

maximum likelihood method (Equation 3.10). The probability of the jumps and jump sizes follow a power law dependence. The maximum likelihood fitting is obtained with $\left(\frac{\Delta R}{R}\right)_{min}$ = 0.0028. The power law exponent is α = 2.22 ± 0.03. The best fitting of the power law distribution is between $\frac{\Delta R}{R}$ = 0.0028 and $\frac{\Delta R}{R}$ = 0.06. For $\frac{\Delta R}{R}$ < 0.0028, the number of the jumps is over counted because of the noise in the measurement system, giving an exponent higher than the real value. The probability for the jump sizes $\frac{\Delta R}{R}$ > 0.06 is very low (~ 1%). A limited number of R-T measurements cannot offer a good resolution in the region. This gives rise to the deviation of the experimental data from the fitting as shown in Figure 3.4. The power law dependence implies that the MIT of V_2O_3 occurs through avalanches. To further understand the avalanches in nanoscale V_2O_3, V_2O_3 devices with different dimensions need to be studied.

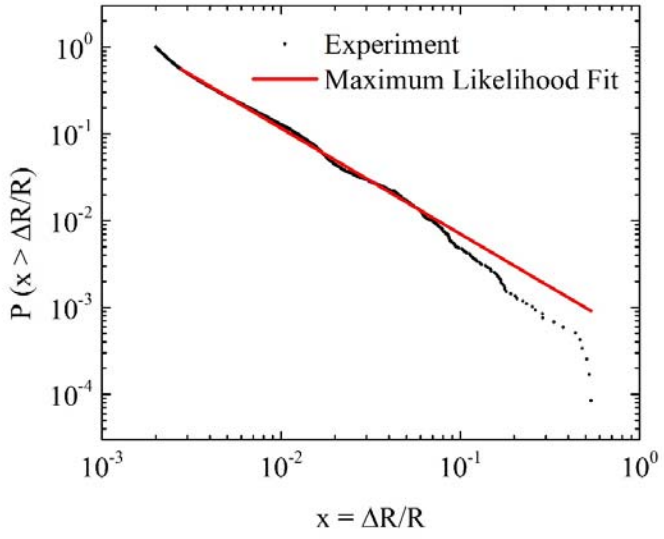

Figure 3.4. (Black circles) Cumulative distribution function of the resistance jumps from the heating branches of 10 R-T measurements from the 1 × 2 μm^2 V_2O_3 device. (Red line) Cumulative distribution function calculated with maximum likelihood method.

III.2.2 Geometrical effect – maximum jump size

In the following two sections, I will discuss the geometrical and non-geometrical effects of the R-T characteristics of V_2O_3 devices with different dimensions. In this section, I will focus on the geometrical dependence of the maximum jump size in the R-T characteristics. Figure 3.5 shows the maximum jump size as a function of the device length. All the devices are fabricated on one 100 nm V_2O_3 thin film and the device width is kept constant (2 μm) for all the devices. Each data point in Figure 3.5 is calculated by averaging the maximum jumps from the heating (or cooling) branches of 10 consecutive R-T measurements for each device length and the error bar is the standard deviation. For both heating (Figure 3.5(a)) and cooling (Figure 3.5(b)), the average maximum jump size decreases with the increasing device length. For each device length, the maximum jump size is the same within the error bar for heating and cooling.

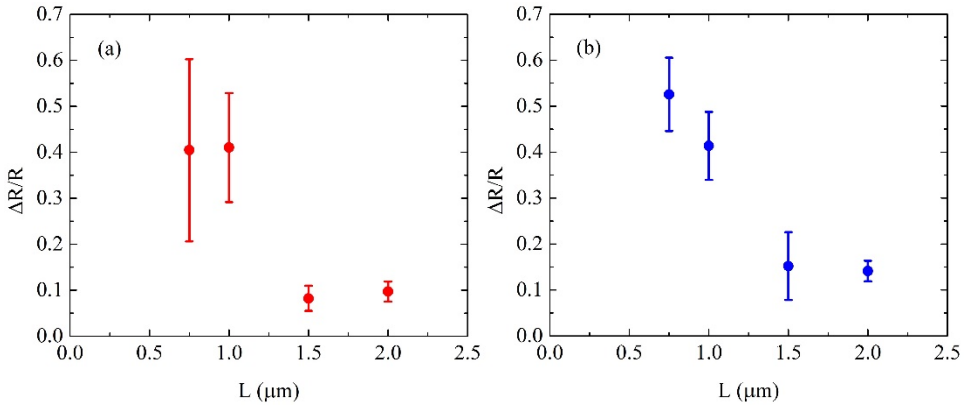

Figure 3.5. The average value of the maximum jumps versus the device length. (a) The red circles are the maximum jumps from the heating branches of 10 consecutive R-T measurements for each device length and (b) the blue circles are maximum jumps from the cooling branches of the same R-T measurements. The error bars are standard deviations.

Figure 3.6 shows the maximum jump size as a function of the device width. All the devices are fabricated on one 100 nm V_2O_3 thin film and the device length is constant (500 nm) for all the devices. Note that the two V_2O_3 films used to produce Figure 3.5 and 3.6 are deposited separately. The data points and error bars in Figure 3.6 are obtained with the same method as for Figure 3.5. For both heating (Figure 3.6(a)) and cooling (Figure 3.6(b)), the average maximum jump size decreases with the increasing device length except for one data point at 3 μm. A difference from the sample in Figure 3.5 is that the maximum jumps in the heating are higher than those in the cooling, except for the 5 μm device.

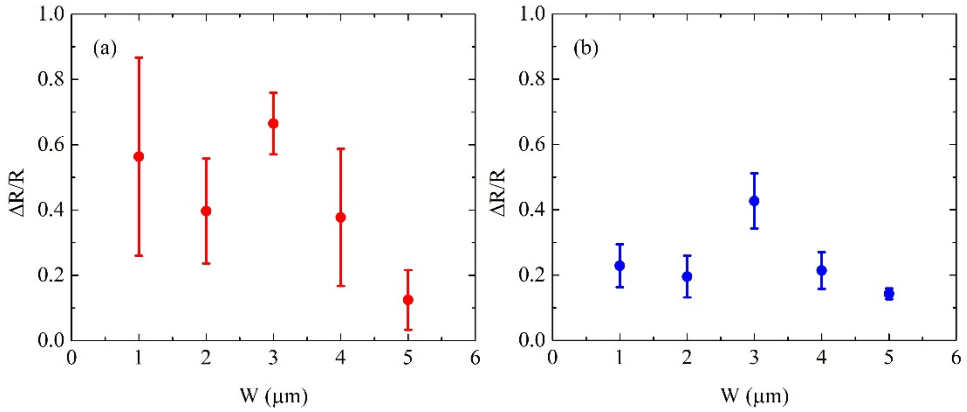

Figure 3.6. The average value of the maximum jumps versus the device width. (a) The red circles are the maximum jumps from the heating branches of 10 consecutive R-T measurements for each device width and (b) the blue circles are maximum jumps from the cooling branches of the same R-T measurements. The error bars are standard deviations.

From Figure 3.5 and 3.6, we can summarize the behavior of the maximum jump size as follows.

(1) The maximum jump size decreases with the increasing device size. This implies that the device size is on the same length scale as the domains involved in the MIT of V_2O_3. As the device size increases, a domain switching contributes less to the resistance change of the device, leading to a decrease of the maximum jump size. The maximum jump size depends on the device geometry.

(2) For a device, the maximum jump size can be the same or different for the heating and cooling branches of the R-T characteristics. This was different for samples from different depositions. For the sample in Figure 3.5, the maximum jump size in heating and cooling are equal within the error bars; for the sample in Figure 3.6, the maximum jump size in heating and cooling are different. The maximum jump size shows a sample dependence.

(3) The 3 μm device in Figure 3.6 shows a larger average maximum jump size than other devices on the same film. This may be attributed to local defects in this device. The contact between V_2O_3 and the gold electrodes could be inhomogeneous, leading to a reduced device width. Both effects could cause an increase in the maximum jump size. The maximum jump size depends on the defects.

The jumps of the V_2O_3 devices indicate the percolation [19, 20] of the V_2O_3 domains, which connects the two electrodes of the devices. This geometrical effect is strongly related to the device size and the defects, both of which are extrinsic properties of the V_2O_3 devices. Similar behavior was observed in VO_2 devices with the same dimensions [5].

III.2.3 Non-geometrical effect – power law exponent

In this section, I will focus on the geometrical dependence of the power law exponent obtained from the maximum likelihood method (Equation 3.10). Figure 3.7 shows the geometrical dependence of the power law exponent with the device length (Figure 3.7(a)) and width (Figure 3.7(b)). The value of the exponent is 2.1 – 2.7 for all the devices and does not depend on the samples. The exponent does not scale with the device length or width as the maximum jump size does. It also does not change if the temperature sweep rate is changed from 1 K/min to 0.5 K/min. For both samples in Figure 3.7, the value of the exponent from the heating is always higher than that from the cooling. This indicates that the power law exponent of the V_2O_3 device is related to the non-geometrical, intrinsic properties and inhomogeneities of V_2O_3.

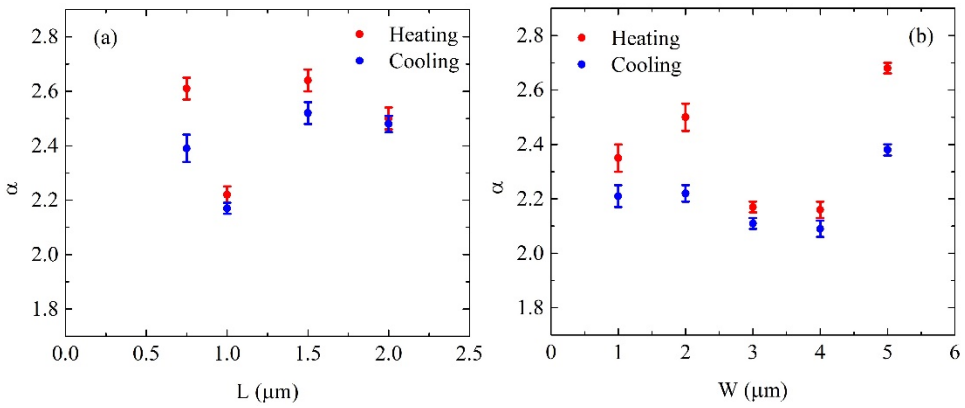

Figure 3.7. Geometrical dependence of the power law exponent from the maximum likelihood method (Equation 3.10): dependence on (a) device length and (b) device width. The red circles are the exponents from the heating branches of 10 consecutive R-T measurements for each device width and the blue circles are the exponents from the cooling branches of the same R-T measurements. The error bars are standard deviations given by Equation (3.11).

III.3 Comparing avalanches in VO_2 and V_2O_3

The power law exponent is also an intrinsic parameter for VO_2 [5]. Figure 3.8 compares the power law exponents of VO_2 and V_2O_3 devices with device length between 500 nm to 2 μm. There are two distinct differences between the two materials.

(1) The value of the exponent is 1.9 – 2.4 for all the VO_2 devices, which is lower than the exponent for the V_2O_3 devices.

(2) For VO_2, the value of the exponent does not depend on whether the device is heating or cooling, whereas in V_2O_3, it does.

These two differences imply that the MITs of VO_2 and V_2O_3 occur through different mechanisms.

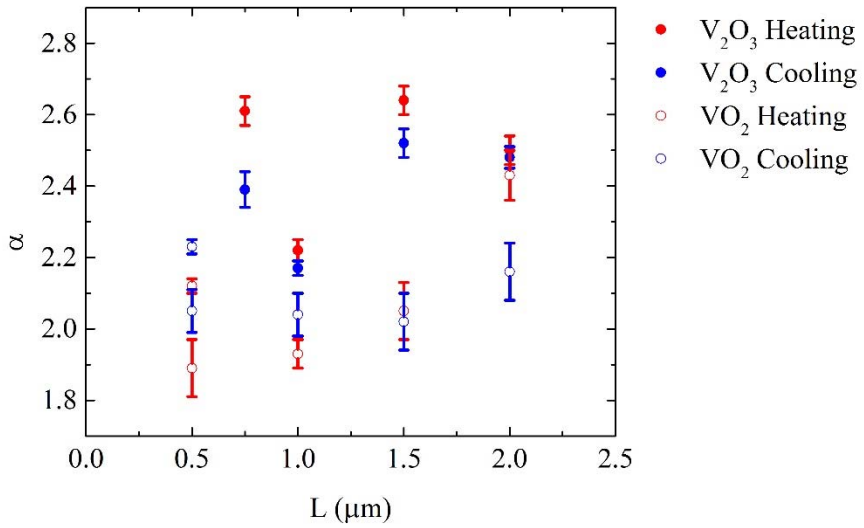

Figure 3.8. Power law exponents of V_2O_3 (solid circles) and VO_2 (open circles) devices with different lengths. The red circles are the exponents from the heating branches of the R-T measurements and the blue circles from the cooling branches of the same R-T measurements. The error bars are standard deviations given by Equation (3.11).

III.4 Theoretical model

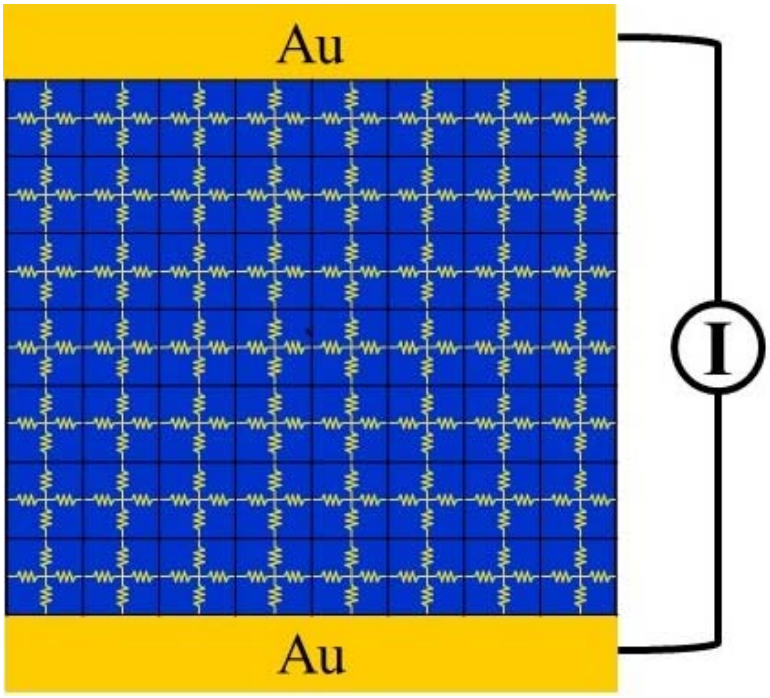

Figure 3.9. Schematic of a 2D resistor network in a square lattice. Each square with 4 resistors represents a 50 × 50 nm^2 V_2O_3 domain which switches independently from its neighbors. When a domain switches, the resistance of the resistor changes from 1.2 MΩ (insulating phase) to 120 Ω (metallic phase). The current flows in and out of the network through two gold electrodes with zero resistance.

I performed a numerical simulation with a random percolation model to understand the physical mechanism in the avalanches of vanadium oxides. The V_2O_3 device is simulated with a 2D square lattice as shown in Figure 3.10 [5]. Each lattice site represents a 50 × 50 nm^2 V_2O_3 domain. I assumed that the MIT in a 50 × 50 nm^2 V_2O_3 domain takes place independently from its neighbors. The transition temperature of the domains follows a Gaussian distribution with a mean value 150 K and a standard deviation of 10 K. Each

domain contains 4 resistors as shown in Figure 3.9. When a domain switches, the resistance of the resistor changes from 1.2 MΩ (insulating phase) to 120 Ω (metallic phase). The current flows in and out of the network through two gold electrodes with zero resistance. For each temperature, the resistance of the network can be calculated by solving the Kirchhoff equations for all the domains.

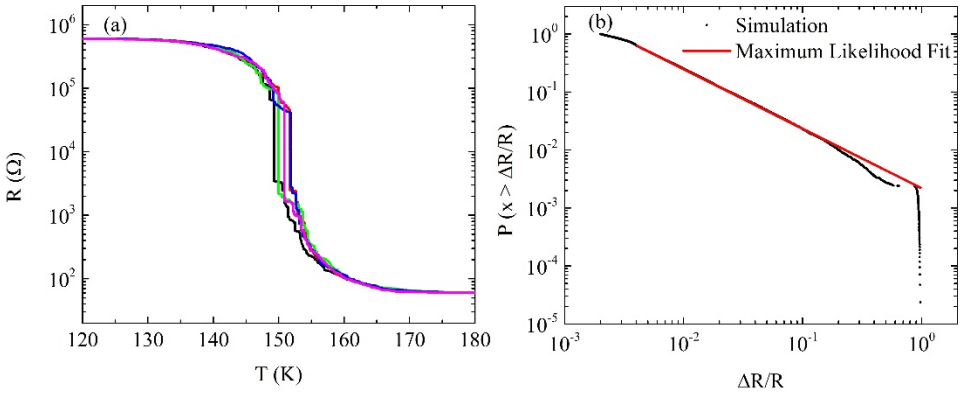

Figure 3.10. (a) 5 simulated R-T characteristic curves (heating branches) of a 1 × 2 μm^2 V_2O_3 device with the random percolation model. (b) The black circles are the cumulative distribution function from 100 simulated R-T characteristic curves and the red line is the maximum likelihood fitting.

Figure 3.10(a) shows 5 simulated R-T characteristic curves of a 1 × 2 μm^2 V_2O_3 device. Each R-T curve is calculated with a different random distribution of the transition temperatures in the network. This reproduces that the resistance jumps occur at different temperatures in different R-T measurements. A large resistance jumps exist at 5 different temperatures close to the mean transition temperature, 150 K, for all the 5 simulated R-T curves. This is the temperature at which the percolation occurs in the network. The jump size ΔR/R at this temperature is up to 0.94, higher than the measured value shown in Figure

3.5. This implies that the domain size (50 × 50 nm^2) in the simulation is larger than the domains in the V_2O_3 device. Figure 3.10(b) shows the cumulative distribution function for 100 simulated R-T curves (black circles) and the fitting with the maximum likelihood method (red line). The power law exponent α is 2.03 ± 0.01 and the minimum jump size x_{min} is 0.004. The probability below x_{min} is lower than the value expected from the maximum likelihood fitting. This also indicates that the domain size (50 × 50 nm^2) in the simulation is larger than the domains in the V_2O_3 device. The number of jumps below x_{min} in the simulation is underestimated due to the lack of domains smaller than 50 × 50 nm^2. It is beyond our computational capacity to further reduce the domain size.

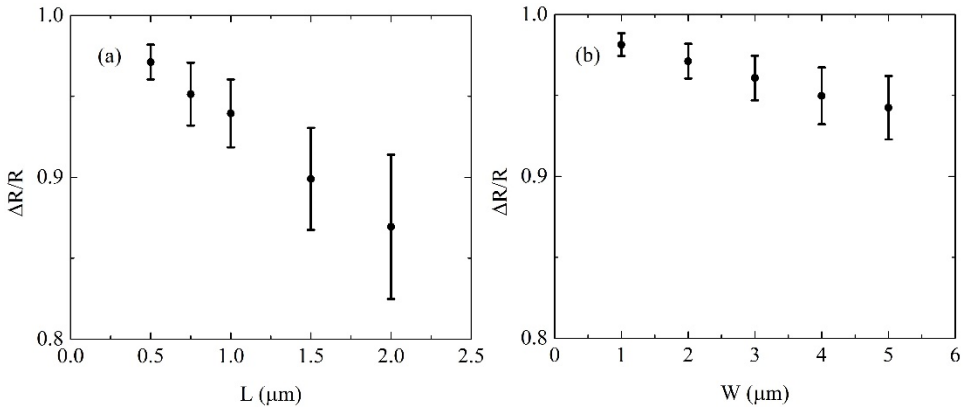

Figure 3.11. Average maximum jump size of 100 simulated R-T characteristic curves versus (a) device length and (b) width. The error bars are standard deviations.

Figure 3.11 shows the simulated geometrical dependence of the maximum jump size ΔR/R. Figure 3.11(a) shows maximum jump size for device lengths from 500 nm to 2 μm. The device width is 2 μm. These dimensions are the same as the device shown in

Figure 3.5. Figure 3.11(b) shows device widths from 1 μm to 5 μm. The device length is 500 nm. These dimensions are the same as the device shown in Figure 3.6. The maximum jump size decreases with the increasing device length and width. This supports the argument that the maximum jump size is determined by the extrinsic properties, such as device geometry.

Figure 3.12 shows the geometrical dependence of the power law exponent α from the same simulation as the one shown in Figure 3.11. The power law exponents for different device dimensions are all close to 2.05 and this value is the same for heating and cooling. This supports the claim that the power law exponent is related to the intrinsic properties of the system. For a random percolation model in a 2D square lattice, the power law exponent is 2.05.

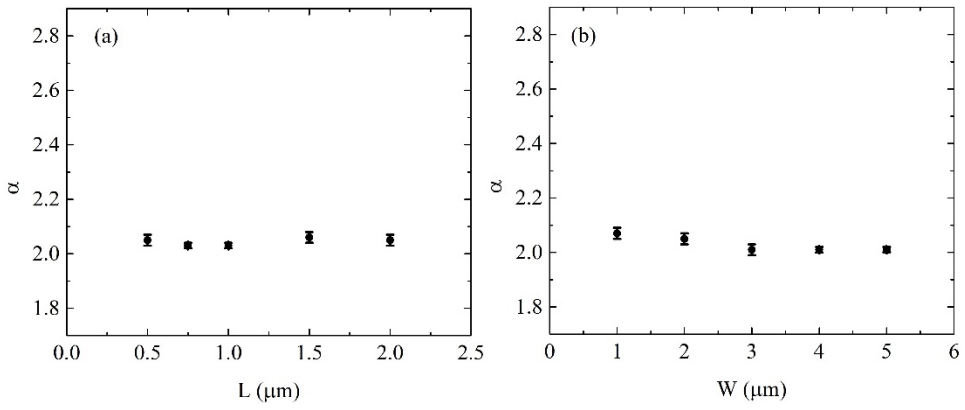

Figure 3.12. Power law exponent of 100 simulated R-T characteristic curves versus (a) device length and (b) width. The error bars are standard deviations given by Equation (3.11).

Figure 3.13 compares the power law exponent of V_2O_3, VO_2 and the simulation. The power law exponent for VO_2 is close to the simulated value and shows no dependence on the heating and cooling. This implies that a 2D random percolation model describes the MIT in the VO_2 devices [15]. However, the power law exponent for V_2O_3 is higher than the simulated value and depends on heating and cooling. This means that a 2D random percolation model is not sufficient to describe the MIT in the V_2O_3 devices.

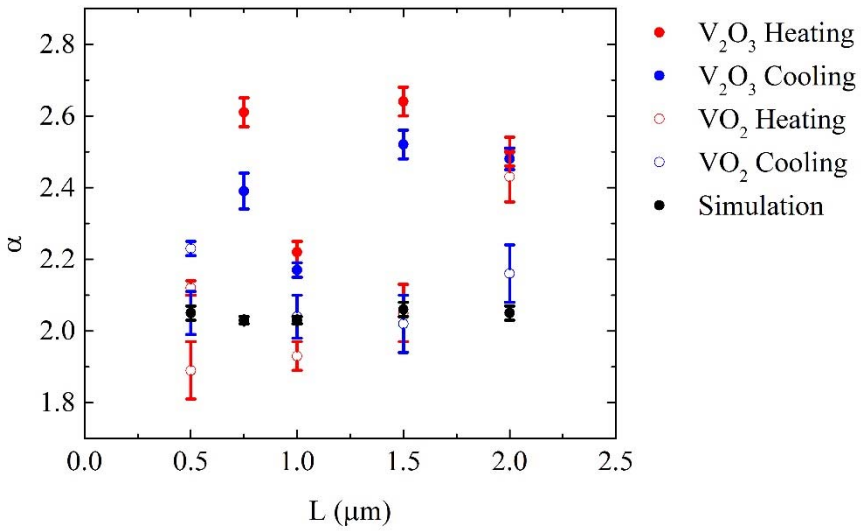

Figure 3.13. Comparison of the power law exponent of V_2O_3 (solid circles), VO_2 (open circles) and the simulation (black circles). The red circles are the exponents from the heating branches of the R-T measurements and the blue circles are the exponents from the cooling branches of the same R-T measurements. The error bars are the standard deviations given by Equation (3.11).

Asymmetry has been observed in first order phase transitions such as in water [21], elemental metals [22], type-II superconductors [23, 24], $CeFe_2$ [25, 26], $CuMoO_4$ [27], and $NdNiO_3$ [28]. Recently, asymmetric R-T characteristics of single crystalline VO_2

microbeams were reported [29]. The heating branch contains multiple small resistance jumps (10 – 100 Ω) while the cooling branch shows several large jumps of up to 10^5 Ω. Monoclinic twin walls exist at the low temperature end of the transition and act as nucleation centers leading to a continuous MIT for the heating. No twinning walls exist at the high temperature end of the transition, due to the high symmetry of the rutile phase. This causes supercooling (VO_2 remains in the high temperature phase at temperatures below the transition temperature) and a discontinuous MIT during the cooling. The supercooling can be suppressed by point defects, which act as nucleation centers at high temperature. This leads to a symmetric R-T characteristic.

The V_2O_3 films studied in this chapter are single crystalline and more homogeneous than the VO_2 films shown by the SEM images in Section II.3.2 of Chapter II. Monoclinic twin walls at the low temperature can increase the number of nucleation centers and the probability of the small resistance jumps during the heating. This causes a higher power law exponent and an asymmetric MIT in V_2O_3. To further support this hypothesis, point defects can be induced by doping or ion irradiation to suppress the supercooling during the cooling and increase the value of the power law exponent, but that is beyond the scope of this thesis.

III.5 Conclusions

To summarize, in this chapter, I presented the study of the R-T characteristics of V_2O_3 nanodevices. Multiple jumps in the resistance were observed in the R-T characteristics of V_2O_3 devices with sizes ranging from 500 nm to 5 μm. The maximum

jump sizes in the R-T characteristics increase with decreasing device dimensions, indicating that the maximum jumps are determined by the geometrical effects. A power law distribution is found for the resistance jumps $\frac{\Delta R}{R} = 10^{-3}$ to $\frac{\Delta R}{R} = 10^{-1}$. The power law exponent does not show a geometrical dependence and the value from heating is always higher than from cooling. This implies that the power law exponent is related to the intrinsic properties and inhomogeneities of V_2O_3.

The power law exponent of V_2O_3 was compared to VO_2 and a 2D random percolation model. While the MIT of the VO_2 devices can be described by the 2D random percolation model, the MIT of the V_2O_3 devices shows different characteristics. This indicates that the MITs of VO_2 and V_2O_3 occur through different mechanisms. The asymmetry in the MIT of V_2O_3 may be attributed to the supercooling during the cooling while superheating is suppressed during the heating due to the twin walls of the low symmetry monoclinic phase.

III.6 Acknowledgements

Chapter III in part is currently being prepared for submission for publication of the material. The co-authors are J. G. Ramirez, and I. K. Schuller. The dissertation author was the primary investigator and author of this material.

III. 7 References

[1] E. Dagotto, Scinece **309**, 257 (2005).

[2] P. Papon, J. Leblond, and P. H. E. Meijer, translated by S. L. Schnur, *The Physics of Phase Transitions*, 2nd edition (Springer, New York, 2006).

[3] K. M. Lang, V. Madhavan, J. E. Hoffmann, E. W. Hudsen, H. Eisaki, S. Uchida, and J. C. Davis, Nature **415**, 412 (2002).

[4] M. Fath, S. Freisem, A. A. Menovsky, Y. Tomioka, J. Aarts, and J. A. Mydosh, Science **285**, 1540 (1999).

[5] A. Sharoni, J. G. Ramírez, and I. K. Schuller, Phys. Rev. Lett. **101**, (2008).

[6] M. M. Qazilbash, M. Brehm, B.-G. Chae, P.-C. Ho, G. O. Andreev, B.-J. Kim, S. J. Yun, A. V. Balatsky, M. B. Maple, F. Keilmann, H.-T. Kim, and D. N. Basov, Science **318**, 1750 (2007).

[7] D. L. Turcotte, Rep. Prog. Phys. **62**, 1377 (1999).

[8] E. Vives, J. Ortin, L. Manosa, I. Rafols, R. Perez-Magrane, and A. Planes, Phys. Rev. Lett. **72**, 1694 (1994).

[9] M. P. Lilly, P. T. Finley, and R. B. Hallock, Phys. Rev. Lett. **71**, 4186 (1993).

[10] P. J. Cote and L. V. Meisel, Phys. Rev. Lett. **67**, 1334 (1991).

[11] V. Hardy, S. Majumdar, M. R. Lees, D. McK. Paul, C. Yaicle, and M. Hervieu, Phys. Rev. B **70**, 104423 (2004).

[12] B. Gutenberg and C. F. Richter, *Seismicity of the Earth and Associated Phenomena* (Princeton University Press, Princeton, 1949).

[13] J. P. Sethna, K. A. Dahmen, and C. R. Myers, Nature **410**, 242 (2001).

[14] E. Altshuler, T. H. Johansen, Y. Paltiel, P. Jin, K. E. Bassler, O. Ramos, Q. Y. Chen, G. F. Reiter, E. Zeldov, and C. W. Chu, Phys. Rev. B **70**, 140505 (2004).

[15] A. Shekhawat, S. Papanikolaou, S. Zapperi, and J. P. Sethna, Phys. Rev. Lett. **107**, 276401 (2011).

[16] F. J. Morin, Phys. Rev. Lett. **3**, 34 (1959).

[17] S. Guénon, S. Scharinger, S. Wang, J. G. Ramirez, D. Koelle, R. Kleiner, and I. K. Schuller, EPL **101**, 57003 (2013).

[18] A. Clauset, C. R. Shalizi, and M. E. J. Newman, SIAM Rev. **51**, 661 (2009).

[19] M. Sahimi, *Applications of Percolation Theory* (Taylor & Francis, London, 1994).

[20] M. Taya, *Electronic Composites* (Cambridge University Press, New York, 2005).

[21] O. Mishima and H. Eugene Stanley, Nature **396**, 329 (1998).

[22] M. Iwamatsu, J. Phys.: Condens. Matter **11**, L1 (1999).

[23] W. K. Kwok, J. Fendrich, S. Fleshler, U. Welp, J. Downey, and G. W. Crabtree, Phys. Rev. Lett. **72**, 1092 (1994).

[24] W. Wu and P. W. Adams, Phys. Rev. Lett. **74**, 610 (1995).

[25] S. B. Roy, M. K. Chattopadhyay, P. Chaddah, and A. K. Nigam, Phys. Rev. B **71**, 174413 (2005).

[26] M. K. Chattopadhyay, S. B. Roy, A. K. Nigam, K. J. S. Sokhey, and P. Chaddah, Phys. Rev. B **68**, 174404 (2003).

[27] T. Ito, H. Takagi, and T. Asano, Chem. Mater. **21**, 3376 (2009).

[28] D. Kumar, K. P. Rajeev, J. A. Alonso, and M. J. Martinez-Lope, J. Phys.: Condens. Matter **21**, 185402 (2009).

[29] W. Fan, J. Cao, J. Seidel, Y. Gu, J. W. Yim, C. Barrett, K. M. Yu, J. Ji, R. Ramesh, L. Q. Chen, and J. Wu, Phys. Rev. B **83**, 235102 (2011).

Chapter IV

Electrothermal induced transition in vanadium oxides

IV. 1 Introduction

Phase transitions, particularly first order phase transitions, can be induced by various stimuli such as temperature, pressure, chemical doping, electric field, charge injection and light. Multiple driving forces can indicate different mechanisms in the phase transitions. Voltage or current induced metal insulator transitions (MIT) in transition metal oxides, e.g. VO_2 [1, 2], NbO_2 [3], Fe_3O_4 [4, 5] and manganites [6], have been intensively studied. In many narrow-gap materials, this phenomenon has been attributed to the Mott transition [7]. When injected charge density exceed a critical density, according to the Mott criterion [8], a bandgap caused by electron repulsion should close and an MIT takes place. This process can be non-thermal and purely electronic [1], which does not require heating. However, some scientists have argued that Joule heating plays a significant role in voltage induced transitions [3, 5].

Vanadium oxides are prototypical narrow-gap insulators, exhibiting a voltage induced transition. The voltage induced transition in VO_2 has been studied with structural characterization techniques. In-situ X-ray diffraction [9, 10] and Raman scattering [11] on the micrometer scale have shown that there is no SPT occurs simultaneously with the voltage induced transition. This strongly supports the argument that the MIT in VO_2 is purely electronic, i.e. a Mott transition. However, observations of nanoscale phase coexistence [12] and avalanches [13] in VO_2 show that the MIT in VO_2 is inhomogeneous

at the nanoscale. As a result, nanoscale temperature measurements must be performed in vanadium oxides to understand the role of Joule heating in voltage induced transitions.

In this chapter, I will present a direct, local, quantitative thermal measurement on VO_2 during the voltage induced transition using fluorescence based scanning thermal microscopy (SThM) [14]. The results show that Joule heating is the predominant mechanism for the voltage induced transition in VO_2. I also extend the study to V_2O_3, which has been identified as a possible Mott insulator [15]. With low temperature SEM imaging, the voltage induced transition in V_2O_3 microdevices at T = 145 K is shown to be inhomogeneous at the nanoscale, as shown by the formation of electrothermal domains, i.e. metallic filaments. Numerical simulations reproduce the I-V characteristics and the formation of these metallic filaments. High current density and local temperature in the metallic filaments from the simulations suggest that as in VO_2, Joule heating induces the MIT in V_2O_3 microdevices at T = 145 K. However, the I-V characteristics of V_2O_3 microdevices at T = 155 K indicate that Joule heating may not account for the voltage induced transition. Other possible mechanisms will be discussed at the end of this chapter.

IV.2 Local temperature measurement on VO_2 microdevices

IV.2.1 Fluorescent thermal imaging technique

The experimental setup for the local temperature measurement on VO_2 microdevices is shown in Figure 4.1(a). To perform in-situ local temperature and I-V characteristic measurements, the VO_2 sample is mounted on a Peltier heater with a

calibrated PT-100 temperature sensor. Electrical transport measurements are carried out with a voltage sweep generator. The two resistors, 55 kΩ and 123 kΩ, are used to limit the current in the circuit, which is measured by the voltage drop over the 55kΩ resistor. A 975 nm laser is used to excite the fluorescent particle and the fluorescence is measured by a microscope and spectrometer.

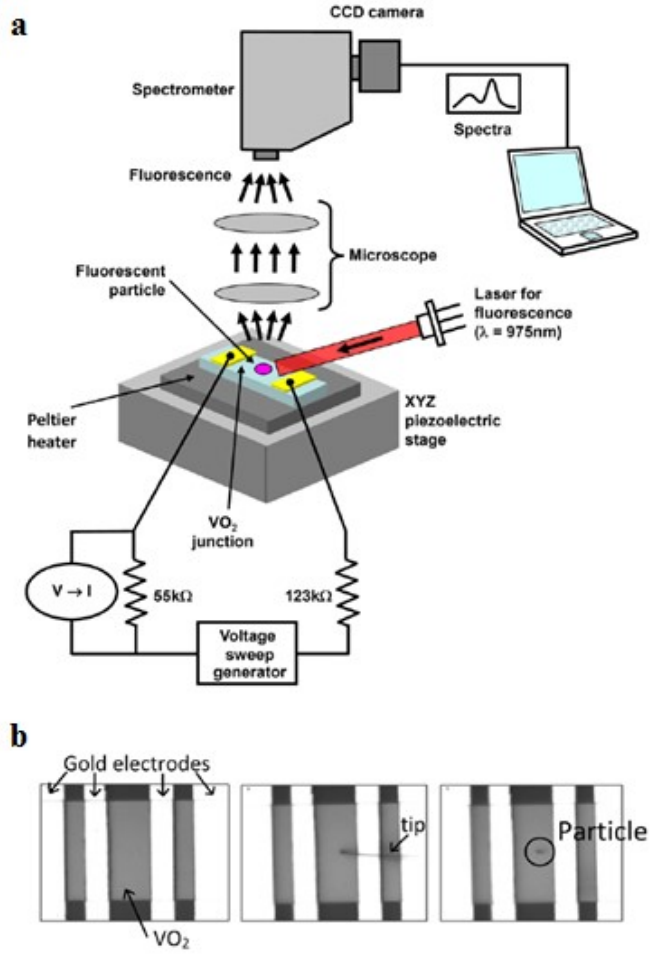

Figure 4.1. (a) Depiction of the experimental optical and electrical setup. (b) 20 μm device before, during and after positioning the micro-sized fluorescent particle on the device (from left to right). Reprinted from A. Zimmers *et al*., Phys. Rev. Lett. **110**, 056601 (2013). Copyright by the American Physical Society.

The VO_2 films are etched into 50 μm bars using reactive ion etching and the gold contacts are fabricated using photolithography. The fabrication process is described further in Chapter II. The distances between adjacent electrodes are 10 μm and 20 μm.

The local temperature measurements on VO_2 are performed with a ~ 1 μm fluorescent particle made of erbium/ytterbium codoped fluoride glass [14]. The particle is placed on the surface of the microdevices with a homemade nanomanipulator system, shown in Figure 4.1(b). When excited by near-infrared light (λ = 975 nm), the fluorescent particle absorbs two phonons and emits visible light. The fluorescent spectra show two peaks centered at λ = 520 nm and λ = 550 nm respectively (the inset of Figure 4.2). The ratio of the two peak areas (A_{520} and A_{550}, respectively) depends on the local temperature, described by Equation (4.1) [14]:

$$\frac{A_{520}}{A_{550}} = Be^{-D/T}. \tag{4.1}$$

To measure the surface temperature of the microdevices, parameters B and D in Equation (4.1) are determined by the following procedure. We first measure two fluorescent spectra at two calibration temperatures: room temperature 27°C and the MIT temperature 66°C, shown by colored triangles in Figure 4.2. These two temperatures are measured by the standard PT-100 temperature sensor mounted on the Peltier heater in Figure 4.1(a). With these two calibration points, we have B = 7.25 ± 0.3 and D = 1103 ± 30 K in good agreement with literature values [14, 16, 17]. To prove the equivalence between the local temperature measured by the fluorescent particle and the base temperature measured by the PT-100 sensor, we measured a series of fluorescent spectra at different base temperatures (Inset in Figure 4.2). Local temperatures are calculated with

Equation (4.1) and plotted with respect to the base temperatures in the black curve in Figure 4.2. Within 0.2°C, the local and base temperatures are equal. These calibrations show that the fluorescent spectra can measure the local temperature accurately.

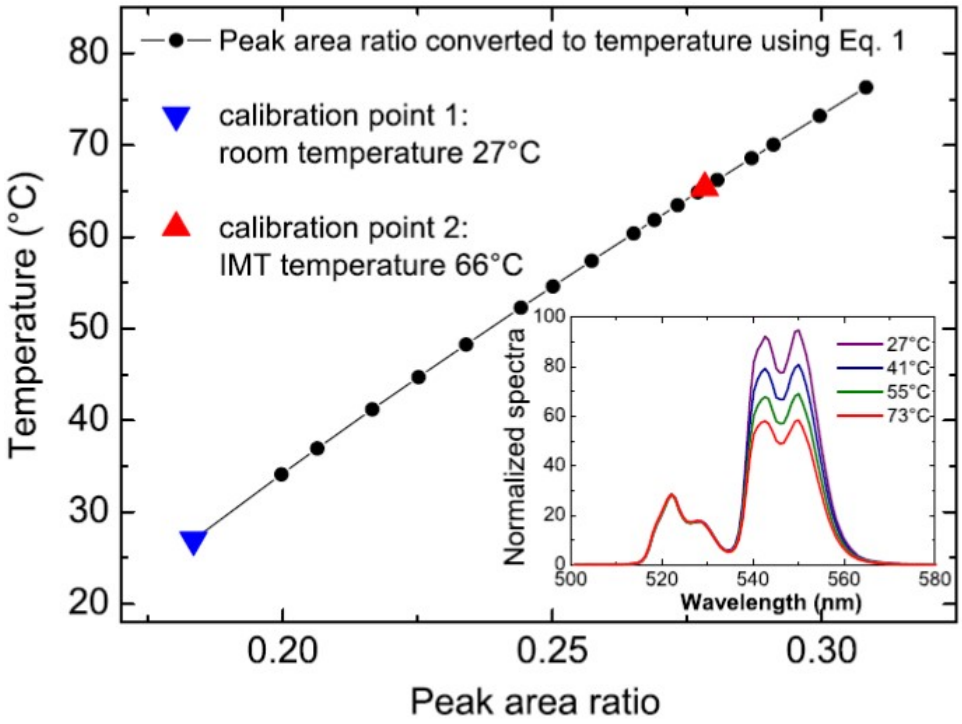

Figure 4.2. Local temperature versus base temperature and both calibration points (27°C and 66°C). Inset: Fluorescent spectra at different base temperatures. Reprinted from A. Zimmers *et al*., Phys. Rev. Lett. **110**, 056601 (2013). Copyright by the American Physical Society.

IV.2.2 I-V characteristic and local temperature

Electrical transport properties of the VO_2 devices are measured in the circuit shown in Figure 4.1(a). Resistance versus temperature (R-T) measurement of the 20 μm device shows over 4 orders of magnitude MIT (Figure 4.3(a)), indicating a high quality VO_2 film.

Current versus voltage (I-V) measurements of the 10 μm and 20 μm devices at different base temperatures show similar features, including a threshold voltage ($V_{Threshold}$ in Figure 4.3(b)). The threshold voltage decreases with increasing base temperature and decreasing device dimensions. When the applied voltage is below the threshold, the slope of the I-V curves increases with the increasing applied voltage, indicating a decreasing resistance of the devices. Above a certain threshold voltage, the device jumps to a bias point with a reduced voltage and a higher current. The resistance of the device decreases by one to two orders of magnitude, i.e. a voltage induced MIT occurs. It indicates that the VO_2 devices are not fully metallic since Figure 4.3(a) clearly shows that a full MIT involves much greater change in resistance. Note that the resistance of the load resistors in the circuit shown in Figure 4.1(a) is close to the resistance of the VO_2 devices before the voltage induced MIT occurs. When the voltage induced MIT takes place in the VO_2 devices, the resistance in the circuit decreases significantly, leading to a jump in the current. The corresponding electric field across the devices at $V_{Threshold}$ ranges from $1.5 – 2.6 \times 10^6$ V/m, close to the values reported previously [11].

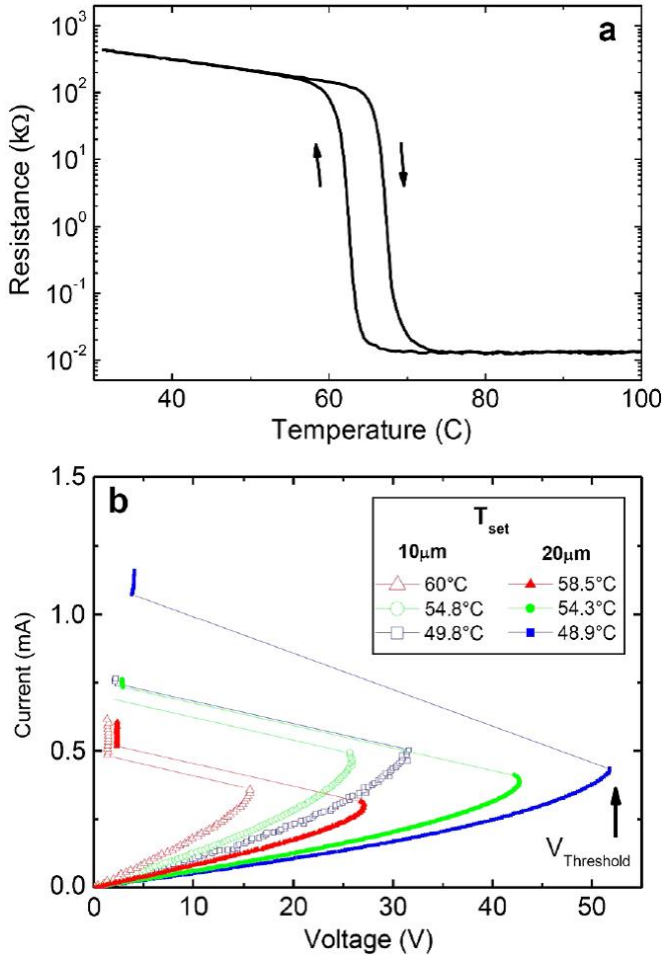

Figure 4.3. (a) R-T of the 20 μm VO_2 device. (b) I-V characteristics of the 10 μm and 20 μm VO_2 devices at different base temperatures. Reprinted from A. Zimmers *et al.*, Phys. Rev. Lett. **110**, 056601 (2013). Copyright by the American Physical Society.

Local temperatures are measured via the fluorescent spectra and electrical transport measurements are preformed simultaneously as depicted in Figure 4.1. For all the base temperatures, the local temperature increases with the applied voltage on each device, due to Joule heating, shown in Figure 4.4(a) and 4.4(c). When the applied voltages reach $V_{Threshold}$, the local temperatures reach the transition temperature range of the MIT of VO_2, shown by the shadowed regions in Figure 4.4(b) and (d). The fluorescent particle is placed

at various locations in the devices to check the homogeneity of the Joule heating before the transition takes place. The local temperatures are different by less than 0.5 °C at different locations, indicating a homogeneous Joule heating before the transition.

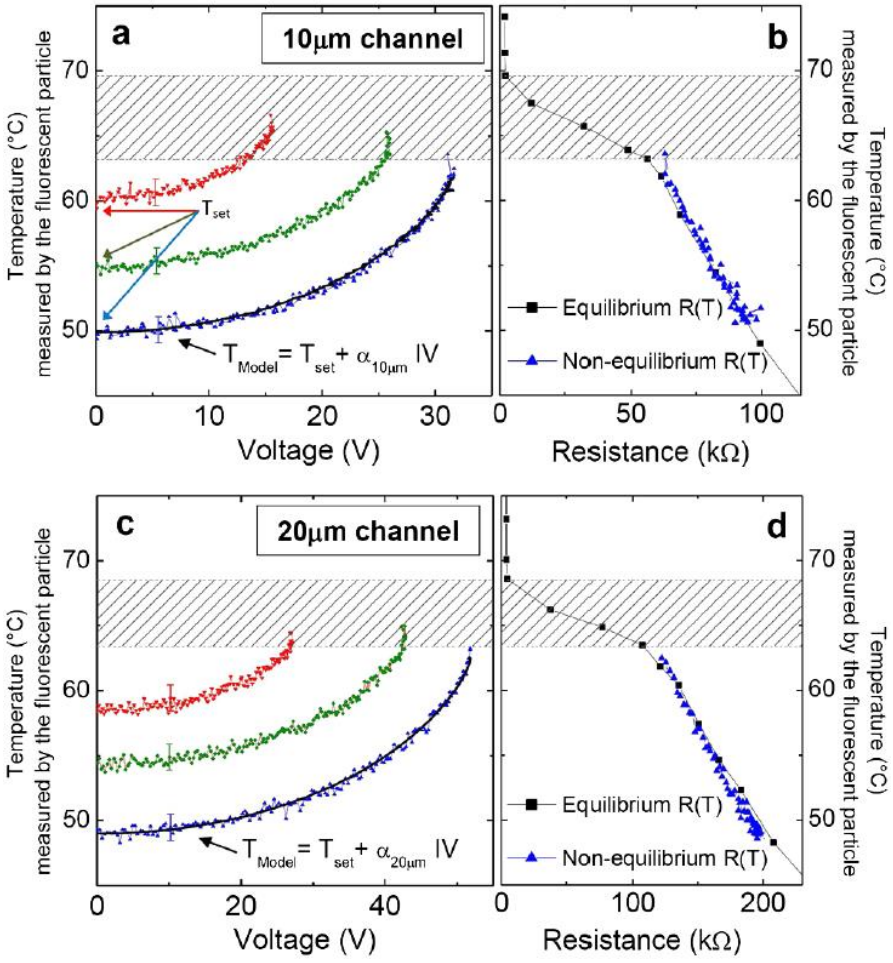

Figure 4.4. Local temperature versus voltage (a) and (c), and local temperature versus resistance (b) and (d) for the 10 μm and 20 μm devices. Reprinted from A. Zimmers *et al*., Phys. Rev. Lett. **110**, 056601 (2013). Copyright by the American Physical Society.

To further support the argument that Joule heating causes the MIT, the local temperature can be modeled by assuming Ohmic dissipation [18, 19] using Equation (4.2):

$$T_{model} = T_{set} + \alpha IV, \quad (4.2)$$

where T_{set} is the base temperature, T_{model} is the modeled local temperature and α the heat transfer coefficient or thermal resistance [19]. The modeled curves are plotted for both 10 μm and 20 μm devices in Figure 4.4(a) and (c). We find $\alpha_{10\mu m} = 750 \pm 5$°C/W from the measurements on the 10 μm device and $\alpha_{20\mu m} = 600 \pm 10$°C/W from the measurements on the 20 μm device. The coefficient is determined by the device dimensions and the thermal coupling with the heat sinks. The thermal coupling with the heat sinks is related to the thermal conductivity of VO_2 and the sapphire substrate, the thermal coupling between VO_2, the sapphire substrate and the metal electrodes, and the air flow during the experiment.

Equation (4.2) can be simplified to Equation (4.3) to better illustrate the linear dependence between the local heating and Joule heating power:

$$\Delta T = \alpha P, \quad (4.3)$$

where $\Delta T = T_{model} - T_{base}$ is the local temperature increase and $P = IV$ is the Joule heating power. Figure 4.5 shows that all the ΔT-P curves for different base temperatures superimpose onto a single straight line, implying that the coefficient α is temperature independent for each device.

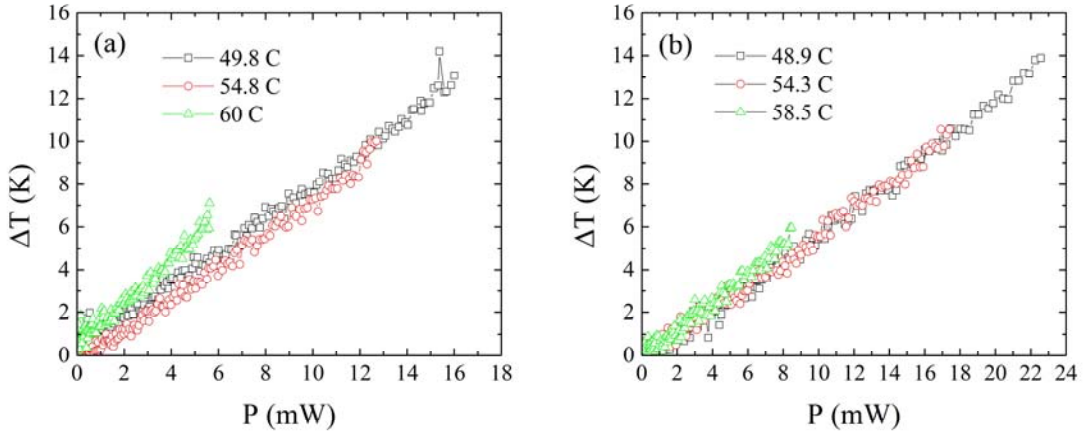

Figure 4.5. Local temperature increase versus power input for different base temperatures in (a) 10 μm and (b) 20 μm VO_2 devices.

Further evidence suggesting that Joule heating induces the transition is shown in Figure 4.4(b) and (d). The equilibrium R(T) curve is obtained by sweeping the global temperature with the Peltier heater and measuring the device resistance. The non-equilibrium R(T) curve is calculated from the I-V curves with a fixed global temperature using the local temperature to determine the temperature in the figure. The temperature is measured with the same fluorescent particle in both experiments. The equilibrium and non-equilibrium R(T) curves superimpose on each other, showing that the device is heated by the current.

IV.3 Low temperature SEM imaging on V_2O_3 microdevices

IV.3.1 Low temperature SEM technique

In this chapter, the study of voltage induced transitions is extended to another vanadium oxide, V_2O_3. Fluorescent local temperature measurements cannot be performed at cryogenic temperatures. Instead, we use low temperature SEM (LTSEM) [20, 21] to map out the metallic phase in the V_2O_3 devices. The LTSEM is a state of art SEM equipped with a liquid nitrogen cryostat. A schematic is shown in Figure 4.6. The sample (DUT in Figure 4.6) is mounted on a cold plate under vacuum. A periodically modulated electron beam is scanned across the sample surface (x-y plane), controlled by the xy-scanner. Due to the large working distance required by the IR-shielding of the cryostat, the minimum spot size of the e-beam is about 300 nm. A Keithley 2400 current source and a conventional preamplifier with a National Instruments measurement card are used for the 2-probe measurements.

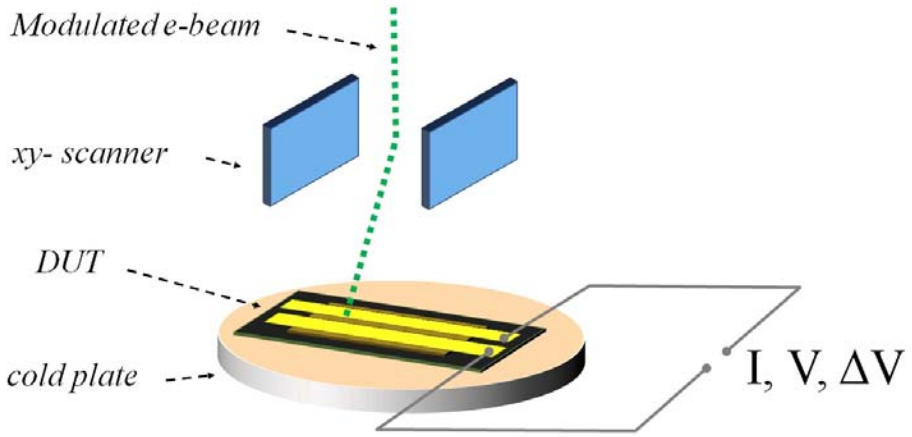

Figure 4.6. Schematic of the LTSEM.

The LTSEM signal is obtained by recording the voltage change (ΔV in Figure 4.6) when the beam blanking is on and off. This is detected by means of lock-in technique. When the e-beam is focused on the device, it causes a local heating δT at a location (x_0,y_0) on the device within the beam size Δx, shown in Figure 4.7(a). In the case of V_2O_3, the conductivity of the material increases when heated, sketched in Figure 4.7(b). The voltage change is given by Equation (4.4):

$$\Delta V(\mathrm{x_0}, \mathrm{y_0}) = I\left(R_{on} - R_{off}\right) = I\left(\frac{1}{G_i+\delta G_i} - \frac{1}{G_i}\right) \approx -I\frac{\delta G_i}{G_i^2} \tag{4.4}$$

where R_{on} and R_{off} are the resistance of the device when the e-beam is on and off, G_i the conductance of the slab highlighted in Figure 4.7(a) when the e-beam is off, and δG_i the conductance change caused by the e-beam. Considering the resistance of the slab $R_i = \frac{\Delta x}{L} R_{off}$, we have

$$G_i = \frac{1}{R_i} = \frac{L}{\Delta x R_{off}} \tag{4.5}$$

and

$$\delta G_i \approx \frac{\Delta y t}{\Delta x}\delta g \approx \frac{\Delta y t}{\Delta x}\frac{dg}{dT}\delta T, \tag{4.6}$$

where δg is the conductivity change of V_2O_3 and t is the thickness of V_2O_3, the voltage change can be written as

$$\Delta V(x0, y0) \approx -I\frac{st}{L^2}R_{off}^2\frac{dg}{dT}\delta T, \tag{4.7}$$

where s = $\Delta x \Delta y$ is the area of the e-beam spot. The specific heat of V_2O_3 between 100 – 200 K are on the same order of magnitude [22]. As a result, δT remains on the same order of magnitude when the electron beam is on the insulating and metallic phases. $\Delta V(x_0,y_0)$ is proportional to the applied current I and the derivative of the conductivity with respect to the temperature $\frac{dg}{dT}$. The applied current in this experiment is 1 – 10 mA. For the insulating phase, at T = 145 K we get $g_i \approx 26.6 \frac{1}{\Omega m}$ and $\frac{dg_i}{dT} \approx 1.37 \frac{1}{\Omega K m}$. For the metallic phase, we get $g_m \approx 1.43 \times 10^5 \frac{1}{\Omega m}$ and $\frac{dg_m}{dT} \approx -310 \frac{1}{\Omega K m}$. The difference in the conductivity and its derivative with respect to temperature between the insulating and metallic phases is 2 – 3 orders of magnitude. As a result, the contrast between the insulating and metallic phases in the LTSEM signal is large. In fact, only the metallic phase of V_2O_3 produces a visible LTSEM signal. In the following section, I will present the in-situ I-V characteristic and LTSEM measurements.

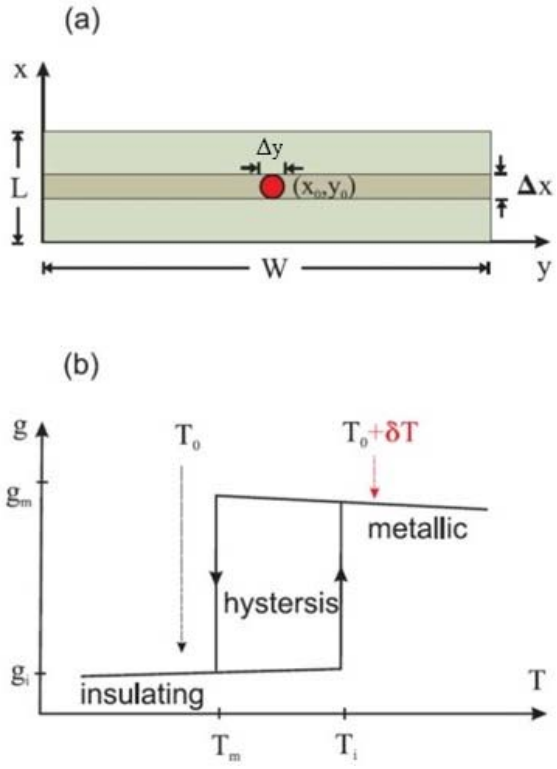

Figure 4.7. (a) Schematic of the device, where L and W are the length and width of the device, (x_0,y_0) is the e-beam spot location, and Δx and Δy are the spot sizes. (b) Sketch of the conductivity vs. temperature plot, where g_m and g_i are the conductivity of metallic and insulating V_2O_3, T_m and T_i are the hysteresis of the MIT, T_0 is the device temperature when beam blanked, and δT is the temperature increase caused by e-beam spot. Reprinted from S. Guenon *et al*., arXiv:1210.6648 (2012).

IV.3.2 I-V characteristic and low temperature SEM imaging

We performed in-situ I-V characteristic and LTSEM on a V_2O_3 microdevice as shown in Figure 4.8(a). A 200 μm V_2O_3 stripe was etched with reactive ion etching and gold electrodes with a 10 μm gap. The device was fabricated with photolithography as described in Chapter II. The device exhibits a MIT with more than three orders of magnitude resistance change as shown in Figure 4.8(b). I-V characteristics were measured at T = 145 K and T = 155 K. The I-V characteristics at these two temperatures shared two

common features. First, there was a large hysteresis between the up current-sweep and down current-sweep. Second, there was a training effect, i.e. the two consecutive I-V measurements showed different I-V characteristics. This training effect disappeared after the second or the third current cycle. The training effect reappeared after thermally cycling the device by cooling it to 80 K.

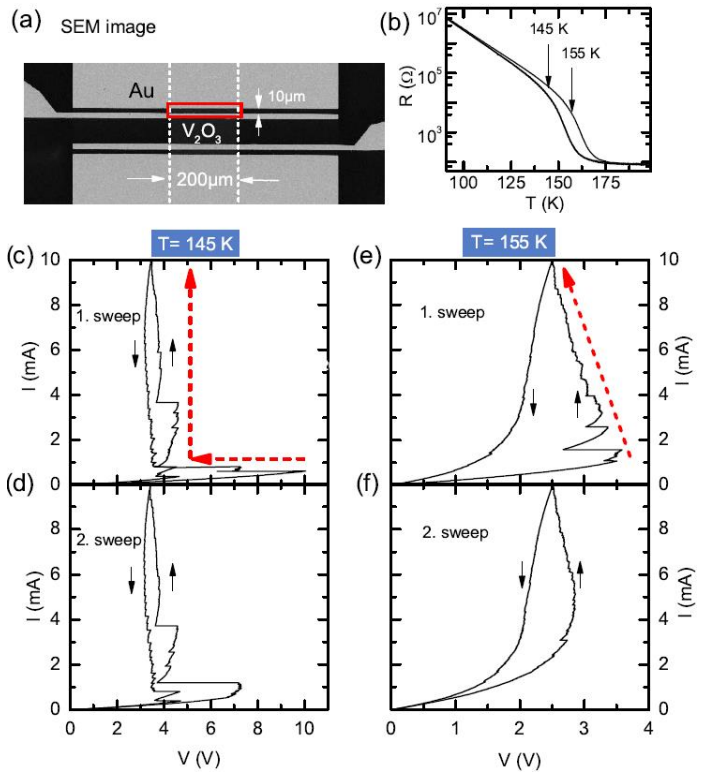

Figure 4.8. (a) SEM image of the V_2O_3 microdevice. (b) R-T characteristic of the V_2O_3 microdevice. (c-f) I-V characteristic of the V_2O_3 microdevice at T = 145 K and T = 155 K. (c,e) First current sweep. (d,f) Second current sweep. The black solid arrows indicate the current sweep direction and the red dashed arrows indicate the overall direction of the electrical breakdown. Reprinted from S. Guenon *et al.*, Europhys. Lett. **101**, 57003 (2013). Copyright by the Europhysics Letters Association.

The I-V characteristics at T = 145K and 155K exhibit distinct behaviors. At T = 145 K, there is always an electrical breakdown, i.e. a large voltage drop, when a 1 mA bias

current is applied. The second sweep shows a smaller breakdown than the first sweep at the same bias current. A second breakdown occurs at 4 mA bias current in both sweeps. At = 155 K, instead of an electrical breakdown, a sawtooth shaped I-V characteristic is observed in the first sweep, followed by a progression with a negative slope when the bias current is above 6 mA. The second sweep shows a rather smooth I-V characteristic and a negative differential resistance region.

For T = 145 K, in-situ LTSEM imaging is performed in the second sweep at various bias currents as show in Figure 4.9(a). Figure 4.9(f) shows a clear filament when the electrical breakdown occurs at bias point (f) in Figure 4.9(a). As we discussed in the previous section, the bright signal comes from the metallic phase of V_2O_3. This suggests that the electrical breakdown, i.e. voltage induced MIT in V_2O_3 does not occur homogeneously. In Figures 4.9 (b_z-k_z) we imaged the entire process of the metallic filament formation. From Figures 4.9(b_z-e_z) bright spots, i.e. metallic domains on the scale of 100's of nm nucleate in the V_2O_3 device before the voltage induced MIT occurs. From Figures 4.9(f_z-k_z) a bright filament forms and expands as the bias current increases after the voltage induced MIT occurs. This type of filament was also reported previously in VO_2 [23, 24]. It is important to note that the area of the bright filament after the transition (Figure 4.9(f_z)) is smaller than the area of all the bright dots before the transition (Figure 4.9(e_z)). As discussed in the previous section, the LTSEM signal is proportional to the applied current. This means that a current redistribution occurs after the transition, i.e. the current concentrates in the metallic filament.

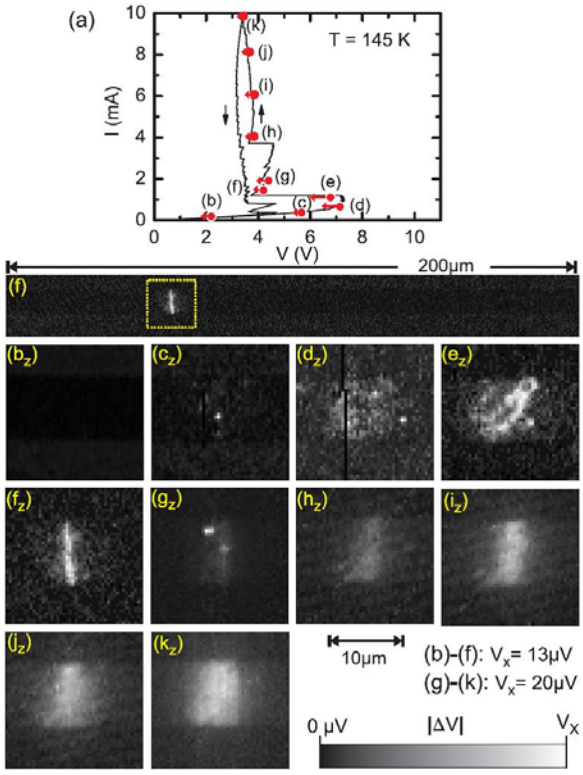

Figure 4.9. (a) I-V characteristic of the V_2O_3 microdevice, second sweep at T = 145 K. Red arrows indicates a small voltage decrease at each bias point when the e-beam is on. This is caused by local heating from the e-beam as discussed in the previous section. (f) LTSEM image of the V_2O_3 microdevice at bias point (f) in (a). The yellow dotted square indicates the zoomed area shown in (b_z-k_z). (b_z-k_z) Zoomed LTSEM images of the V_2O_3 microdevice at bias points (b-k) in (a). Reprinted from S. Guenon *et al*., Europhys. Lett. **101**, 57003 (2013). Copyright by the Europhysics Letters Association.

The voltage induced transition at T = 155 K behaves differently than the one at T = 145 K. The LTSEM imaging is performed during the first current sweep. When the bias current is applied, the bright spots appear at the same position in the device. As the current increases from bias points (b-k), the number of the bright spots increases and they eventually merge into a filament. The transition at this temperature occurs rather continuously and there is not abrupt electrical breakdown and current redistribution. This

imply that there may be a different mechanism for the voltage induced MIT at this temperature than at T = 145 K.

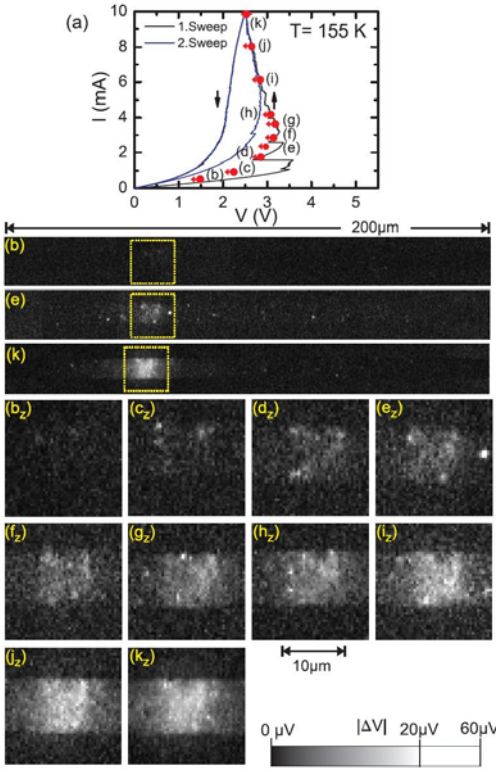

Figure 4.10. (a) I-V characteristic of the V_2O_3 microdevice, first and second sweep at T = 155 K. Red arrows indicates a small voltage decrease at each bias point when the e-beam is on. This is caused by local heating from the e-beam as discussed in the previous section. (f) LTSEM image of the V_2O_3 microdevice at bias point (f) in (a). The yellow dotted square indicates the zoomed area. (b_z-k_z) Zoomed LTSEM images of the V_2O_3 microdevice at bias points (b-k) in (a). Reprinted from S. Guenon *et al*., Europhys. Lett. **101**, 57003 (2013). Copyright by the Europhysics Letters Association.

IV.3.3 Simulation

To understand the physical mechanism of the voltage induced MIT in V_2O_3, we performed a numerical simulation. We assumed that the V_2O_3 microdevice is a two

dimensional diamond shaped resistor network as described in Ref. [25], shown in Figure 4.11. Each V_2O_3 domain is represented by a resistor in the network. As Figure 4.12(a) shows, each resistor has a different transition temperature T_C and a thermal hysteresis ΔT_C = 8 K. For the transition temperatures of the resistors, a Gaussian distribution with a mean value of 163 K and a standard deviation of 3.16 K is assumed. For each temperature, the resistance of the network can be calculated by solving the Kirchhoff equations for all the resistors. In our simulation, we used a 20 × 400 resistor network to represent the aspect ratio of the V_2O_3 microdevice. As shown in Figure 4.12(b), the measured (black dots) and simulated (red lines) R-T agree very well.

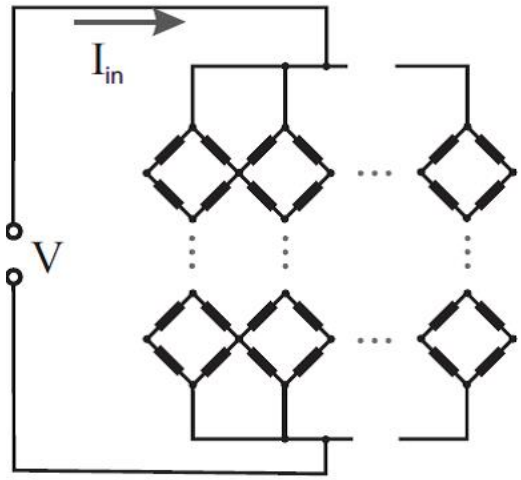

Figure 4.11. Schematic of the 2D diamond shaped resistor network. Reprinted from S. Guenon *et al*., arXiv:1210.6648 (2012).

In order to quantify the effect of Joule heating, we introduced a thermal cross coupling between nearest neighbors A_c and a thermal coupling to the heat sink, the sapphire

substrate, A_s. When a stable state is reached at a constant bias current, the Joule heating is balanced by heat dissipation for a domain j, which can be written as:

$$\sum_{i=1}^{N} A_c(T_j - T_i) + A_s(T_j - T_b) = IV \tag{4.8}$$

where domain i is a nearest neighbor to domain j, N = 4 is the number of the nearest neighbors and T_b is the base temperature in the substrate (or heat sink). We use $A_c = 5.0 \times 10^{-7}$ W/K and $A_s = 4.25 \times 10^{-7}$ W/K to reproduce the threshold voltage and current at T = 145 K. The edge cooling effect from the electrodes is neglected to simplify the simulations.

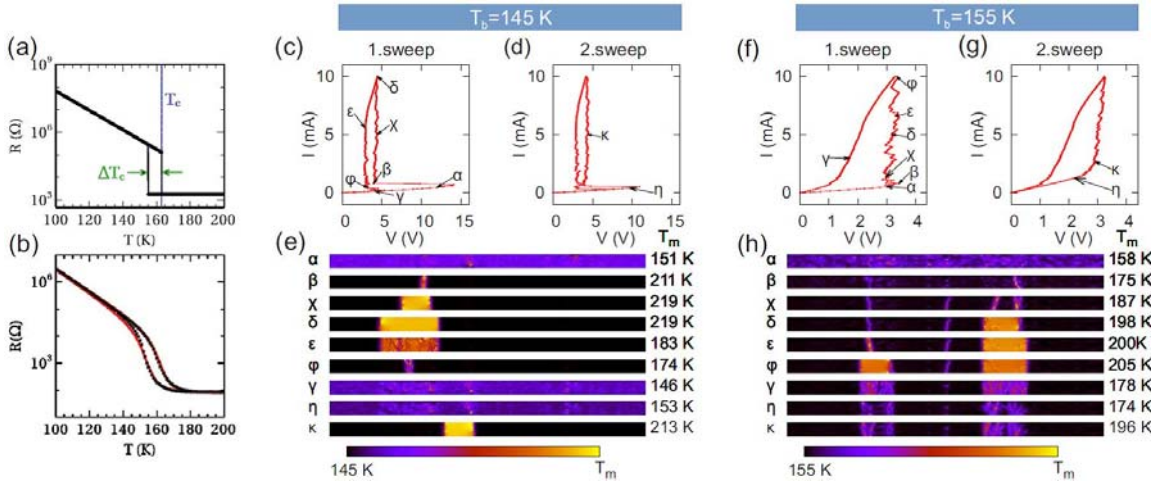

Figure 4.12. (a) R-T of a single V_2O_3 domain used in the simulation. (b) Measured R-T (black dots) and simulated R-T (red lines) of the V_2O_3 microdevice. (c,d) Simulated I-V of the V_2O_3 microdevice at T = 145 K. (c) the first sweep and (d) the second sweep. (e) Simulated temperature distribution in the V_2O_3 microdevice at different bias point in (c) and (d). The maximum temperature T_m for each bias point is on the right-hand side of the figure. (f,g) Simulated I-V of the V_2O_3 microdevice at T = 155 K. (f) the first sweep and (g) the second sweep. (h) Simulated temperature distribution in the V_2O_3 microdevice at different bias point in (f) and (g). The maximum temperature T_m for each bias point is on the right-hand side of the figure. Reprinted from S. Guenon *et al*., Europhys. Lett. **101**, 57003 (2013). Copyright by the Europhysics Letters Association.

With Equation (4.8), we are able to simulate the I-V characteristics of the V_2O_3 microdevice at T = 145 K and T = 155 K. The simulated I-V for T = 145 K is shown is Figure 4.12(c,d) and Figure 4.13(a,b). The simulated I-V curves reproduce the general shape of the measured I-V curves, including the threshold voltage and current, the magnitude of the breakdown, the hysteresis and training effect. The second breakdown at 4 mA is not reproduced in the simulation. This breakdown observed in the experiment possibly comes from defects in the V_2O_3 device acting as pinning sites that stop the expansion of the filament. The simulated temperature and current distributions are shown in Figure 4.12(e) and Figures 4.13(c-k). The filament formation and current redistribution after the electrical breakdown are reproduced. The local temperature in the simulated filament is higher than the transition temperature in the heating branch of the R-T curve (Figure 4.12(b)). The high current density and the high local temperature in the simulated filament suggests that Joule heating is responsible for the electrical breakdown, i.e. the voltage induced MIT. The hysteresis in the I-V can be attributed to the thermal hysteresis of V_2O_3. It is important to note that Figure 4.13(j) shows more metallic domains than Figure 4.13(c). This implies that the Joule heating does not drive the V_2O_3 microdevice to a fully metallic state. When the current is reduced, the V_2O_3 microdevice cools along a minor loop inside the full R-T curve. Without thermal cycling to 80 K, some of the domains remain metallic, i.e. the device does not return to its original state at T = 145 K. As a result, the I-V characteristic of the second current sweep is different from that of the first sweep. This is the cause of the training effect.

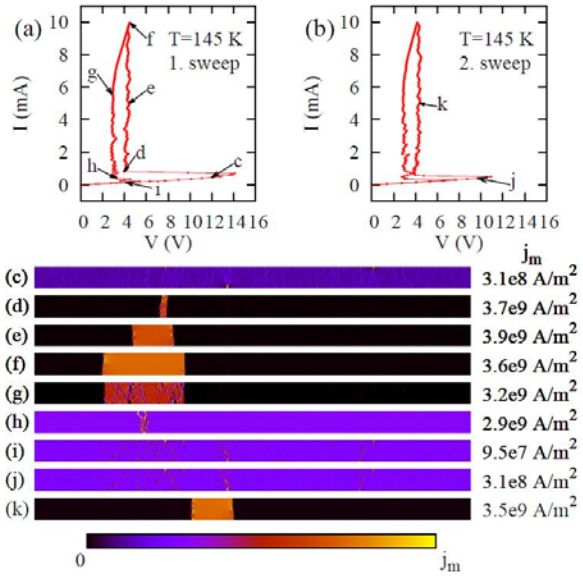

Figure 4.13. (a,b) Simulated I-V of the V_2O_3 microdevice at T = 145 K. (a) the first sweep and (b) the second sweep. (c-k) Simulated current distribution in the V_2O_3 microdevice at different bias point in (a) and (b). The maximum temperature j_m for each bias point is on the right-hand side of the figures. Reprinted from S. Guenon *et al*., arXiv:1210.6648 (2012).

The simulated I-V for T = 155 K is shown in Figures 4.12(f,g) and Figures 4.14(a,b). The simulation shows similar hysteresis and training effect as the measurements, but the general shape of the I-V curve is not reproduced at this temperature. The simulated I-V curves reproduce the sawtooth feature shown in the measurements in the first current sweep and become smoother in the second current sweep. However, the negative differential resistance is not reproduced in the simulation. The simulated temperature and current distribution (Figures 4.12(h) and Figures 4.14(c-k)) are also significantly different from the LTSEM images. In the simulation, multiple filaments form as the current increases. However, the LTSEM images clearly show the nucleation and growth of the metallic domains as previously discussed, which is different from the simulation.

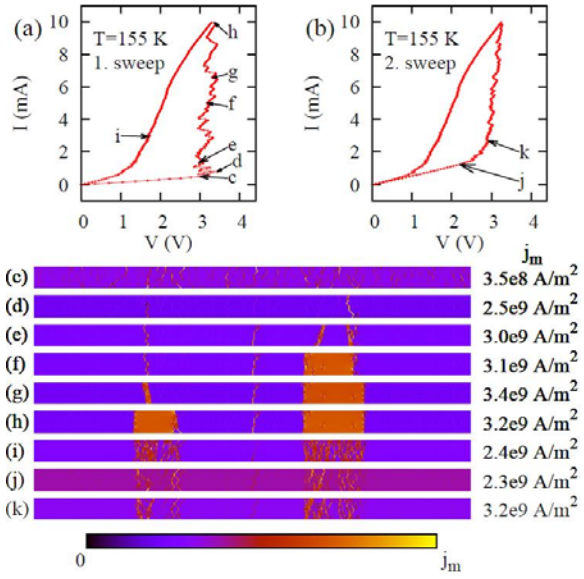

Figure 4.14. (a,b) Simulated I-V of the V_2O_3 microdevice at T = 155 K. (a) the first sweep and (b) the second sweep. (c-k) Simulated current distribution in the V_2O_3 microdevice at different bias points in (a) and (b). The maximum current density j_m for each bias point is on the right-hand side of the figures. Reprinted from S. Guenon *et al*., arXiv:1210.6648 (2012).

This continuous nucleation and growth indicates that the voltage induced MIT at T = 155 K might be attributed to a different mechanism. The numerical model is based on the assumption that each V_2O_3 domain has bistable states (Figure 4.12(a)). Yet if intermediate states exist between the insulating and metallic state of V_2O_3, the voltage induced MIT can occur continuously. An intermediate state can be induce by effects such as Landau-Zener tunneling, which requires an electric field as high as $10^6 – 10^7$ V/cm [26-29]. However, the applied electric field in this experiment is on the order of 10^4 V/cm, too low for tunneling to take place. To further understand this phenomenon, the V_2O_3 devices

need to be scaled to the metallic domain size, 100's of nm. At this length scale the electrical breakdown of a single domain can be investigated and the electric field can be enhanced.

IV.4 Conclusions

To summarize, in this chapter, I presented the role of Joule heating in the voltage induced transitions in vanadium oxides. With fluorescent microparticles, we performed local temperature measurements on VO_2 microdevices during the voltage induced transitions at different base temperatures. This experiment proved that Joule heating is the predominant mechanism in the voltage induced transition in VO_2.

I extended the study of the voltage induced transitions to V_2O_3 microdevices. LTSEM imaging showed that the voltage induced transitions in V_2O_3 microdevices do not occur homogeneously. Comparing the I-V characteristics and the LTSEM images with numerical simulations based on a Joule heating model, we found that the voltage induced transition at T = 145 K can be explained by Joule heating. However, the voltage induced transition at T = 155 K might be caused by a different mechanism.

IV.5 Acknowledgements

Chapter IV, in part (section IV.2), has been previously published in: A. Zimmers, L. Aigouy, M. Mortier, A. Sharoni, S. Wang, K. G. West, J. G. Ramirez, and I. K. Schuller, "Role of Thermal Heating on the Voltage Induced Insulator-Metal Transition in VO_2", Phys. Rev. Lett. **110**, 056601 (2013). The dissertation author was a co-author of this paper.

Chapter IV, in part (section IV.3), has been previously published in: S. Guenon, S. Scharinger, S. Wang, J. G. Ramirez, D. Koelle, R. Kleiner, and I. K. Schuller, "Electrical breakdown in a V_2O_3 device at the insulator-to-metal transition", Europhys. Lett. **101**, 57003 (2013). The dissertation author was a co-auther of this paper. Chapter IV, in part (section IV.3), has been previously published in: S. Guenon, S. Scharinger, S. Wang, J. G. Ramirez, D. Koelle, R. Kleiner, and I. K. Schuller, "Electrical Breakdown in a V_2O_3 device at the Insulator to Metal Transition", arXiv:1210.6648 (2012). The dissertation author was a co-auther of this paper.

IV.6 References

[1] G. Stefanovich, A. Pergament, and D. Stefanovich, J. Phys.: Condens. Matter **12**, 8837 (2000).

[2] H.-T. Kim, B.-G. Chae, D.-H. Youn, S.-L. Maeng, G. Kim, K.-Y. Kang, and Y.-S. Lim, New J. Phys. **6**, 52 (2004).

[3] M. D. Pickett and R. S. Williams, Nanotechnology **23**, 215202 (2012).

[4] S. Lee, A. Fursina, J. T. Majo, C. T. Yavuz, V. L. Colvin, R. G. S. Sofin, I. V. Shvets, and D. Natelson, Nat. Mater. **7**, 130 (2008).

[5] A. A. Fursina, R. G. S. Sofin, I. V. Shvets, and D. Natelson, Phys. Rev. B **79**, 245131 (2009).

[6] A. Asamitsu, Y. Tomioka, H. Kuwahara, and Y. Tokura, Nature **388**, 50 (1997).

[7] P. Stoliar, L. Cario, E. Janod, B. Corraze, C. Guillot-Deudon, S. Salmon-Bourmand, V. Guiot, J. Tranchant, and M. Rozenberg, Adv. Mater. **25**, 3222 (2013).

[8] N. F. Mott, *Metal-Insulator Transitions*, second edition (Tayler & Francis, London, 1990).

[9] K. Okimura, Y. Sasakawa, and Y. Nihei, Jpn. J. Appl. Phys. **45**, 9200 (2006).

[10] B.-J. Kim, Y. W. Lee, S. Choi, J.-W. Lim, S. J. Yun, H.-T. Kim, T.-J. Shin, and H.-S. Yun, Phys. Rev. B **77**, 235401 (2008).

[11] H.-T. Kim, B.-G. Chae, D.-H. Youn, G. Kim, K.-Y. Kang, S.-J. Lee, K. Kim, and Y.-S. Lim, Appl. Phys. Lett. **86**, 242101 (2005).

[12] M. M. Qazilbash, M. Brehm, B.-G. Chae, P.-C. Ho, G. O. Andreev, B.-J. Kim, S. J. Yun, A. V. Balatsky, M. B. Maple, F. Keilmann, H.-T. Kim, and D. N. Basov, Science **318**, 1750 (2007).

[13] A. Sharoni, J. G. Ramírez, and I. K. Schuller, Phys. Rev. Lett. **101**, 026404 (2008).

[14] L. Aigouy, G. Tessier, M. Mortier, and B. Charlot, Appl. Phys. Lett. **87**, 184105 (2005).

[15] S. Yu. Ezhov, V. I. Anisimov, D. I. Khomskii, and G. A. Sawatzky, Phys. Rev. Lett. **83**, 4136 (1999).

[16] M. A. R. C. Alencar, G. S. Maciel, C. B. de Araujo, and A. Patra, Appl. Phys. Lett. **84**, 4753 (2004).

[17] F. Vetrone, R. Naccache, A. Zamarron, A. J. de la Fuente, F. Sanz-Rodriguez, L. M. Maestro, E. M. Rodriguez, D. Jaque, J. G. Sole, J. A. Capobianco, ACS Nano **4**, 3254 (2010).

[18] Y. F. Chen, M. Ziese, and P. Esquinazi, Appl. Phys. Lett. **89**, 082501 (2006).

[19] A. S. Alexandrov, A. M. Bratkovsky, B. Bridle, S. E. Savel'ev, D. B. Strukov, and R. S. Williams, Appl. Phys. Lett. **99**, 202104 (2011).

[20] J. R. Clem and R.P. Huebener, J. Appl. Phys. **51**, 2764 (1980).

[21] R. Gross and D. Koelle, Rep. Prog. Phys. **57**, 651 (1994)

[22] H. V. Keer, H . L. C. Barros, D. L. Dickerson, A. T. Barkfnecht, and J. M. Honig, Mat Res Bull **12**, 137 (1977).

[23] C. N. Berglund, IEEE Trans. Electron. Devices **16**, 432 (1969).

[24] J. Duchene, M. Terraillon, P. Pailly, and G. Adam, Appl. Phys. Lett. **19**, 115 (1971).

[25] A. Shekhawat, S. Papanikolaou, S. Zapperi, and J. P. Sethna, Phys. Rev. Lett. **107**, 276401 (2011).

[26] T. Oka, R. Arita, and H. Aoki, Phys. Rev. Lett. **91**, 066406 (2003).

[27] S. Okamoto, Phys. Rev. Lett. **101**, 116807 (2008).

[28] M. Eckstein, T. Oka, and P. Werner, Phys. Rev. Lett. **105**, 146404 (2010).

[29] F. Heidrich-Meisner, I. González, K. A. Al-Hassanieh, A. E. Feiguin, M. J. Rozenberg, and E. Dagotto, Phys. Rev. B **82**, 205110 (2010).

Chapter V

Novel magnetic properties of vanadium oxide/ferromagnet bilayers

V.1 Introduction

Manipulating the coercivity and magnetization of a ferromagnet has been a fundamental problem in the design of magnetic recording devices. Methods of controlling magnetism without an applied magnetic field is an on-going research topic of interest in both solid state physics and electrical engineering, due to its technological potential [1-4]. Electric field [1-4], current [5-7], pressure [8-10], heat [11, 12], microwaves [13, 14], acoustic waves [15] and light [16] have been used to modify and reverse the magnetization or assist the magnetization reversal. One possible solution is to use strongly correlated multiferroic materials in which different degrees of freedom such as lattice, charge and spin are strongly coupled [2]. However, to satisfy the requirements for magnetic recording, e.g. coercivity, saturation magnetization and Curie temperature, the choice of materials is limited. An alternative solution is to fabricate thin film hybrid structures containing standard magnetic materials in proximity to materials with high susceptibility to external stimuli such as electric field, pressure, heat, light and etc. [17, 18].

Figure 5.1 illustrates the candidate magnetic hybrid structures that could be used to control magnetism. The ferromagnet/antiferromagnet (FM/AF) structures exhibit the most intensively studied and most widely applied phenomenon in magnetic hybrid structures, exchange bias [19]. In an exchange biased system, the coercivity of ferromagnets can be enhanced and the magnetization can be stabilized against thermal fluctuations [20]. Control of magnetism can be achieved in a multiferroic/ferromagnetic system as well. Multiferroic

materials such as $BiFeO_3$ exhibit coupled ferroelectricity and antiferromagnetism [21]. Electric fields can control both the antiferromagnetism and ferroelectricity in a FM/$BiFeO_3$ exchange bias system [21]. More recently, magnetization reversal using electric fields has been demonstrated with CoFe/$BiFeO_3$ [3]. Electric fields can also control the magnetism in ferromagnetic/ferroelectric (FM/FE) systems e.g. Fe/$BaTiO_3$, through the inverse piezoelectric effect [22].

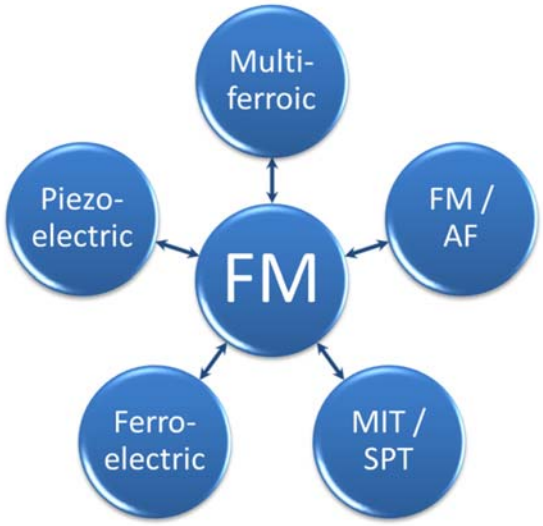

Figure 5.1. Illustration of possible magnetic hybrid structures. FM: ferromagnetic, AF: Antiferromagnetic, MIT: metal insulator transition, SPT: structural phase transition. Reprinted from T. Saerbeck *et al*., J. Mater. Res. (2014). Copyright by the Materials Research Society.

Materials exhibiting structural phase transitions (SPT) can also be used to control magnetic properties such as coercivity and magnetization. For instance, in addition to being a ferroelectric material, $BaTiO_3$ exhibits multiple SPTs at different temperatures [22]. In a

Fe/$BaTiO_3$ bilayer, the SPTs of $BaTiO_3$ at T = 190 K can induce an interfacial stress and change the coercivity by as much as 120 % [22]. This coercivity change occurs over a range of 10 – 15 K and without the application of any electric field [22].

Vanadium oxides could potentially be used for the control of magnetism, because the first order phase transitions cause abrupt volume changes within a narrow temperature range (10 – 15 K). The SPTs of vanadium oxides can offer more flexible control of magnetism since their SPTs can be induced by voltage [23], light [24] and pressure [25], and the transition temperatures can be changed by doping [25, 26], pressure [25] and stress [27]. In this chapter, I will discuss the control of magnetism in vanadium oxide/ferromagnet bilayers. VO_2 exhibits a SPT at 340 K, going from a low temperature monoclinic structure to a high temperature rutile structure. V_2O_3 exhibits a SPT at 150 – 165 K, going from a low temperature monoclinic structure to a high temperature rhombohedral structure. The SPT of vanadium oxides is described in details in Section I.2 of Chapter I. The SPT of vanadium oxides tailors the magnetic properties of the ferromagnets through interfacial stress. This effect can be tuned by selecting different deposition temperatures and ferromagnetic materials. A ~ 300 % coercivity enhancement in V_2O_3/Ni bilayers was observed during the SPT. This effect is attributed to the disorder induced by the inhomogeneous phase transition of V_2O_3.

V.2 Control of magnetism in VO_2/ferromagnet bilayers

V.2.1 Control of coercivity and magnetization in VO_2/Ni

We deposited 100 nm VO_2/10 nm Ni bilayers as shown in Figure 5.2. The VO_2 deposition process is described in Chapter II. The Ni was deposited at 150 °C with 100 W RF power and 4 mTorr Ar pressure.

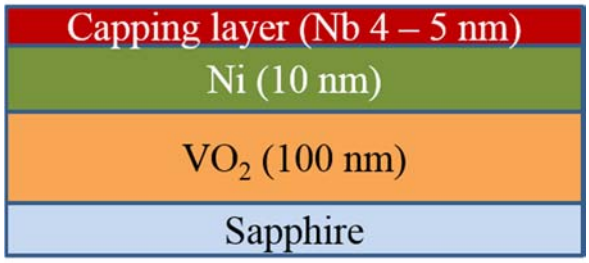

Figure 5.2. Schematic of 100 nm VO_2/10 nm Ni deposited on r-plane sapphire. A 4 – 5 nm Nb capping layer is deposited to avoid surface oxidation.

Magnetic hysteresis loops shown in Figure 5.3 are measured in a Quantum Design superconducting quantum interference device magnetometer (SQUID) and a vibrating sample magnetometer (VSM). We measured the in-plane hysteresis loop of a 100 nm VO_2/10 nm Ni bilayer at various temperatures across the SPT of VO_2. The coercivity of Ni decreases with increasing temperature. Between 320 K and 340 K, the coercivity changes by a factor of two as the SPT of VO_2 takes place. The ratio between the remanent magnetization M_r and the saturation magnetization M_s also decreases with increasing temperature. This behavior is independent of the in-plane magnetic field direction.

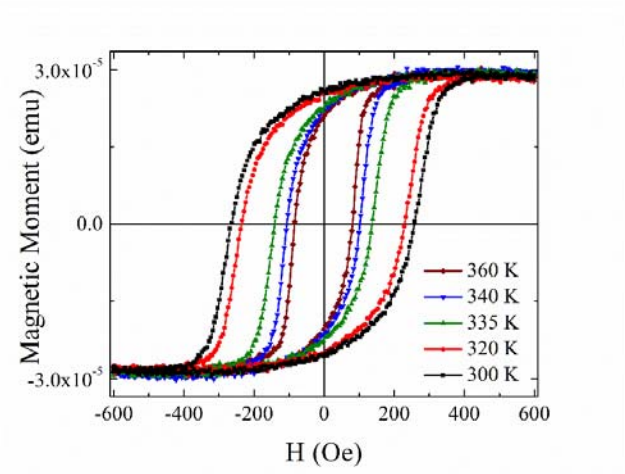

Figure 5.3. In-plane hysteresis loops at various temperatures for a 100 nm VO_2/10 nm Ni bilayer. Reprinted from J. de la Venta *et al*., Appl. Phys. Lett. **102**, 122404 (2013). Copyright by the American Institute of Physics.

Figure 5.4 shows the correlation between the Ni coercivity and the MIT and SPT of VO_2. Figure 5.4(a) shows the MIT of VO_2. Note that the resistance change at the VO_2 MIT is less than the four orders of magnitude resistance change reported in the previous chapters. The resistance of the metal layers on top of VO_2 is close to the resistance of the metallic phase of VO_2. At low temperature, the current flows through the metal layers and the resistance of the insulating phase of VO_2 cannot be directly measured through transport measurements. However, the factor of two change in resistance shows that the MIT takes place in VO_2. Figure 5.4(b) shows the SPT of VO_2. The out-of-plane XRD data is normalized to its integration. The normalized data fitted to two Gaussian functions centered at $2\theta = 37.06°$ for the monoclinic (200) and $2\theta = 37.17°$ for the rutile (011). The FWHM is kept constant for both Gaussian functions at all temperatures. The intensity is the

integration of the Gaussian function for one phase. This shows the shift of the diffraction peak from the monoclinic phase to the rutile phase with increasing temperature in the XRD across the SPT of VO_2 and vice versa. Figure 5.4(c) shows that the coercivity change in Ni occurs at the MIT and SPT temperatures of VO_2 and exhibits the same thermal hysteresis, i.e. the change in the coercivity correlates with the MIT and SPT of VO_2.

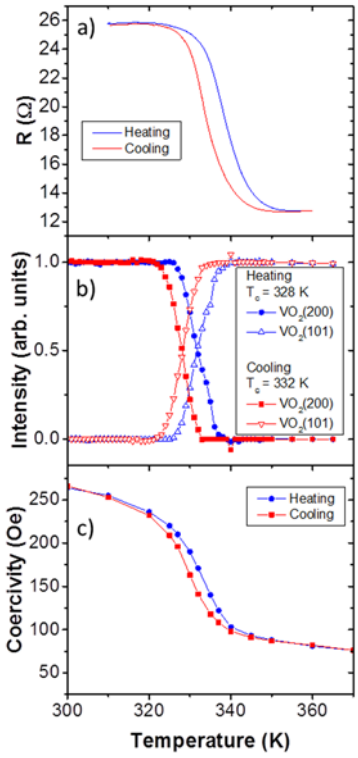

Figure 5.4. Correlation among the coercivity of Ni, the MIT and SPT of VO_2. (a) Resistance versus temperature of VO_2/Ni. (b) SPT of VO_2. (c) Coercivity versus temperature of VO_2/Ni. Reprinted from T. Saerbeck *et al.*, J. Mater. Res. (2014). Copyright by the Materials Research Society.

We studied the VO_2/Ni bilayers with different Ni thicknesses. For 10 nm Ni grown on sapphire (the blue squares in Figure 5.5), the coercivity shows a linear temperature dependence. In VO_2/Ni, the coercivity changes more quickly with respect to temperature across the SPT of VO_2. This effect exists for Ni thicknesses up to 100 nm although this effect is reduced with increasing Ni thickness, indicating that it is an interfacial effect.

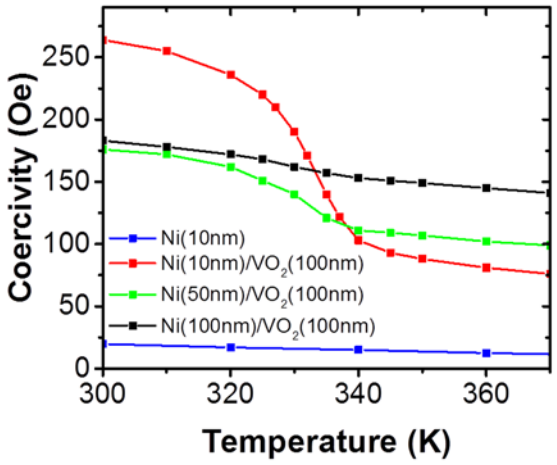

Figure 5.5. Coercivity versus temperature of 10 nm Ni on sapphire (blue squares), 10 nm Ni (red squares), 50 nm Ni (green squares) and 100 nm Ni (black squares) on 100 nm VO_2. Reprinted from T. Saerbeck *et al.*, J. Mater. Res. (2014). Copyright by the Materials Research Society.

V.2.2 Inverse magnetostriction and stress anisotropy

We attribute the temperature dependence of the coercivity of VO_2/Ni bilayers to inverse magnetostriction. Magnetostriction is the change in the dimension along the applied field direction when a ferromagnetic material is magnetized [28]. It is quantitatively defined by Equation (5.1):

$$\lambda = \frac{\Delta L}{L}, \tag{5.1}$$

where λ is the magnetostriction coefficient, L the length of the ferromagnet in demagnetized state and ΔL the change in length. If $\lambda > 0$, the ferromagnet elongates when magnetized; if $\lambda < 0$, the ferromagnet contracts when magnetized. If λ is measured from the demagnetization state to the saturation state, it is called the saturation magnetostriction λ_{si}.

Magnetostriction occurs when magnetic fields cause magnetic domain rotations and domain wall motions [28]. It does not change the saturation magnetization, i.e. it does not increase or decrease the magnetic moments. Magnetostriction originates from spin-orbital coupling in ferromagnetic materials [28]. The magnitude and the sign of the coefficient depend on the ferromagnetic materials and the applied field direction with respect to the crystal orientation [28]. Typically, the magnitude of the magnetostriction coefficient is on the order of $10^{-6} – 10^{-5}$ for nickel, cobalt and iron [28]. The sign of the magnetostriction coefficient for nickel, cobalt and iron along different crystal orientations is illustrate in Table 5.1.

Table 5.1. The sign of the magnetostriction coefficient for Ni, Co and Fe along different crystal orientations from Ref. 28.

Materials	[001]	[110]	[111]	Polycrystalline
Ni	-	-	-	-
Co	zero	-	-	-
Fe	+	+(low field) -(high field)	-	+(low field) - (high field)

Inverse magnetostriction is the change in the magnetization when a stress is applied on a ferromagnet [28]. For ferromagnetic materials with $\lambda < 0$, during the initial magnetization, the magnetization increases under a compressive stress or decreases under a tensile stress. Ferromagnetic materials with $\lambda > 0$ exhibit the opposite behavior. The stress induces a stress anisotropy field given by Equation (5.2):

$$H_{K\sigma} = \frac{3\lambda_{si}\sigma}{M_S}, \tag{5.2}$$

where σ is the applied stress, λ_{si} is the saturation magnetostriction and M_S is the saturation magnetization. As shown in Figure 5.5, the coercivity of Ni on sapphire has a linear temperature dependence. Without any applied stress, the coercivity at 320 K should be 105 Oe in Figure 5.4(c) if extrapolated from the linear temperature dependence at the high temperature. However, the measured coercivity value at 320 K is 236 Oe, 128 Oe higher in Figure 5.4(c). This is attributed to the stress anisotropy field induced by the SPT of VO_2. Assuming that the stress is homogeneous in the Ni film and considering $\lambda_{si} = -34 \times 10^{-6}$ and $M_S = 470$ emu/cm^3 for polycrystalline Ni [28], the stress $\sigma = 58.9$ MPa can be calculated from Equation (5.2).

V.2.3 Tailoring the stress with deposition temperatures

We are able to control the stress by selecting the deposition temperature for the Ni depositions (Figure 5.6). Ni films deposited at 420 K and room temperature show opposite behavior. The coercivity decreases and the magnetization increases with increasing temperature for Ni deposited at 420 K. Conversely, the coercivity increases and the

magnetization decreases with increasing temperature for Ni deposited at room temperature, indicating opposite types of induced stress in the Ni.

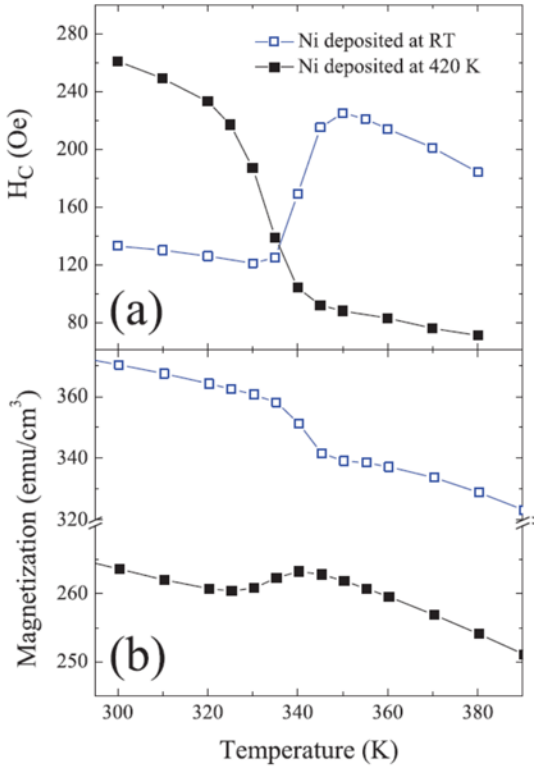

Figure 5.6. (a) Temperature dependence of coercivity of 100 nm VO_2/10 nm Ni. (b) In plane SQUID magnetization versus temperature measured at 1000 Oe with no diamagnetic correction. Ni layers were deposited at 420 K (solid squares) and room temperature (empty squares). Reprinted from J. de la Venta *et al*., Appl. Phys. Lett. **102**, 122404 (2013). Copyright by the American Institute of Physics.

The stress in a VO_2 film was measured by in-situ wafer curvature measurements and a 400 MPa tensile stress is induced in VO_2 by the SPT [29]. However, the stress in Ni is lower and can have a different sign. The transfer of the stress from VO_2 to Ni is related to several effects. The SPT of VO_2 occurs through a pairing and displacement of the

vanadium atoms in the c-axis of the rutile phase. This gives rise to an anisotropic atomic rearrangement on the (011) plane of the rutile phase, which produces a shear stress. In addition to this lattice distortion, there are other effects that can affect the interfacial stress: the coexistence of the monoclinic and rutile phases [30], the presence of the twin boundaries in the monoclinic phase [31, 32] and the interface roughness and alloying. This makes a theoretical prediction of the stress in Ni difficult. However, with inverse magnetostriction, an experimental estimate of the type and magnitude of the stress can be achieved.

V.2.4 Ferromagnets with different magnetostrictions

We extended the study to another vanadium oxide, V_2O_3, and compared bilayers prepared with different ferromagnets. Figure 5.7 (a) and (b) compare Ni with Co and Fe. There are two differences observed among Ni, Co and Fe. First, the coercivity change in Co and Fe is 10 Oe and 20 Oe, respectively. This is lower than the 100 Oe coercivity change in Ni. Second, the coercivity of Fe shows an opposite temperature dependence to Ni and Co across the SPT of V_2O_3. The coercivity of Fe increases with increasing temperature. According to Equation (5.2), if the applied stress σ on all the ferromagnetic materials is the same, the stress anisotropy field $H_{K\sigma}$ is determined by the ratio $\frac{\lambda_{si}}{M_S}$ of the ferromagnetic materials. For polycrystalline Co this ratio is 9 times lower than that for polycrystalline Ni; for polycrystalline Fe this ratio is 17 times lower than that for polycrystalline Ni [28, 33]. The stress anisotropy field in Co is 10 time lower than that in Ni; the stress anisotropy field in Fe is 5 times lower than that in Ni. This implies that stress in Fe is higher than that in Ni

and Co. The magnetostriction coefficient of Fe at low magnetic field has an opposite sign to Ni and Co [28]. This causes the increase of coercivity in Fe with increasing temperature.

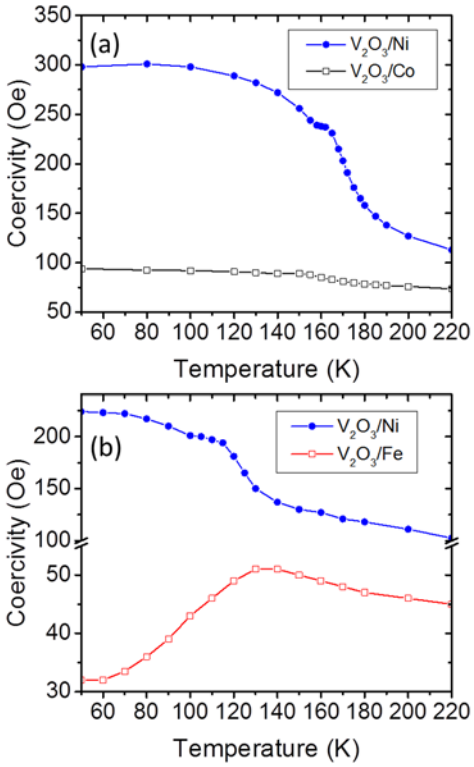

Figure 5.7. Coercivity versus temperature for 100 nm V_2O_3/10 nm FM with FM = Ni, Co (a) and Ni, Fe (b). Reprinted from T. Saerbeck *et al*., J. Mater. Res. (2014). Copyright by the Materials Research Society.

V.3 Coercivity enhancement in V_2O_3/Ni

V.3.1 Anomalous coercivity enhancement in V_2O_3/Ni

In this section, I present our study on a different set of V_2O_3/Ni bilayers. We preformed VSM measurements on 100 nm V_2O_3/10 nm Ni at various temperatures across

the SPT of V_2O_3, shown in Figure 5.8. As highlighted by the enlarged empty symbols, the coercivity of Ni in the middle of the transition (165 K) is higher than above (180 K) and below (100 K) the transition. We refer to this maximum coercivity as the coercivity enhancement in this section.

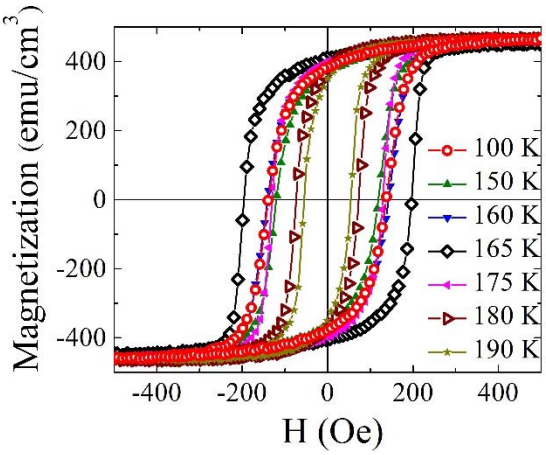

Figure 5.8. In-plane magnetic hysteresis loop of 100 nm V_2O_3/10 nm Ni at various temperatures across the SPT of V_2O_3. Three temperatures, above, in the middle of and below the SPT of V_2O_3 are highlighted with enlarged empty symbols. Reprinted from J. de la Venta *et al*., Appl. Phys. Lett. **104**, 062410 (2014). Copyright by the American Institute of Physics.

Figure 5.9 shows the correlation between the MIT and SPT of V_2O_3 and the coercivity enhancement of V_2O_3/Ni. Figure 5.9(a) shows the MIT of V_2O_3. Note that in these samples, the change in at the MIT of V_2O_3 is less than 5 orders of magnitude because of the metallic overlayer.. The resistance of the metallic layers on top of V_2O_3 is close to the resistance of the metallic phase of V_2O_3. At low temperature the current flows through the metal layers and the resistance of the insulating phase of V_2O_3 is not observable. The

resistance of the Ni layer is about 13 Ω from 130 K to 180 K, while the resistance of the V_2O_3 layer decreases from 10^7 Ω to 70 Ω. Consider that the Ni and V_2O_3 layers are two resistors in parallel, the resistance changes from 13 Ω at low temperature to 11 Ω at high temperature, showing the MIT in V_2O_3.

Figure 5.9(b) shows the SPT of V_2O_3. The out-of-plane XRD data is normalized to its integration. The normalized data is fitted to two Gaussian functions centered at $2\theta = 24.07°$ for the monoclinic (110) and $2\theta = 24.35°$ for the rhombohedral (012). The FWHM is kept constant for both Gaussian functions at all temperatures. The intensity is the integration of the Gaussian function for one phase. This shows the shift of the monoclinic peak to the rhombohedral peak with increasing temperature in the XRD across the SPT of V_2O_3 and vice versa. Figure 5.9(c) shows that the coercivity change of Ni is correlated in temperature with the MIT and SPT of V_2O_3 and exhibits a thermal hysteresis. The coercivity difference between 150 K and 180 K can be attributed to the stress induced by the SPT of V_2O_3 as discussed in the previous section. The coercivity is enhanced by 300 % from 180 K to 160 K at the middle of the SPT of V_2O_3. This will be explained in the next section.

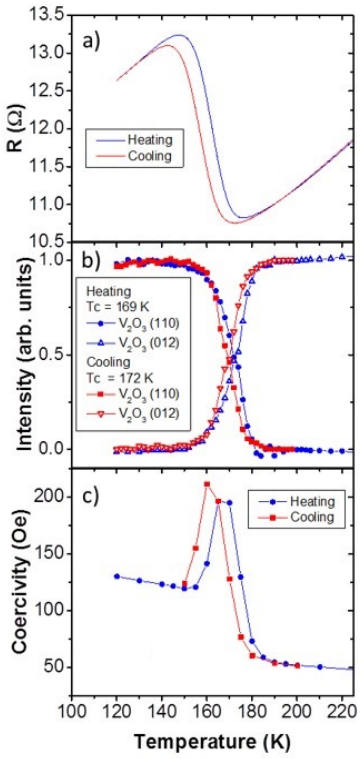

Figure 5.9. (a) MIT and (b) SPT of V_2O_3. (c) Coercivity versus temperature of V_2O_3/Ni. Reprinted from T. Saerbeck *et al*., J. Mater. Res. (2014). Copyright by the Materials Research Society.

V.3.2 Phase coexistence in V_2O_3 and competing length scales in V_2O_3/Ni

In Chapters III and IV, it was shown that the phase transition in vanadium oxide occurs through the nucleation and growth of the metallic domains during heating, or the insulating domains during cooling. In the phase transition range, the two phases coexist on the nanoscale. We attribute the coercivity enhancement in Ni to the nanoscale phase coexistence during the SPT of V_2O_3. Metallic domains on the order of 10 – 100's of nm have been observed with various imaging techniques [30, 34, 35]. Ni in contact with different structural phases of V_2O_3 experiences different stresses. This spatially

inhomogeneous stress leads to a temperature dependent disorder in Ni, which reaches a maximum when the volume fractions of the two phases are equal at 160 – 170 K. If the domain size of V_2O_3 is smaller than the magnetic domain size of Ni, the V_2O_3 domains can induce pinning at the boundary, which separate the magnetic domains of Ni and pin the magnetic domain wall. This gives rise to the enhanced coercivity in the hysteresis loops at 160 – 170 K.

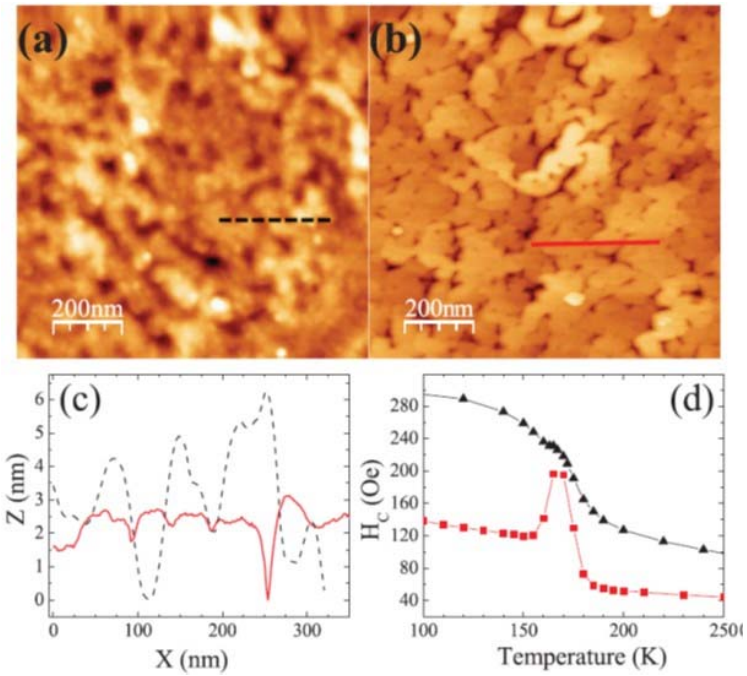

Figure 5.10. (a) and (b) AFM images for V_2O_3/Ni bilayers with different root mean square roughness, (a) 3 nm and (b) 1.5 nm. (c) Height profile along the lines indicated in (a) dashed black line and (b) solid red line. (d) Coercivity as a function of temperature for V_2O_3/Ni bilayers with different roughness: 3 nm black triangles and 1.5 nm red squares. Reprinted from J. de la Venta *et al*., Appl. Phys. Lett. **104**, 062410 (2014). Copyright by the American Institute of Physics.

The magnetic domain size of Ni is related to the microstructure of the Ni film. We estimate the magnetic domain size of Ni from the surface morphology of the bilayers. Figure 5.10 (a) and (b) show the AFM measurements of two V_2O_3/Ni bilayers with different root mean square (RMS) roughnesses. The difference in the roughness causes a difference in the coercivity of the two samples at 250 K, before the SPT occur. Figure 5.10(c) shows the height profile of the two samples. The bilayer with lower roughness (Figure 5.10(b)) shows terraces over 100's of nm with < 1 nm roughness (solid red line in Figure 5.10(c)). We assume that the magnetic domain of Ni can be as large as a terrace (> 100 nm) due to its smooth surface. Between terraces, the magnetic domains are separated by defects. If the V_2O_3 domains are smaller than 100 nm, the magnetic domains of Ni are larger than the V_2O_3 domains. In this case, the phase coexistence in V_2O_3 enhances the coercivity of Ni in the middle of its SPT as shown by the red squares in Figure 5.10(d). For the bilayer with higher roughness, we assume the magnetic domain size of Ni is the same as the grain size (50 – 100 nm), which is given by the local minimum in the AFM height profile (dashed black line in Figure 5.10(c)). Between grains, the magnetic domains are separated by defects. If the V_2O_3 domains are as large as the grains, the magnetic domain size of Ni and the V_2O_3 domain size are the same. Note that we assume the Ni and V_2O_3 grain size to be the same. In this case, the pinning is governed by the grain boundary and the phase coexistence in V_2O_3 does not increase the pinning significantly. As a result, no coercivity enhancement is observed, shown by the black triangles in Figure 5.10(d). Note that coercivity enhancement due to the phase separation was observed in $Nd_{0.5}Sr_{0.5}CoO_3$ films grown on $SrTiO_3$ substrates [36]. In this case, the coercivity enhancement is due to an interfacial phase separation in $Nd_{0.5}Sr_{0.5}CoO_3$ leading to additional pining centers.

V.3.3 Micromagnetic simulation

I performed micromagnetic simulations with Object Oriented MicroMagnetic Framework (OOMMF) [37] to investigate whether nanoscale phase coexistence in V_2O_3 causes magnetic domain separation and domain wall pinning in Ni. In this simulation, I modeled a 1 μm × 1 μm × 10 nm Ni slab with an exchange constant of A = 3.4 pJ/m and saturation magnetization M_S = 494 kA/m [33]. The cell size in the finite difference simulation was given by the exchange length in Equation (5.3):

$$l_{ex} = \sqrt{\frac{2A}{\mu_0 M_S^2}}. \tag{5.3}$$

Below this length scale, the exchange interaction dominates and all the spins are aligned in the same direction so they can be treated as one magnetic moment [33]. I assumed that there were no defects such as roughness and grain boundaries in the Ni slab. The V_2O_3 under the Ni was divided into 100 nm × 100nm domains. The SPT in each V_2O_3 domain takes place independently. I also assumed that the transition temperatures for individual V_2O_3 domains follow a Gaussian distribution. The mean value of the transition temperatures is 165 K and the standard deviation is 5 K to reproduce the coercivity change with temperature. The SPT of the V_2O_3 domains induces a stress anisotropy in the Ni on top. Figure 5.11 shows the stress anisotropy field in Ni induced by the SPT of V_2O_3. At 180 K, V_2O_3 is fully rhombohedral and Ni is assumed to be stress relaxed with zero stress anisotropy (blue color). As the temperature decreases, V_2O_3 domains start to switch to the monoclinic phase. This induces a stress anisotropy in the Ni on top of these domains (green

color). The stress anisotropy induced by the monoclinic phase $K_1 = 1 \times 10^4$ J/m^3 was used to reproduce the coercivity increase from 180 K to 150 K. The boundaries between the stressed and unstressed Ni (red color) act as pinning sites. I assumed a randomly oriented anisotropy to simulate the pinning effect at the boundaries. The anisotropy $K_2 = 4 \times 10^4$ J/m^3 was used for the boundaries to reproduce the coercivity increase from 180 K to 165 K. I assumed the width of the boundaries was 25 – 30 nm, because this better reproduced the data in Figure 5.9(c). The domain wall width parameter [33] given by Equation (5.4),

$$\delta = \sqrt{\frac{A}{K_1}}, \tag{5.4}$$

is 18 nm for A = 3.4 pJ/m and $K_1 = 1 \times 10^4$ J/m^3, implying that the domain wall width between the magnetic domains of stressed and unstressed Ni is close to the width of the boundaries which I assumed in the simulation.

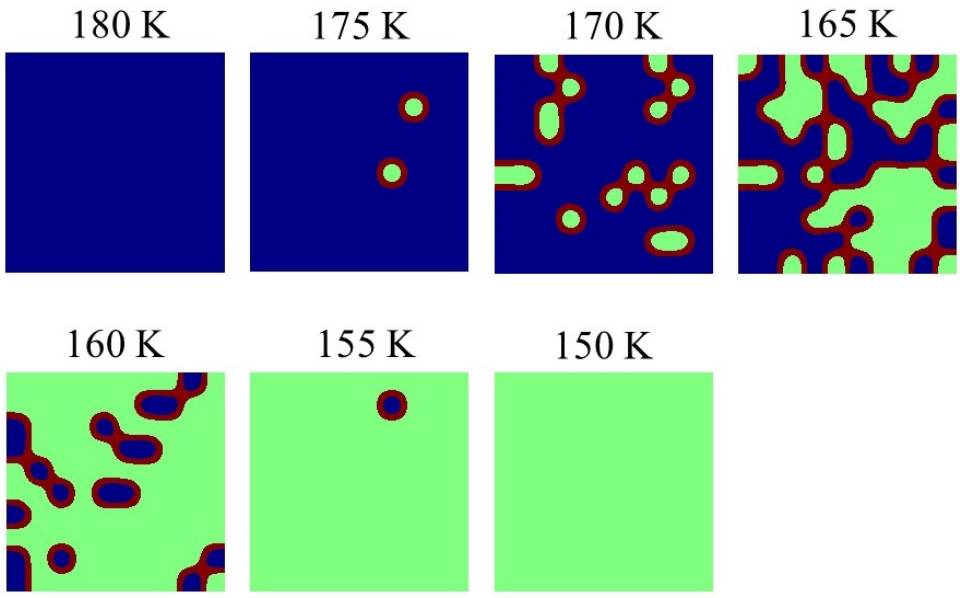

Figure 5.11. Stress anisotropy distribution in Ni at 150 – 180 K. The color coding shows different anisotropy values: The blue color indicates K = 0 J/m^3 for the rhombohedral phase of V_2O_3, while the green color indicates K = 1 × 10^4 J/m^3 for the monoclinic phase of V_2O_3 and the red color indicates K = 4 × 10^4 J/m^3 for the boundary between the two phases.

Figure 5.12 shows the simulated coercivity of Ni compared with the coercivity from the experimental data. For temperatures above 180 K, we used zero anisotropy in the simulations because Ni on top of the rhombohedral phase is polycrystalline and stress relaxed. The simulated coercivity is 25 Oe for these temperatures. From 175 – 165 K, the volume of the monoclinic domains increases and so does the area of the boundary between the two phases, as shown in Figure 5.11. This leads to an increase in the pinning and the coercivity. At 165 K, the volume fractions of the two phases are equal and the area of the boundary reaches a maximum, as shown in Figure 5.11. The coercivity reaches a maximum due to the strongest pinning at this temperature. From 165 – 150 K, the monoclinic phase becomes the majority phase in V_2O_3 and the area of the boundary decreases. This leads to

a decrease of the pinning and the coercivity. Note that at 150 K the coercivity is higher than at 180 K even though the V_2O_3 is homogeneous at 150 K. This is due to the stress anisotropy ($K = 1 \times 10^4$ J/m^3) induced by the monoclinic phase of V_2O_3. The simulation reproduces the coercivity enhancement measured in the V_2O_3/Ni bilayer. Defects such as surface roughness and grain boundaries are not considered in the simulation. The temperature dependence of the exchange constant A and saturation magnetization M_S are not taken into account in the simulation. This gives rise to an offset between the experiment and simulation and a slope in the measured coercivity versus temperature as shown in Figure 5.12.

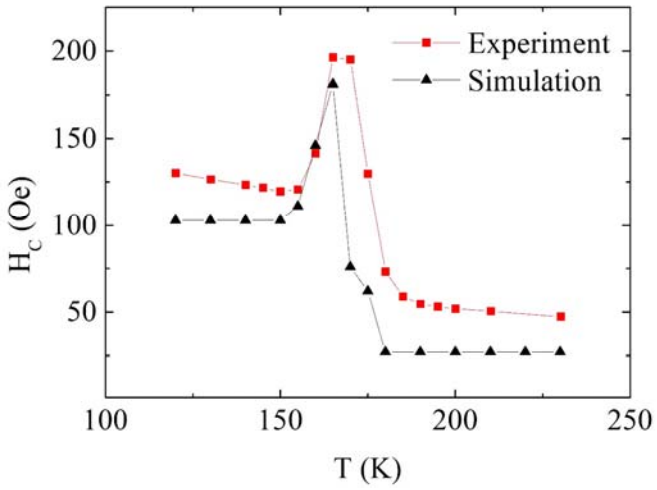

Figure 5.12. Coercivity versus temperature of Ni for experiment (red squares) and simulation (black triangles).

Figure 5.13 compares the simulated magnetization reversal mode for 180 K and 165 K. The simulated coercivity for 180 K is 20 – 30 Oe. When the stress anisotropy is zero and the external magnetic field is low (20 – 30 Oe), the magnetization at the edge of the Ni slab will align parallel to the edge to reduce the demagnetization energy. For applied fields H = 20 Oe (Figure 5.13(a)) and H = 30 Oe (Figure 5.13(b)), the magnetization configuration is always symmetric, with four magnetic domains parallel to the edge of the Ni slab. The simulated coercivity for 165 K is 180 – 190 Oe. For this temperature, the stress anisotropy and pinning at the boundary is predominantly responsible for the magnetization reversal. For applied fields H = 180 Oe (Figure 5.13(c)) and H = 190 Oe (Figure 5.13(d)), magnetic domains of various sizes and domain walls between the magnetic domains are observed in the simulation. The magnetization reversal occurs through domain wall motion and the coercivity is enhanced. To further support this model, magnetic force microscopy (MFM) can be performed to image the magnetic domain structure of Ni, but that is beyond the scope of this thesis.

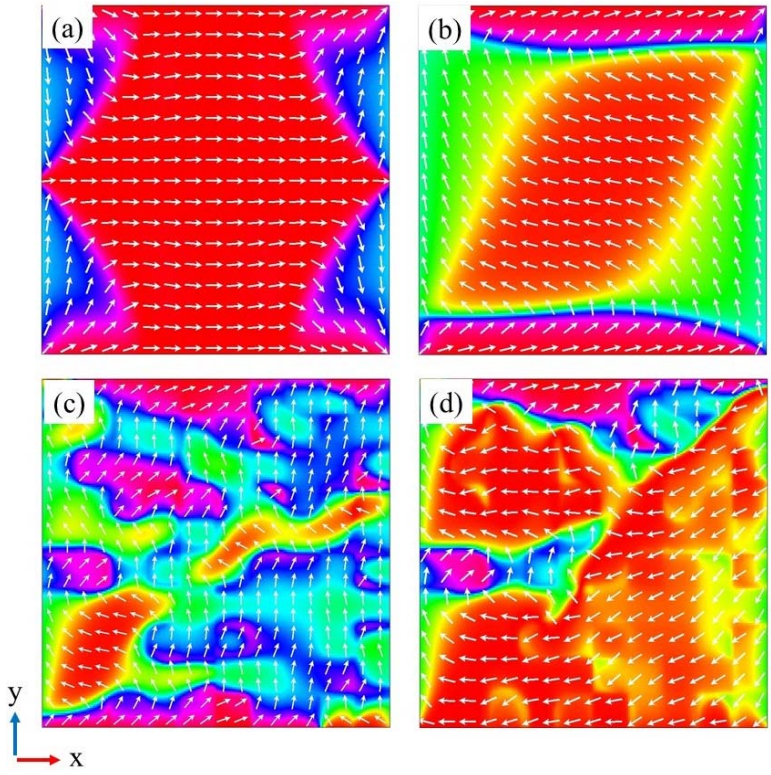

Figure 5.13. Simulated magnetization reversal mode with applied field along x-axis. (a) Magnetization configuration for applied field H = 20 Oe at 180 K. (b) Magnetization configuration for applied field H = 30 Oe at 180 K. (c) Magnetization configuration for applied field H = 180 Oe at 165 K. (d) Magnetization configuration for applied field H = 190 Oe at 165 K. Color coding represents the angle of the magnetic moments with respect to the x-axis: red along the x-axis and blue along the y-axis.

V.3.4 Decoupling V_2O_3/Ni with Cu spacer layer

As discussed in Chapter I, V_2O_3 is an antiferromagnet at low temperature. Exchange interaction between ferromagnetic and antiferromagnetic materials can also cause a coercivity increase in the ferromagnet [19]. To investigate the effect of the exchange interaction, we placed Cu spacer layers with various thicknesses between 100 nm V_2O_3 and 10 nm Ni to decouple the layers magnetically. Figure 5.14 shows that up to 20 nm Cu, the coercivity enhancement remains as strong as the V_2O_3/Ni bilayer. This

means that the strain can transmit through 20 nm Cu, because Cu has the same crystal structure and similar lattice parameters as Ni. Up to 100 nm Cu, the coercivity enhancement is still observable. This excludes the possibility of any effect from the antiferromagnetism of V_2O_3. In addition, we did not observe any exchange bias in these samples. This also suggests that the antiferromagnetism of V_2O_3 does not play a role in the coercivity enhancement.

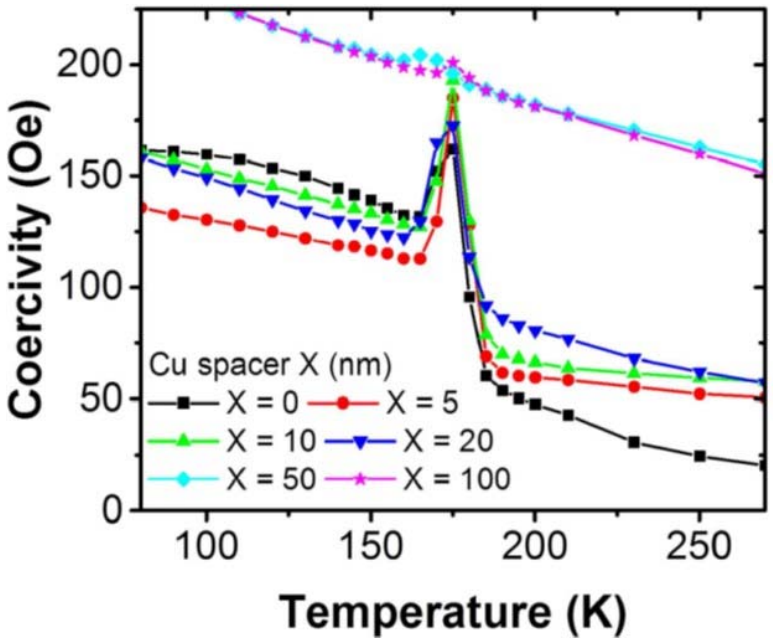

Figure 5.14. Temperature dependence of the coercivity of 100 nm V_2O_3/x nm Cu/10 nm Ni with various Cu thicknesses. Reprinted from T. Saerbeck *et al*., J. Mater. Res. (2014). Copyright by the Materials Research Society.

V.4 Conclusions

In this chapter, I presented the study of the control of magnetism with vanadium oxide/ferromagnet bilayers. The coercivity and remanent magnetization change as the SPT takes place in vanadium oxides, indicating a change in the in-plane anisotropy. This anisotropy is induced by the interface stress from the SPT. Flexible control of the magnetism can be achieved by selecting different deposition temperatures and ferromagnetic materials. The coercivity can change up to a factor of two within 20 K in a VO_2/Ni bilayer.

We observed a ~ 300 % coercivity enhancement in V_2O_3/Ni bilayers in the middle of the SPT of V_2O_3. We attribute the effect to a disorder induced by the nanoscale phase coexistence of V_2O_3. This disorder is caused by the competition in length scale between the V_2O_3 domain and the magnetic domain of Ni. We performed micromagnetic simulation which quantitatively reproduces the coercivity enhancement. A Cu spacer layer is placed between V_2O_3 and Ni to exclude any effect from the antiferromagnetism of V_2O_3.

V.5 Acknowledgements

Chapter V, in part (section V.2), has been previously published in: J. de la Venta, S. Wang, J. G. Ramirez, and I. K. Schuller, "Control of magnetism across metal to insulator transitions", Appl. Phys. Lett. **102**, 122404 (2013). The dissertation author was a co-author of this paper. Chapter V, in part (section V.3), has been previously published in: J. de la Venta, S. Wang, T. Saerbeck, J. G. Ramirez, I. Valmianski, and I. K. Schuller, "Coercivity

enhancement in V_2O_3/Ni bilayers driven by nanoscale phase coexistence", Appl. Phys. Lett. **104**, 062410 (2014). The dissertation author was a co-author of this paper. Chapter V, in part (section V.2 and V.3), has been previously published in: T. Saerbeck, J. de la Venta, S. Wang, J. G. Ramirez, M. Erekhinsky, I. Valmianski, and I. K. Schuller, "Coupling of magnetism and structural phase transitions by interfacial strain", J. Mater. Res.. The dissertation author was a co-author of this paper.

V.6 Reference

[1] V. Laukhin, V. Skumryev, X. Marti, D. Hrabovsky, F. Sanchez, M. V. Garcia-Cuenca, C. Ferrater, M. Varela, U. Luders, J. F. Bobo, and J. Fontcuberta, Phys. Rev. Lett. **97**, 227201 (2006).

[2] M. Gajek, M. Bibes, S. Fusil, K. Bouzehouane, J. Fontcuberta, A. Barthelemy, and A. Fert, Nat. Mater. **6**, 296 (2007).

[3] J. T. Heron, M. Trassin, K. Ashraf, M. Gajek, Q. He, S. Y. Yang, D. E. Nikonov, Y-H. Chu, S. Salahuddin, and R. Ramesh, Phys. Rev. Lett. **107**, 217202 (2011).

[4] R. O. Cherifi, V. Ivanovskaya, L. C. Phillips, A. Zobelli, I. C. Infante, E. Jacquet, V. Garcia, S. Fusil1, P. R. Briddon, N. Guiblin, A. Mougin, A. A. Ünal, F. Kronast, S. Valencia, B. Dkhil, A. Barthélémy, and M. Bibes, Nat. Mater. **13**, 345 (2014).

[5] A. Fert, Rev. Mod. Phys. **80**, 1517 (2008).

[6] J. A. Katine and E. E. Fullerton, J. Magn. Magn. Mater. **320**, 1217 (2008).

[7] L. Liu, C.-F. Pai, Y. Li, H. W. Tseng, D. C. Ralph, and R. A. Buhrman, Science **336**, 555 (2012).

[8] J. S. Kousel and R. H. Wilson, J. Appl. Phys. **32**, 435 (1961).

[9] E. Tatsumoto, H. Fujiwara, H. Tange, and Y. Kato, Phys. Rev. **128**, 2179 (1962).

[10] J. S. Kouvel and C. C, Hartelius, J. Appl. Phys. **35**, 940 (1964).

[11] J.-U. Thiele, S. Maat, and E.E. Fullerton, Appl. Phys. Lett. **82**, 2859 (2003).

[12] J. C. Slonczewski, Phys. Rev. B **82**, 054403 (2010).

[13] Y.-T. Cui, J. C. Sankey, C. Wang, K. V. Thadani, Z.-P. Li, R. A. Buhrman, and D. C. Ralph, Phys. Rev. B **77**, 214440 (2008).

[14] T. Tanaka, N. Narita, A. Kato, Y. Nozaki, Y.-K. Hong, and K. Matsuyama, IEEE Trans. Magn. **49**, 562 (2013).

[15] W. Li, B. Buford, A. Jander, and P. Dhagat, IEEE Trans. Magn. **50**, 3100704 (2014).

[16] S. Mangin, M. Gottwald, C.-H. Lambert, D. Steil, V. Uhlír, L. Pang, M. Hehn, S. Alebrand, M. Cinchetti, G. Malinowski, Y. Fainman, M. Aeschlimann, and E. E. Fullerton, Nat. Mater. **13**, 286 (2014).

[17] H. Y. Hwang, Y. Iwasa, M. Kawasaki, B. Keimer, N. Nagaosa, and Y. Tokura, Nat. Mater. **11**, 103 (2012).

[18] P. Yu, Y.-H. Chu, and R. Ramesh, Mater. Today **15**, 320 (2012).

[19] J. Nogues and I. K. Schuller, J. Magn. Magn. Mater. **192**, 203 (1999).

[20] J. Eisenmenger and I. K. Schuller, Nat. Mater. **2**, 437 (2003).

[21] Y.-H. Chu, L. W. Martin, M. B. Holcomb, and R. Ramesh, Mater. Today **10**, 16 (2007).

[22] S. Sahoo, S. Polisetty, C.-G. Duan, S. S. Jaswal, E. Y. Tsymbal, and C. Binek, Phys. Rev. B **76**, 092108 (2007).

[23] G. Stefanovich, A. Pergament, and D. Stefanovich, J. Phys. Condens. Matter **12**, 8837 (2000).

[24] A. Cavalleri, Cs. Tóth, C. W. Siders, J. A. Squier, F. Ráksi, P. Forget, and J. C. Kieffer, Phys. Rev. Lett. **87**, 237401 (2001).

[25] D. B. McWhan, J. P. Remeika, T. M. Rice, W. F. Brinkman, J. P. Maita, and A. Menth, Phys. Rev. Lett. **27**, 941 (1971).

[26] J. Nag and R. F. Haglund Jr., J. Phys.: Condens. Matter **20**, 264016 (2008).

[27] N. B. Aetukuri, A. X. Gray, M. Drouard, M. Cossale, L. Gao, A. H. Reid, R. Kukreja, H. Ohldag, C. A. Jenkins, E. Arenholz, K. P. Roche1, H. A. Dürr, M. G. Samant, and S. S. P. Parkin, Nat. Phys. **9**, 661 (2013).

[28] B. D. Cullity and C. D. Graham, *Introduction to Magnetic Materials* (John Wiley & Sons, Hoboken, New Jersey, 2009).

[29] B. Viswanath, C. Ko, and S. Ramanathan, Scripta Mater. **64**, 490 (2011).

[30] M. M. Qazilbash, M. Brehm, B.-G. Chae, P.-C. Ho, G. O. Andreev, B.-J. Kim, S. J. Yun, A. V. Balatsky, M. B. Maple, F. Keilmann, H.-T. Kim, and D. N. Basov, Science **318**, 1750 (2007).

[31] T.-H. Yang, R. Aggarwal, A. Gupta, H. Zhou, R. J. Narayan, and J. Narayan, J. Appl. Phys. **107**, 053514 (2010).

[32] Y. Zhao, J. H. Lee, Y. Zhu, M. Nazari, C. Chen, H. Wang, A. Bernussi, M. Holtz, and Z. Fan, J. Appl. Phys. **111**, 053533 (2012).

[33] R. Skomski, J. Phys. Condens. Matter **15**, R841 (2003).

[34] S. Lupi, L. Baldassarre, B. Mansart, A. Perucchi, A. Barinov, P. Dudin, E. Papalazarou, F. Rodolakis, J. -P. Rueff, J. -P. Itié, S. Ravy, D. Nicoletti, P. Postorino, P. Hansmann, N. Parragh, A. Toschi, T. Saha-Dasgupta, O. K. Andersen, G. Sangiovanni, K. Held, and M. Marsi, Nat. Commun. **1**, 105 (2010).

[35] S. Guénon, S. Scharinger, S. Wang, J. G. Ramirez, D. Koelle, R. Kleiner, and I. K. Schuller, EPL **101**, 57003 (2013).

[36] M. Sharma, J. Gazquez, M. Varela, J. Schmitt, and C. Leighton, Phys. Rev. B, **84**, 024417 (2011).

[37] Software description and code available at http://math.nist.gov/oommf.

Chapter VI

Summary

Vanadium oxides are a prototypical transition metal oxide family that exhibits first order phase transitions. The charge, lattice and spin are strongly correlated when the phase transition takes place. Metal insulator transition (MIT), structural phase transition (SPT), and magnetic phase transition occur simultaneously. After 50 years' debate, the physical mechanisms of the phase transitions remain elusive. In the past 15 years, tremendous progress has been made in understanding of the MIT of vanadium oxides on two fronts: (1) inducing the MIT with different driving forces and (2) studying the inhomogeneity during the MIT. Different driving forces for the MIT of vanadium oxides imply that the phase transitions may result from different mechanisms. Inhomogeneities in vanadium oxides at mesoscopic length scales can give rise to a variety of novel phenomena, especially when in proximity with other materials. In this thesis, I report on my studies of the MIT of vanadium dioxide (VO_2) and vanadium sesquioxide (V_2O_3) with advanced thin film deposition and lithographic techniques. To understand the mechanisms of the phase transitions and how they interact with other materials, I focus on three topics: inhomogeneities, driving forces, and proximity effects in mesoscopic vanadium oxides.

In Chapter III, I describe R-T characteristics of V_2O_3 devices from 500 nm to 5 μm. The R-T curves are constituted with discontinuous resistance jumps over two orders of magnitude. Analysis of the jumps shows two characteristics: (1) the maximum jump size scales with the device size as well as shows sample and defect dependence; (2) the distribution of the jump sizes follows a power law. The maximum jump results from

percolation in the V_2O_3 device and is related to the device geometry and defects. The power law distribution of the jumps suggests that the MIT of V_2O_3 occurs through a series of avalanches at the nanoscale. The power law exponent shows no dependence on the sizes, samples, or defects. This means that the power law exponent is related to the intrinsic properties and inhomogeneities of V_2O_3.

The power law exponent of V_2O_3 is compared to that from VO_2 and a 2D random percolation modeling. The power law exponent of the simulation agrees with the one measured in VO_2, which means that avalanches in VO_2 can be described by a 2D random percolation model. However, the power law exponent of V_2O_3 is higher than that of VO_2 and the simulation. This suggests that the MIT of V_2O_3 occurs through a different mechanism than VO_2 and is not a simple 2D random percolation. Asymmetry in the power law exponent is also observed between the heating and cooling of V_2O_3.

In chapter IV, I describe the role of Joule heating in the voltage induced MIT of vanadium oxide microdevices. Local temperature of VO_2 microdevices were measured with a calibrated fluorescent particle when the MIT was induced by a voltage. The local temperature increased with the increasing voltage and reached the transition temperature from the R-T measurements. The heating can be modeled with a phenomenological Ohmic dissipation model. These direct local temperature measurements suggest that Joule heating plays a predominant role in the voltage induced MIT of the VO_2 microdevices.

The study of the voltage induced MIT was extended to V_2O_3 microdevices. Low temperature scanning electron microscopy (LTSEM) was performed when the current was applied to the microdevices at two different base temperatures, 145 K and 155 K. The

LTSEM showed that the voltage induced MIT in V_2O_3 was inhomogeneous at the nanoscale. At 145 K base temperature, the voltage jumped to a lower value and a metallic filament formed when the voltage induced MIT occurred. The I-V characteristic and the filament formation can be reproduced with a Joule heating model, suggesting that at 145 K the voltage induced MIT of V_2O_3 can be explained by Joule heating. However, at 155 K base temperature, the voltage induced MIT occurs through multiple small voltage jumps and nanoscale metallic domains nucleate in V_2O_3, which cannot be reproduced by the Joule heating model. This indicates that a different mechanism might be involved.

In Chapter V, I describe the magnetic properties of the vanadium oxide/ferromagnet bilayers. For a VO_2/Ni bilayer, the coercivity can change by a factor of two when the SPT of VO_2 takes place. The SPT of VO_2 induces a stress anisotropy in Ni through the inverse magnetostrictive effect. The magnitude of the stress can be estimated by the coercivity change across the SPT of VO_2. The magnitude of the coercivity change can be altered by choosing a different ferromagnetic material; the critical temperature of the effect can be changed by choosing a different vanadium oxide; and the effect can be reversed by choosing a different deposition temperature for the ferromagnet. This allows for a very flexible control of magnetism.

An approximately 300% coercivity enhancement was observed in V_2O_3/Ni bilayers at the middle of the SPT of V_2O_3. This effect originates from the phase coexistence in V_2O_3 during the SPT. There are two competing length scales contributing to the coercivity enhancement: the magnetic domains size of Ni and the rhombohedral domain size of V_2O_3. When the rhombohedral domain size of V_2O_3 is smaller than the magnetic domains size of

Ni, the phase coexistence in V_2O_3 can induce pinning at the phase boundaries. This temperature dependent disorder breaks the magnetic domains of Ni and pins the magnetic domain wall. This leads to an enhanced coercivity at the middle of the SPT of V_2O_3, when the two phases in V_2O_3 are equal in the contact area with the Ni. This model is supported by the microstructure study of the bilayer with AFM and micromagnetic simulations.

In this thesis, I have presented my research on the inhomogeneities, driving forces, and proximity effect in the phase transition of mesoscopic vanadium oxides. The inhomogeneity at mesoscopic scale is related to both the driving force and the proximity effect. When inhomogeneity is taken into account, heating is shown to be an important driving force in the current or voltage induced phase transitions in vanadium oxides. The inhomogeneity also gives rise to a variety of novel phenomena when vanadium oxides are in proximity with other materials. The work in this thesis will shed light on other research on transition metal oxides with phenomenology similar to vanadium oxides.

Chapter VII

Outlook

There are several open questions about the phase transitions in vanadium oxides.

1. Avalanches in V_2O_3

- A theoretical model needs to be developed to describe the avalanches in V_2O_3. A 2D random percolation model is not sufficient.
- The possible role of supercooling in the asymmetry of the metal insulator transition (MIT) of V_2O_3 is not well understood. Supercooling can be suppressed by defects. Controlled doping or ion irradiation can create defects in V_2O_3 and suppress the asymmetry of the MIT.
- Single crystalline V_2O_3 nanobeams can be synthesized to reduce the number of defects and the effect of supercooling. The asymmetry of the MIT of V_2O_3 should be enhanced.

2. Voltage induced MIT in V_2O_3

- Low temperature scanning electron microscopy of V_2O_3 microdevice at 155 K indicates a different mechanism than Joule heating. If Zener tunneling is involved, it may be observed in the I-V characteristics of V_2O_3 nanodevices, because the electric fields in nanodevices is higher due to the smaller device size.

3. Control of magnetism with vanadium oxides

- The phase coexistence in V_2O_3 can be investigated with scanning near-field optical microscopy.
- The magnetic domain structure in Ni during the structural phase transition (SPT) of V_2O_3 can be investigated with magnetic force microscopy and neutron scattering.

4. Ultrafast spectroscopy of vanadium oxides

- The relationship between the MIT and SPT in < 100 fs time scale remains an open question. In-situ optical pump – optical probe and optical pump – X-ray probe experiments can be performed to compare the time scale of the MIT and SPT.
- Optical second harmonic generation can be measured to extract structural information instead of X-ray.
- To understand the role of the SPT in the voltage induce MIT, terahertz pump – X-ray probe experiments can be performed on metamaterials fabricated with vanadium oxides. High electric fields induced by the metamaterials can drive the MIT in vanadium oxides. The time scale of the MIT and SPT can be compared when the voltage induced MIT takes place.